University of Southampton

Faculty of Engineering and Physical Sciences
Zepler Institute for Photonics and Nanoelectronics

Nonlinear optical components and systems for quantum technologies and communications

by

Alan Ciarán Gray
B.Sc., M.Sc.
ORCiD: 0000-0002-2316-8821

A thesis for the degree of
Doctor of Philosophy

March 2021

University of Southampton

Abstract

Faculty of Engineering and Physical Sciences
Zepler Institute for Photonics and Nanoelectronics

Doctor of Philosophy

Nonlinear optical components and systems for quantum technologies and communications

by Alan Ciarán Gray

This thesis describes a series of experimental research primarily revolving around the applications of periodically poled lithium niobate (PPLN). Initially, a set of work is described regarding the fabrication and characterisation of PPLN ridge waveguides designed for frequency doubling into the blue/UV range. These waveguides are fabricated via diffusion of zinc into the crystal structure. A precision dicing process creates the sidewall definition for modal confinement and also optical facet preparation. Preliminary results with the most efficient waveguide fabricated produced a maximum conversion efficiency of 6.9%/W in a 14 mm-long device, generating 391 nm light. This was performed with a novel near-IR VECSEL; designed and built as part of a collaboration with the research undertaken in this thesis to investigate new routes for miniaturised UV sources.

The development of a non-destructive route to characterise the physical dimensions of a ridge waveguide for nonlinear applications is also presented. This presented methodology uses white light interferometry and standard edge recognition algorithms to determine the waveguide width profile. In combination with numerical propagation constant data for these waveguides, a numerical phasematching spectra can be calculated. A comparison to the experimental phasematching spectra of the second-harmonic generation process enables the discrimination between issues in the fabrication processes.

Using bulk PPLN, a final application is presented for communications using mid-IR radiation and all commercial components. This configuration involves the use of difference-frequency generation followed by sum-frequency generation to create the transmitter and receiver systems, respectively. This enables final detection of 809 nm light (firmly within the silicon absorption band). Bit error ratios as low as 10^{-7} from single-pass nonlinear conversion for both systems without the need for an additional optical amplifier in the receiver. Finally, the propagation of relative intensity noise within the system as the source lasers propagate through a two step nonlinear conversion is presented and discussed within.

Contents

List of Figures

List of Tables

Declaration of Authorship

I declare that this thesis and the work presented in it is my own and has been generated by me as the result of my own original research.

I confirm that:

1. This work was done wholly or mainly while in candidature for a research degree at this University;
2. Where any part of this thesis has previously been submitted for a degree or any other qualification at this University or any other institution, this has been clearly stated;
3. Where I have consulted the published work of others, this is always clearly attributed;
4. Where I have quoted from the work of others, the source is always given. With the exception of such quotations, this thesis is entirely my own work;
5. I have acknowledged all main sources of help;
6. Where the thesis is based on work done by myself jointly with others, I have made clear exactly what was done by others and what I have contributed myself;
7. Parts of this work have been published as:
   Alan C. Gray *et al.*, Leaky mode integrated optical fibre refractometer. Optics Express, 26(7):9155-9164, 2018
   Alan C. Gray *et al.*, Zinc-indiffused MgO: PPLN waveguides for blue/UV generation via VECSEL pumping. Applied Optics, 59(16):4921-4926, 2020,
   Alan C. Gray *et al.*, Investigation of PPLN waveguide uniformity via second harmonic generation spectra. IEEE Photonics Technology Letters, 32(1):63-66, 2019,
   Alan C. Gray *et al.*, Upconversion detection of 1.25 Gb/s mid-infrared telecommunications using a silicon avalanche photodiode. Optics Express, 2020 (In-press)

Signed:.. Date:..................

Acknowledgements

First and foremost, I would like to thank Prof. Peter Smith. Initially, for taking a chance on me and offering a position within his group but also for the long hours of discussions and the level of commitment he has shown to me and my work. Coming up in a close second, I would like to thank Dr. Corin Gawith. I have never met a busier man but he always pulls through and those moments of brutal honesty are legitimately priceless. And to Dr. Christopher Holmes who taught me the ropes in the early stages of my PhD and guided me towards the researcher I am today.

To Sam Berry and Lewis Carpenter, who took me under their respective wings to ensure I wouldn't fall. While their technical skills were vital to my own development and the work herein, their ability to make the long hours in the lab an absolute delight will forever be the primary reason I am grateful. I would like to thank Lewis specifically for his contribution to some of the devices contained within this thesis.

The work within this thesis would never have been completed without the support from all members of this research group, past and present. This applies in particular to Dr. James Gates, whom has provided a wealth of knowledge and encouragement and was never under any obligation to; I will be forever grateful. To Matthew Posner and Stephen Lynch who were able to convince me it would all be worth it (despite their own begrudgings regarding a life in academia!). To the rest of the team: James Field, Alex Jantzen, Senta Jantzen, Paula Smith, Rex Bannerman, Devin Smith, Paul Gow and Charlie Turner; I am delighted to have gotten to know you all. I thoroughly enjoyed the friendship and support you provided throughout my PhD.

I would like to thank my VECSEL collaborators in the department of Physics and Astronomy Dr. Jonathan Woods, Dr. Vasilis Apostolopoulos and Prof. Anne Tropper who let me invade their lab. Specifically, to Jonathan who contributed vast hours to our work with such astonishing enthusiasm. Also, Dr. Hermann Kahle and Prof. Mircea Guina from Tampere University, who provided materials for experimentation and invaluable feedback when the time for manuscript preparation arose.

I would also like to thank the technical support staff within the ORC, who have helped me with everything from technical cleanroom issues to keeping the temperature in the optics lab pleasant. I would also like to thank Prof. David Smith who permitted me time in his lab to do some emergency measurements.

There are many other members of the ORC to whom I am grateful for their support and some who have become close friends, primarily Andrei, Kat and Jonny, whose support in the latter stages I will never be able to repay. To Tom, Nic, Olly, Ed and Lewis for making my teaching experience all the more enjoyable and educational for me too.

Finally, to Alison, who somehow hasn't left me yet. I thank you for everything.

"Perfection is attained by slow degrees; it requires the hand of time."

- Voltaire

Chapter 1

Introduction

1.1 Introduction

Since the development of the laser 60 years ago [1] this technology has played a role in almost all aspects of the economy and society to advance our standard of living. Lasers have found themselves used in an assortment of areas including optical telecommunications, CD/DVD technologies, medical, manufacturing, metrology and many more. In addition to their contribution to our everyday lives, and since Feynman's proposal of quantum computation in the 1980's [2], the quantised nature of this light can be exploited to enable light itself to be a viable candidate for quantum computation alongside enabling the cooling of atoms and ions in competitor quantum technologies.

As well as their use of generating accessible quantum particles, lasers provide a route towards high optical intensities; this leads to the entire field of nonlinear optics, which started with Bloembergen in the early 1960's [3]. Since then, nonlinear optics has become a vital technological area via the applications of, but not limited to, Raman amplification, Kerr mode locking and even within the walls of a classroom through green laser pointers. Increasingly, nonlinear optics is finding important applications in quantum technologies both for single/pair photon generation and generating light at required wavelengths where conventional lasers are less practical than using harmonic generation or other nonlinear processes. Thus, the subject of this thesis is the use of periodically poled lithium niobate (PPLN) for the generation and detection of obscure frequencies of light which are otherwise challenging to obtain or difficult to detect.

1.1.1 Nonlinear optics in quantum technologies

Major worldwide investments have accelerated the development of quantum technologies (QT), specifically within the EU and the USA. This includes €1bn in the EU Quantum

Flagship, \$1.2bn in the US Quantum Initiative and £1bn in the UK's National Quantum Technologies Programme. The scale of this funding indicates the importance of QT to governments for a variety of reasons, including security, national prestige, and economic opportunity. Broadly speaking, the main aims of this research and product development are the next generation of computation, sensing and secure communications via quantum encryption. However, commercial realisation of mass produced or miniaturised systems for quantum computation or metrology is hindered by a lack of commercially available components that are required. Included in this are: the light sources required for ion trapping - a leading candidate for quantum computation; cold atoms - for sensors and quantum memories; the efficient generation of single-photons with the desired characteristics for quantum applications; and a method to route photons in low-loss waveguides.

One of the predominant research interests in this work has been developing technologies capable of delivering light following wavelength conversion from a more commercially available, high-specification laser source - good examples being light at around 780 nm for Rb atom trapping, and UV/blue for ion trapping technologies. Nonlinear optics is particularly appropriate for such sources. Nonlinear optical research in this thesis reports on the generation of blue/UV in PPLN ridge waveguides at wavelengths close to ion trap requirements in an optical platform which has recently resulted in world-record conversion powers for Rb wavelengths [4] (but not discussed within this thesis). Further research demonstrates the use of bulk PPLN crystals for an important and developing opportunity in up-conversion detection from mid-IR for communication applications. This approach offers many advantages relative to conventional IR detectors, particularly avoiding the need for cooling, and fast detection. Finally, work on a potential application of attached optical fibre as a refractometer is presented as an aside body of work.

1.2 Blue/UV lasers for ion trapping

Ion trapping has been a candidate for achieving quantum computing since its suggestion by Cirac and Zoller in 1995[5]. It is considered a viable candidate for quantum computation due to their long coherence times. Current state-of-the-art has attained coherence times of approximately 10 minutes in a hybrid Yb^+ and Ba^+ system [6]. While ions are typically trapped in rotating electric fields which form the RF Paul trap, the use of techniques such as Doppler cooling [7] alongside other cooling methods are implemented to reduce the temperature of the ion as close to absolute zero as possible. This use of the Doppler effect involves a narrow linewidth laser which is tuned to a frequency slightly below resonance of the ion which is being trapped. In this configuration, the ion will only interact with the incoming photon if it is moving towards the laser beam.

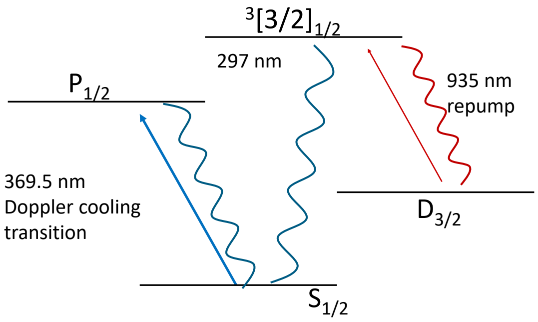

FIGURE 1.1: The excitation processes of the Yb^+ ion used in quantum metrology experiments. Note the energy transition associated with a UV photon's energy. Hence, a source for targeting this transition is required. Adapted from [8].

A variety of different ion species have been experimented with for applications in quantum computing. These include Mg^+, Ca^+, Sr^+ and Yb^+. Of most relevance to the work presented in this thesis is the Yb^+ ion. This ion has an optimum wavelength for Doppler cooling of 369.5 nm, the $^2\mathrm{P}_{1/2} \to ^2 S_{1/2}$ dipole transition. The UV sources currently available at this wavelength do not meet stability or laser linewidth requirements as they push the limits of current technology with regards to both material science and optical engineering.

1.2.1 Nonlinear ridge waveguides as a route towards blue/UV generation

Prior work to achieve blue or UV wavelengths has included semiconductor diode lasers and rare-earth ion doped upconversion lasers. Although the demonstration of the GaN semiconductor diode lasers at 405 nm was a remarkable scientific feat, diode lasers are restrictive in wavelength range and typically output an inconvenient mode shape. Hence, nonlinear conversion is a key competitor in the engineering challenge for specific, short wavelength sources. This has also led to a drive in research for higher power infrared lasers to compensate for a potentially low conversion efficiency in some instances using nonlinear optical crystals. Nonlinear optical theory provides us with the information that the greatest intensity and spatial overlap should increase the conversion efficiency [9].

Recent work here at the University of Southampton has demonstrated the applicability for high power-handling lithium niobate ridge waveguides [4, 10], which have been designed for frequency-doubling 1560 nm light to 780 nm light. Hence, the development of this technology will form a large portion of the work presented in this thesis where the primary goal is to offer a competitive route towards the miniaturisation of blue/UV sources, schematically displayed in figure 1.2. The diffusion of dopant elements creates a refractive index contrast to form the basis of a waveguide. The relatively large propagation modal area, in comparison to other techniques for nano waveguides [11, 12],

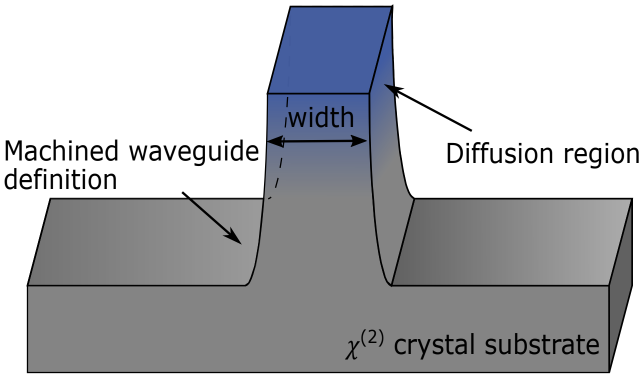

Figure 1.2: An illustration of a ridge waveguide in a nonlinear optical crystal where the higher refractive index to form a waveguide is performed via in-diffusion of an appropriate element. This concept is used to develop the waveguide technology used in this work.

maximises the potential for high damage thresholds and optical power coupled into the waveguide to seed the nonlinear process.

1.3 Upconversion detection of mid-IR radiation

Depending on the background of the reader, there may be a few automatic assumptions as to the use of mid-IR (MIR) radiation. This is likely to be aligned with spectroscopic sensing, in which this band of the electromagnetic spectrum is commonly referred to as the molecular-fingerprint region, ranging from 2-20 µm; although subsets of this band may have vastly different applications. This spectral region is termed so due to the vast amount of absorption peaks corresponding to rotation or vibrational excitation lines in organics and hydrocarbons [13]. To quantify the MIR signal absorption (and hence concentration of hydrocarbon), a viable route is to convert this signal into the NIR spectral range to take advantage of highly responsive semiconductor detectors [14]. The conversion of lower frequency light to a higher frequency signal for more convenient detection is termed upconversion detection. While there exists a plethora of applications for upconversion detection, this operating principle remains constant.

Operating at longer wavelengths than the conventional 1.55 µm C-band has potential advantages in free space optical communications due to a reduction in Rayleigh scattering ($1/\lambda^4$) and the potential for additional data security; signal absorption through the atmosphere is also minimal at MIR wavelengths, as shown in figure 1.3. The challenge in developing MIR communications systems is not so much the modulation of longer wavelength signals, but the availability of high-speed, sensitive photodetectors. High-speed detection of MIR signals via a standard HgCdTe detector is generally limited to <100 MHz, while industrial applications would ideally be capable of at least an order of

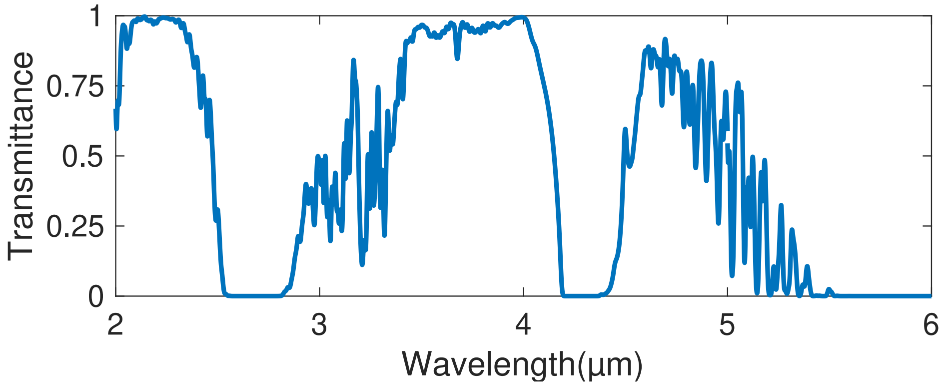

Figure 1.3: A coarse representation of the transmittance of mid-IR wavelengths though the atmosphere. Data is taken from the HITRAN 2016 database and corresponds to simple horizontal transmission on the Earth's surface.

magnitude increase in this data rate. The reduced bandgap of the semiconductor materials used to detect MIR radiation consequently introduces the requirement for cooling to reduce noise induced by thermal emission; a summary of a subset of MIR detectors is presented in table 1.1. The potential for enhanced security is a result of the relatively narrow criteria to perform nonlinear optical conversion, i.e., a malicious party will need to know the precise transmission wavelength to convert to a high-speed, detectable wavelength in the near-IR. Additionally, operating in the absorption bandwidth (< 1100 nm) of silicon-based detectors presents an opportunity to reduce total components in a receiver system and potentially exploit the typically higher quantum efficiency to observe improvements in system performance; forming the basis of the investigations carried out in this thesis on this topic.

Table 1.1: Commercial detectors of IR radiation. Values given are approximate or within an order of magnitude.

Detector	λ range (µm)	Speed (GHz)	Cost (£)	Cooling?
Si	0.4 - 1.1	1	> 2000	No
InGaAs	0.7 - 1.8	40	< 5000	No
GaAs	0.45 - 0.87	10	< 5000	No
FLIR	3 - 12	0.00003	100	No
HgCdTe (MCT)	2 - 10	0.2	< 1000	Yes
SNSPD	0.2 - 2	0.1	100,000	Yes

1.4 Low-loss integrated waveguides

Another topic at the forefront of realising quantum technologies is the requirement to route photons between optical processes without substantial signal loss; this is an increasingly important specification when utilising single photons. One experiment in which a user will wish to route single photons is the demonstration of the Hong-Ou-Mandel (HOM) dip; a technique which confirms photon indistinguishability of a source. In 1987, Hong *et al* [15] carried out this experiment to demonstrate non-classical interference of two indistinguishable photons. To achieve this, a beam of light was passed through a nonlinear crystal, both the signal and idler photons were directed towards a beamsplitter to spatially separate and be re-directed to interfere at another beamsplitter. It was seen that if the beamsplitter underwent a small displacement, a dip in coincidence rate was observed across the two detectors receiving the respective photons.

Integrated optical adaptations [16, 17, 18] of the initial HOM experiment utilize integrated directional couplers in replacement of bulk optic beamsplitters. The proceeding recombination and interference is simply a Mac-Zehnder interferometer (MZI) and a single arm phase shift via thermo- or electro-optic tuning. Having the capability to integrate the low propagation losses of optical fibre with the mechanical and thermal stability of a large substrate would prove advantageous if the required devices could be fabricated in this platform.

The ruggedness of a fibre-on-planar platform also allows for the creation of sensors, particularly refractometers, in which the low-loss aspect of optical fibres at communication wavelengths is intentionally infringed upon to explore the modulation of propagation loss as a measurable quantity. This is enabled via a wealth of experience in inscribing Bragg gratings into silica waveguides at Southampton [19, 20, 21, 22].

1.5 Research context

This work is partially sponsored by the European Office of Aerospace Research and Development (EOARD) with the task of investigating technological routes for delivering blue/UV laser light, generated via nonlinear optical processes.

The nonlinear waveguide development work ran alongside Innovate UK funded projects such as Pioneer Gravity and Cold-Atom Space PAyload (CASPA) which were interested in the development of high-power and efficient nonlinear waveguides for wavelength conversion from 1560 nm to 780 nm using the second harmonic generation process. The research presented in this thesis with regards to blue/UV generation is an extension of our team's long-term research goal to create a broad range of wavelength conversion devices. The presented work regarding MIR communications in Chapter 6 is generally aligned to the goals of QUINTESSENCE, an EPSRC funded QT fellowship project regarding a range of frequency conversion applications.

1.6 Synopsis

Due to the relatively constant theme of the application of nonlinear optics, particularly the use of PPLN as the crystal of choice, Chapter 2 shall provide the majority of the underlying theory to explain the work presented in this thesis. This thesis, where possible, attempts to consist of self-contained Chapters. Following the initial background theory in Chapter 2, Chapter 3 provides the historical context in the form of a literature review on fabrication of quasi-phasematched devices and waveguide development in PPLN.

Chapter 4 presents the preliminary work to fabricate a nonlinear waveguide capable of generating blue/UV light. This work discusses the fabrication challenges associated with nonlinear conversion of a 780 nm source into a 390 nm output and characterisation of fabricated devices. This work provides a stepping stone towards the fabrication of devices for the 739 nm to 369.5 nm process required for application in Yb^+ ion trapping technologies.

Chapter 5 presents a method of physically characterising the fabrication intolerances of ridge waveguides in PPLN and how this may affect the nonlinear optical phasematching spectrum. A discussion of the literature regarding non-perfect nonlinear waveguides, theoretically or experimentally, is also contained within this chapter.

Chapter 6 introduces a system using bulk PPLN crystals and will be a self-contained body of experimental work, motivation and a short literature review regarding MIR telecommunications and upconversion detection. The experimental work contains the design and characterisation of an experimental up-conversion detection scheme for a 1.25 Gb/s system where the final detection is performed using a silicon avalanche photodiode to investigate the applicability of high-speed, free-space optical communications at MIR wavelengths.

Chapter 7 is truly self-contained and is intended to be somewhat of an aside body of work performed in the course of my PhD. I will present the fabrication and testing of a refractometer for harsh environment sensing. This is realised using an optical fibre which has been chemically etched and ruggedized via the deposition of a silica-based glass layer to bond it to a silica-on-silicon substrate.

Chapter 8 includes a summary of the key points presented and discussed in the main body of this thesis along with some final comments regarding the long-term direction of research.

Chapter 2

Nonlinear optics: theory of three-photon parametric processes

2.1 Introduction

Under the over-arching title of nonlinear optics, there exists a vast number of applicable materials, fundamental processes and physics and, hence, phenomena and effects. These effects and applications range from enabling quantum entanglement via the quantised nature of light to biomedical characterisation and methodologies for achieving high peak-power lasers. One of the simplest applications is to acquire a certain wavelength of light which is challenging to obtain from a direct source, or to take advantage of high quality optical components at standardised wavelengths. These final two points will be the predominant theme throughout this thesis and will make use of three-photon processes which are enabled through crystalline materials with a non-negligible $\chi^{(2)}$ coefficient. Providing the background physics of this specific route for frequency conversion is the primary task of this chapter.

2.2 Processes of nonlinear generation

In this section, an introduction to the origins of nonlinear optics is given, primarily based on the workings in Boyd [23] and the use of lithium niobate as the choice of nonlinear crystal for the experimental applications presented in this thesis. In general, nonlinear optical phenomena occur due to the generalisation of the electric field induced polarization in a material,

$$P(t) = \epsilon[\chi^{(1)}E(t) + \chi^{(2)}E^2(t) + \chi^{(3)}E^3(t) + ...] \tag{2.1}$$

where $\chi^{(1)}$ represents the linear susceptibility, $\chi^{(2)}$ and $\chi^{(3)}$ represent the second and third order nonlinear susceptibilities respectively. The latter two are non-negligible values in non-centrosymmetric and centrosymmetric materials, respectively. For the remainder of this thesis, I shall only be concerned with $\chi^{(2)}$ nonlinear optical processes; so-called three-wave nonlinear processes. If we assume there are two distinct input frequencies, and the electric field is defined as

$$E(t) = E_1 \exp\left(-i\omega_1 t\right) + E_2 \exp\left(-i\omega_2 t\right) + c.c., \tag{2.2}$$

the nonlinear polarisation is given by

$$\begin{aligned} P(t) = \epsilon_0\chi^{(2)}[E_1^2\exp(-2i\omega_1)t + E_2^2\exp(-2i\omega_2 t) + 2E_1E_2\exp(-i(\omega_1+\omega_2)t) \\ + 2E_1E_2\exp(-i(\omega_1-\omega_2)t) + c.c] + 2\epsilon_0\chi^{(2)}[E_1E_1^* + E_2E_2^*] \end{aligned} \tag{2.3}$$

where the first and second terms represent second harmonic generation (SHG), the third term is sum-frequency generation (SFG) and the fourth term is difference-frequency generation (DFG). In figure 2.1, the energy level diagrams of these nonlinear $\chi^{(2)}$ processes are shown. The dashed upper line indicates the total energy of which one or more

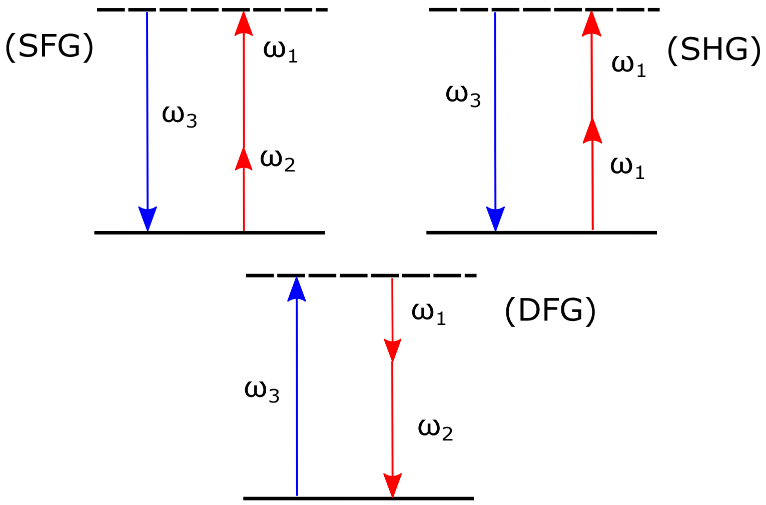

FIGURE 2.1: Energy conservation diagrams of the $\chi^{(2)}$ nonlinear processes: sum-frequency generation (SFG), second harmonic generation (SHG) and difference-frequency generation (DFG). Notice the upper dashed line to indicate energy conservation of the photons must be adhered to for the nonlinear optical process.

photon's energy are combined in an interaction. This distinguishes the interaction of nonlinear optical processes from that of absorption effects due to the incoming radiation satisfying the excitation conditions for electronic transitions.

In the susceptibility tensor, $\chi^{(2)}_{ijk}$, the indices represent Cartesian coordinates. By historical convention, I now introduce the matrix d_{ijk} where

$$d_{ijk} = \frac{\chi^{(2)}_{ijk}}{2} \tag{2.4}$$

which is typically used to describe the nonlinear property of a crystal. This parameter, and its $\chi^{(2)}$ equivalent, is a third rank tensor but can be represented as a two-dimensional matrix when frequency information is suppressed and we assume the Kleinman symmetry condition [24] holds true. This condition is that $\chi^{(2)}_{ijk}(\omega_3;\omega_1;\omega_2)$ is equal to $\chi^{(2)}_{ikj}(\omega_3;\omega_1;\omega_2)$. This is intuitively true far away from material resonances when the linear refractive index is not quickly changing. Additionally, Smith [25] makes an argument that this statement cannot be proved incorrect as there are very few methodologies precise enough to invalidate this assumption but it has not been proven incorrect to date. Nevertheless, it allows for a contraction in subscript notation by replacing *jk* with a new index, l. Hence, d_{il} is expressed as

$$d_{il} = \begin{bmatrix} d_{11} & d_{12} & d_{13} & d_{14} & d_{15} & d_{16} \\ d_{21} & d_{22} & d_{23} & d_{24} & d_{25} & d_{26} \\ d_{31} & d_{32} & d_{33} & d_{34} & d_{35} & d_{36} \end{bmatrix}, \tag{2.5}$$

and some of these parameters are not independent, also due to the Kleinman symmetry condition. As previously mentioned, a non-negligible $\chi^{(2)}$ requires a non-centrosymmetric crystal structure. For a given crystal, this is not true for radiation propagating in any arbitrary direction, as some directions of propagation will posses a symmetric structure. This will result in the matrix element disappearing to zero. A class 3m crystal structure, such as that of $LiNbO_3$ [26], has a nonlinear susceptibility matrix

$$d_{il} = \begin{bmatrix} 0 & 0 & 0 & 0 & d_{31} & -d_{22} \\ -d_{22} & d_{22} & 0 & d_{31} & 0 & 0 \\ d_{31} & d_{31} & d_{33} & 0 & 0 & 0 \end{bmatrix}. \tag{2.6}$$

This knowledge can now be used to create a simple reference tool when discussing whether a particular nonlinear conversion process is physically possible in a given crystal. For the simpler case of SHG, the nonlinear polarisation, P_i, of the generated frequency is

$$\begin{bmatrix} P_x(\omega_3) \\ P_y(\omega_3) \\ P_z(\omega_3) \end{bmatrix} = 2\epsilon_0 d_{il} \begin{bmatrix} E_x(\omega_1)^2 \\ E_y(\omega_1)^2 \\ E_z(\omega_1)^2 \\ 2E_y(\omega_1)E_z(\omega_1) \\ 2E_x(\omega_1)E_z(\omega_1) \\ 2E_x(\omega_1)E_y(\omega_1) \end{bmatrix} \tag{2.7}$$

where it is preferential to work with the d_{33} coefficient as it is the largest nonlinear coefficient in the crystal at 25.7 pm/V at 832 nm [27]. The d_{33} element can be utilised through propagation in the x-direction of the $LiNbO_3$ crystal using vertically polarised light in a z-cut wafer. This is the so-called extraordinary axis and the second harmonic wavelength is also extraordinarily polarised. The process which is sometimes employed for photon entanglement uses the d_{24} coefficient (represented as d_{31} in equation 2.6) for ordinary-axis polarisation light to be converted into one extraordinary photon and one ordinary photon in the down-conversion regime. LN has a d_{31} coefficient of 4.9 pm/V, making this process substantially less efficient than SHG for comparable input powers. To make use of any nonlinear optical process, it should be noted that both energy and momentum should be conserved as will be described in section 2.3.

2.2.1 The nonlinear coefficient, d

The nonlinear coefficient derived from the polarisation susceptibility is typically evaluated experimentally but there also exist empirical rules which were designed in early nonlinear optics research to assist crystallographic researchers in their efforts to develop crystals which would have a high nonlinearity. This was primarily defined by the efforts of Miller in his seminal paper in 1964 [28]. Thence, there was incentive to perfect a crystal growth process flow prior to performing the highly precise experiments to evaluate the usefulness of the experimental material. The dipole response which gives rise to the nonlinear susceptibility within a material is inherently dependent upon the frequency of the radiation but for

$$d_{ijk} = \epsilon_0 \chi_{ii}^{\omega_3} \chi_{jj}^{\omega_1} \chi_{kk}^{\omega_2} \delta_{ijk}, \tag{2.8}$$

where χ_{ii} in this case represents the linear susceptibility i.e., the diagonal elements of the linear susceptibility matrix and

$$\chi_{ii} = n_i^2 - 1. \tag{2.9}$$

where n_i is the linear refractive index and i is the direction of linear polarisation. As a slight aside, this relation to linear refractive index is the basis of the assumption required for the Kleinman symmetry condition to hold true. In addition to crystal development, one can see the usefulness of this equation in estimating the nonlinear coefficient of a DFG process perhaps where a longer wavelength, likely to be mid-infrared, is not directly available for characterising a nonlinear crystal in the SHG configuration. δ_{ijk} is the quantity defined by Miller [28] in which he predicts a constant, frequency independent parameter that deviates by only a factor of 2 between all non-centrosymmetric crystals. As will be obvious by the end of this thesis, the SHG process is considered the simplest phenomena for optical characterisation due to the degeneracy of input wavelengths and beam diffraction in an experimental setup. A thorough investigation of Miller's empirical relation was carried out by Alford and Smith [29]. They found there to be good agreement with this simple model for a variety of crystals: KDP, KTP, KTA $KNbO_3$, $LiIO_3$, $LiNbO_3$, BBO and LBO. Without detailing their finer points, Alford and Smith, however, did not characterise the δ_{ijk} associated with the d_{33} coefficient of $LiNbO_3$ for the ee → e interaction principally used in the work presented in Chapters 4, 5 and 6.

Due to this complexity and the lack of a δ_{ijk} coefficient for the most common nonlinear interaction currently used for $LiNbO_3$, evaluations of d or the effective nonlinear coefficient, d_{eff}, are not commonly reported in literature on this topic. This is for a range of reasons including, but not limited to, the overly careful experimental procedures required to make this measurement and the limited usefulness since $LiNbO_3$ is already accepted to be one of the most versatile nonlinear crystals for $\chi^{(2)}$ interactions. Nevertheless, Murray *et al.* [30] provided an estimate of d_{eff} for a DFG process utilising 1065 nm, ~1560 nm and 3400 nm as 11 pm/V. Using the refractive index parameters presented in section 2.3.2, a δ_{ijk}=0.029 m^2/C can be calculated. While this is the only detail available from literature to extract this value, to the knowledge of this author, Murray *et al.* acknowledge their calculation of d_{eff} may be significantly biased due to the offset in position of the focal points of the beams within the crystal, CW light present in the pulsed sources, and rise time of the implemented pulses. While the true practicality of this parameter lies in the development of new materials, it is a useful consideration when dealing with far-infrared signals as the lower refractive index will reduce the conversion efficiency.

2.2.2 Nonlinear generation terminology used in this report

This thesis uses a variety of $\chi^{(2)}$ processes so I will begin with clarifying some of the often colloquial terminology found throughout. When utilising the comparatively simple process of SHG, the longer wavelength which seeds the process will be called the pump. The generated shorter wavelength (exactly double the frequency by definition) will be commonly refered to as the signal.

In other $\chi^{(2)}$ processes such as DFG or SFG, the shortest wavelength will typically be called the pump and the other two frequencies will be referred to as the signal and idler, where the longest wavelength is usually denoted as the idler. It is widely accepted the

Table 2.1: Conventional nomenclature for the polarisations involved in a nonlinear process.

Process name	Involved polarisations
Type-0	ee $\longrightarrow$ e
Type-1	ee $\longrightarrow$ o oo $\longrightarrow$ e
Type-2	eo $\longrightarrow$ o eo $\longrightarrow$ o

differential between the signal and idler simply adds to confusion and is why A. Smith [25] simply refers to them as red1 and red2. In this chapter, I will use the subscript notation of 1 and 2 for lower energy beams and 3 to denote the highest energy/shortest wavelength in the interaction, i.e., $\omega_3 > \omega_{1/2}$. The exception to this will be the special case of SHG, where it is useful to only present two parameters and so a subscript notation of 1 and 3 is sufficient.

Additionally, there is some convention with regards to naming the polarisations involved in a three-photon nonlinear interaction. As these may be regularly referred to in this thesis and/or the review of prior art in this area of research, the three most common interactions are listed in table 2.1. They are listed in the table assuming a SFG interaction with regards to directionality of the arrow. As standard in the discussion of birefringent crystals, the *e* and *o* subscripts denote the extraordinary and ordinary axes, respectively.

2.3 Techniques for phasematching in three-photon interactions

One of the foremost issues to tackle in stimulating nonlinear optical processes is material dispersion, commonly referred to as the phasematching condition for momentum conservation. The photon momentum vector is defined as

$$k = \frac{2\pi n}{\lambda}. \tag{2.10}$$

where all parameters have their usual meaning. Generally, there exists two terms which are used to represent routes to phasematching a nonlinear process; critical and non-critical phasematching. Critical phasematching is achieved by angle tuning a crystal and using the crystal's birefringence to modify the observed refractive index of a propagating beam. This is known as birefringent phasematching. Non-critical phasematching is comparatively insensitive to angle alignment and all beams propagate perpendicular to the crystal facet. One method to achieve this is to employ a quasi-phasematching

(QPM) technique to account for the mismatch in photon k-vectors due to dispersion. As a result of its versatility, QPM is the phasematching method used for all experimental work in this thesis. Hence, birefringent phasematching will be briefly explained prior to an in-depth discussion of QPM principles. A third common route to achieve k-vector phasematching is through dispersion engineering of waveguide technologies. This method will not be addressed in this review but further information can be found in refs. [31, 32, 33].

2.3.1 Birefringent phasematching

As described above, birefringent phasematching first method used to phasematch a parametric interaction. This method constructs a scenario where the pump and signal photons remain in phase whilst propagating through the material via careful selection of the propagation direction. While this technique provides many possibilities, it can be restrictive with regards to wavelengths available and which nonlinear coefficient can be used. For a negative uniaxial crystal $n_e < n_o$, and vice versa for positive uniaxial crystals. As a specific example, $LiNbO_3$ is a negatively uniaxial crystal and quartz is positively uniaxial. The phasematching condition is [23]

$$\frac{1}{n_e^2(\theta)} = \frac{\sin^2\theta}{n_e^2} + \frac{\cos^2\theta}{n_o^2} \tag{2.11}$$

For simplicity, this is realised in the case of SHG by imagining a fundamental beam polarised to the slow axis in a crystal and, a second harmonic wave generated polarized to the fast axis such that

$$n_{\text{slow}}(\omega_1) = n_{\text{fast}}(2\omega_1, \theta). \tag{2.12}$$

in the so called type-1 interaction. Typically the index elipsoid [34], an example is presented in figure 2.3, is used to visualise this relation and how phasematching can occur due to changing the input beam direction of propagation through a crystal. It should also be noted there also exists a class of crystals have that biaxial birefringence and may be phasematched for nonlinear interactions. Examples of these include KTP, LBO and $KNbO_3$ and angle for birefringent phasematching requires further consideration [25].

Birefringent phasematching is still utilised in commercial and research applications where the properties of the materials are favourable. For example, BBO has a transmission range from 198 to 2600 nm [35] and LBO has a damage threshold approximately 40 times that of lithium niobate [36], making these materials an attractive option for a variety of applications regardless of their lower nonlinear coefficients. As the path of propagation

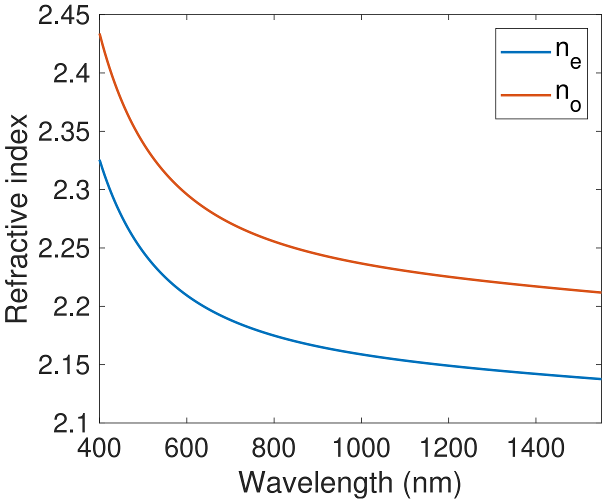

FIGURE 2.2: Dispersion profile of 5%MgO:LN for both n_e and n_o. This is an example of a negative uniaxial crystal.

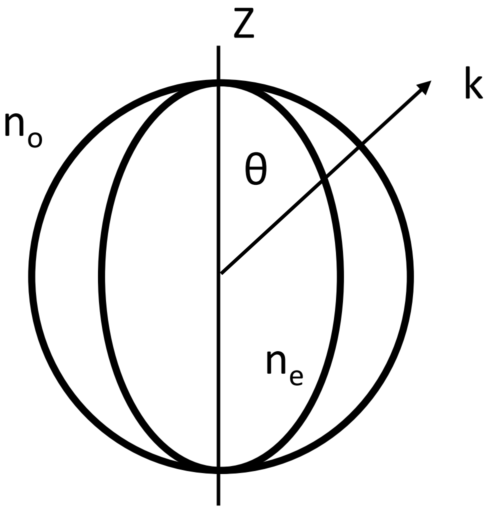

FIGURE 2.3: Simplified refractive index ellipse associated with a negative uniaxial crystal. Quickly demonstrates the constant ordinary refractive index and that phase-matching can occur through modification of the observed extraordinary index through angle tuning. Adapted from [25].

in the crystal is at an angle to the crystal axes, the effective nonlinear coefficient is potentially reduced further as it is the result of a combination of the coefficients presented in equation 2.5. As BBO and LBO are not ferroelectric, there is no route to easily reverse the direction of the nonlinear coefficient, which is the underlying principle of QPM. Additionally, one of the limiting factors which essentially drove research away from birefringent phasematching is the so-called phenomena of spatial walk-off. For the case of SHG, this is where the pump and signal propagate at different angles in the crystal. This leads to a limited crystal length possible as the continuous generation of signal results in a highly elliptical beam and a lower conversion efficiency than may be theoretically expected prior to considering walk-off. Although this is not always a consideration as the crystal length will be restricted in short laser pulse applications to avoid unwanted effects such as temporal walk-off.

2.3.2 Quasi-phasematching

Quasi-phasematching was proposed in 1962 [3], soon after the invention of the laser [1] when the light intensities required to access higher optical harmonics were suddenly attainable. Essentially, QPM is implemented by a periodic reversal of the second order nonlinear coefficient, d, of which the previous sections have been largely concerned. At this point, it is worth mentioning that QPM may be implemented via utilising ferroelectric materials where the application of an electric field appropriately modifies the crystal structure. Other implementations in non ferro-electrics including wafer-stacking or patterned crystal growth renders QPM possible in materials with desirable transmission windows [37, 38, 39]. Evidently, QPM has allowed for great advances to be made in the field of nonlinear optics. QPM has brought crystals such as lithium niobate [40, 41, 42] and potassium titanyl phosphate (KTP) [43, 44, 45] to the forefront of nonlinear optics research; predominantly as this unlocks their entire transmission window for application. The experimental nuances associated with the ability to perform this periodic reversal of the d parameter will feature in Chapter 3.

The fundamental principal of QPM relies on the fact the periodic domain reversal allows for a correction in the momentum offset between the input and generated photons. At this point, it is useful to graphically demonstrate phasematching through phasor diagrams. Although there are many styles of this, I portray this in figure 2.4 where the arrow directionality depicts phase mismatch after propagation through the nonlinear crystal. For a non-phasematched system (which is the case for a crystal prior to implementing a QPM technique), there is a coherence length, L_C, in which there exists optical harmonic generation before the beams accumulate a full π phase shift with respect to one another. At that point, energy in the generated frequencies is back-converted into the fundamental frequency as energy conservation must still be adhered to i.e., full power is initially back-converted when $\Delta kz = \pi$. This description forms the circle which is created in the non-phasematched case of the phasor representation. Perfect phasematching is hence a straight, horizontal line of power growth. Finally, QPM is represented by disjointed semi-circles in which the nonlinear coefficient is reversed at L_C in order to maintain electric field growth.

Periodic reversal of $d$eff allows for the creation of a momentum vector to phase match between the input field(s) and the generated electric field(s), similar in concept to what was achieved in a birefringent phasematching crystal. For the general case of SFG, the momentum mismatch is

$$\Delta k = k_1 + k_2 - k_3. \tag{2.13}$$

Likewise, the DFG momentum mismatch is given as

$$\Delta k = k_3 - k_1 - k_2, \tag{2.14}$$

of which the sign of the momentum vector simply implies directionality for consistency with figure 2.1. This is convention typically used and is otherwise consistent with equation 2.13. Equation 2.13 simplifies in the case of SHG to

$$\Delta k = 2k_1 - k_2, \tag{2.15}$$

The phasematching condition for this process and its relation to the coherence length is commonly given as

$$\Lambda = 2L_C = \frac{2\pi}{\Delta k} = \frac{\lambda}{2(n_\lambda - n_{2\lambda})}. \tag{2.16}$$

The refractive index can be calculated for each wavelength using the corresponding Sellmeier equation and the correct coefficients. For 5% magnesium doped lithium niobate (MgO:LN) the Sellmeier coefficients are available from Gayer *et. al*[46], table 2.2. This is the particular variation used in this work. The corresponding equation for both refractive indices is

$$\begin{aligned} n_{e/o}^2 &= a_1 b_1 f + \frac{a_2 + b_2 f}{\lambda_i^2 - (a_3 + b_3 f)^2} + \frac{a_4 + b_4 f}{\lambda^2 - a_5^2} - a_6 \lambda^2 \\ f &= (T - 24.5°\text{C})(T°\text{C} + 570.82). \end{aligned} \tag{2.17}$$

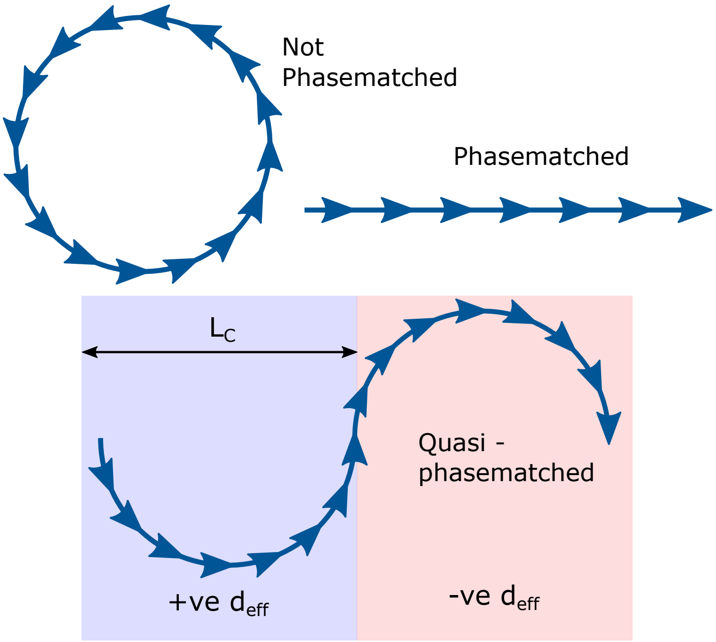

FIGURE 2.4: Phasor representation of phasematching in nonlinear optical generation. The growth of the harmonic field is demonstrated by horizontal travel of the phasors.

TABLE 2.2: Sellmeier coefficients for congruent 5% MgO:LN from Gayer *et. al*[46].

Parameter	n_e	n_o
a_1	5.756	5.653
a_2	0.0983	0.1185
a_3	0.2020	0.2091
a_4	189.32	89.61
a_5	12.52	10.85
a_6	1.32×10^{-2}	1.97×10^{-2}
b_1	2.860×10^{-6}	7.941×10^{-7}
b_2	4.700×10^{-8}	3.134×10^{-8}
b_3	6.113×10^{-8}	-4.641×10^{-9}
b_4	1.516×10^{-4}	-2.188×10^{-6}

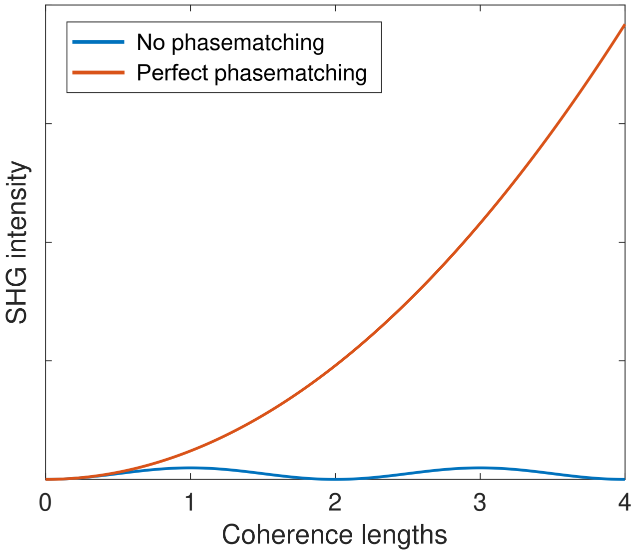

FIGURE 2.5: Generation of SHG intensity comparing a phasematched crystal to a crystal with no phasematching.

Knowledge of the refractive index of the respective wavelengths present in the parametric process is the final information required to enforce the phasematching condition for QPM. For the case of SHG, this condition was given in equation 2.16 where the relation to refractive index is explicitly denoted.

2.3.2.1 Three-wave coupled mode theory

The plane-wave, three-wave interaction theory for $\chi^{(2)}$ materials is well understood and can be represented by three relatively straightforward coupled-mode equations. These can be used to illustrate the conversion process from one or more input electric fields into a converted wavelength. The coupled-mode equations can be used to demonstrate the effect of different poling orders, the unpoled scenario and the conversion characteristics at wavelengths around the phase matched wavelength. To gain an understanding of where these equations come from and how they result in amplitude growth of a generated electric field, one starts with the standard wave equation and use this as a starting point. While there are many sources discussing this topic, the mathematical notation in this section will be kept relatively consistent with Boyd [23]. The wave equation is given as

$$\nabla^2 E - \frac{\epsilon^1(\omega)}{c^2}\frac{\partial^2}{\partial t^2}E = \frac{1}{\epsilon_0 c^2}\frac{\partial^2 P^{NL}}{\partial t^2}. \tag{2.18}$$

For consistency with future chapters, primarily Chapter 5, I substitute the mathematical notation for momentum vectors from k to β. This is the common notation for this parameter in reference to optical waveguides and is defined as

$$\beta = \frac{2\pi n_{\text{eff}}}{\lambda} \tag{2.19}$$

where $n_{\text{core}} > n_{\text{eff}} > n_{\text{clad}}$ and n_{eff} is dependent on the waveguide mode in question. Further details on solutions to propagating modes in waveguides can be found in Okamoto [47], Ghatak and Thyagarajan [48] or in the following theses [49, 50]. Following from this, the electric field of the travelling wave is defined as

$$E_i(z,t) = A_i(z)\exp\left[i(\beta_i z - \omega_i t)\right] \tag{2.20}$$

As we have assumed the electric field is independent of x and y, i.e., only changes in the direction of propagation. This enables the simplification of ∇^2 to $\frac{\partial^2}{\partial z^2}$. Due to the dependence of A_3 on the propagation distance, the differentiation is more apparent as a two-step process. The first-derivative of the first term of equation 2.18

$$\frac{\partial E(z,t)}{\partial z} = \frac{\partial A_3}{\partial z}\exp\left[i(\beta z - \omega t)\right] + i\beta A_3 \exp\left(i(\beta z - \omega t)\right) \tag{2.21}$$

and the second derivative is given as

$$\begin{aligned}\frac{\partial^2 E_3(z,t)}{\partial z^2} =& \left(\frac{\partial A_3}{\partial z}\right) ik_3 \exp\left[i(\beta_3 z - \omega_3 t)\right] + \left(\frac{\partial^2 A_3}{\partial z^2}\right)\exp\left[i(\beta_3 z - \omega_3 t)\right] + \\ & \left(\frac{\partial A_3}{\partial z}\right) ik_3 \exp\left[i(\beta_3 z - \omega_3 t)\right] + A_3 i^2 k_3^2 \exp\left[i(\beta_3 z - \omega_3 t)\right]\end{aligned} \tag{2.22}$$

and simplifying to

$$\frac{\partial^2 E_3(z,t)}{\partial z^2} = \exp\left[i(\beta_3 z - \omega_3 t)\right]\left(\frac{\partial^2 A_3}{\partial z^2} + 2i\beta_3\frac{\partial A_3}{\partial z}\right) \tag{2.23}$$

The second term from equation 2.18 is straightforward with only a single parameter dependent on time. Hence the second term becomes

$$\frac{\partial^2 E_3(z,t)}{\partial t^2} = \frac{-\epsilon^{(1)}\omega_3^2}{c^2} A_3 \exp\left[i(\beta_3 z - \omega_3 t)\right] \tag{2.24}$$

$$\frac{\partial^2 E_3(z,t)}{\partial t^2} = -k_3^2 A_3 \exp\left[i(\beta_3 z - \omega_3 t)\right]. \tag{2.25}$$

where $\epsilon^1 = n_1^2$.

The RHS can be solved given the definition of nonlinear susceptibility,

$$P_3 = 4\epsilon_0 d_{\text{eff}} E_1 E_2 \tag{2.26}$$

$$\frac{1}{\epsilon_0 c^2}\frac{\partial^2 P}{\partial t^2} = \frac{-4id_{\text{eff}}\omega_3^2 A_1 A_2}{c^2}\exp\Big(i((\beta_1+\beta_2)z - (\omega_1+\omega_2)t)\Big) \tag{2.27}$$

While the LHS and RHS of the wave equation, equation 2.18, have now been analytically expanded, they are still in an impractical format. Some key points can be made to assist in simplifying further. It is noted that $\omega_3 = \omega_1 + \omega_2$, and this substitution can be made in the final term of equation 2.27. Hence, the exp $(i\omega_3 t)$ terms cancels from the expression. Additionally, dividing across by $\exp(i\beta_3 z)$ combines the exponential terms into a single term on the RHS. The simplified wave equation can now be written as

$$\frac{\partial^2 A_3}{\partial z^2} + 2i\beta_3\frac{\partial A_3}{\partial z} = \frac{-4d_{eff}\omega_3^2}{c^2} A_1 A_2 \exp\left[i(\beta_1+\beta_2-\beta_3)z\right] \tag{2.28}$$

The slowly varying amplitude approximation commonly used throughout wave equation simplifications in electromagnetism can now be implemented. Essentially, this assumes

$$\frac{\partial^2 A_3}{\partial z^2} \ll \frac{\partial A_3}{\partial z} \tag{2.29}$$

and we can neglect the term containing the second-derivative of A_3. Finally, we have

$$\frac{\partial A_3}{\partial z} = \frac{2id_{eff}\omega_3^2}{\beta_3 c^2} A_1 A_2 \exp\left(i\Delta\beta z\right). \tag{2.30}$$

Similarly, the ODEs for the input beams A_1 and A_2 can be derived and are given as

$$\begin{aligned} \frac{\partial A_1}{\partial z} &= \frac{2id_{eff}\omega_1^2}{\beta_1 c^2} A_3 A^*{}_2 \exp\left(-i\Delta\beta z\right) \\ \frac{\partial A_2}{\partial z} &= \frac{2id_{eff}\omega_2^2}{\beta_2 c^2} A_2 A^*{}_1 \exp\left(-i\Delta\beta z\right) \end{aligned} . \tag{2.31}$$

At this point, it is appropriate to determine the analytical solution of such an equation. The purpose of this is to explain the function which is often presented as the data resulting from a standard characterisation of a waveguide with a non-negligible $\chi^{(2)}$ parameter. Taking the integral of equation 2.30 and combining all the constants into a single term, γ, we find

$$\begin{aligned} |A_3(L)|^2 &= \gamma \left| \int_0^L \exp\left(i\Delta\beta z\right) \right|^2 \\ &= \gamma \left| \frac{\exp\left(i\Delta\beta L\right) - 1}{i\Delta\beta} \right|^2 \\ &= \gamma L^2 \left(\frac{\exp\left(\Delta\beta L\right) - 1}{i\Delta\beta L} \right) \left(\frac{\exp\left(-i\Delta\beta L\right) - 1}{i\Delta\beta L} \right) \end{aligned} \tag{2.32}$$

The imaginary i in the denominator can dropped within the absolute value bars before the expansion, of which in this case is recognised as a multiplication of the equation with its complex conjugate. Continuing,

$$\begin{aligned} |A_3(L)|^2 &\propto 2L^2 \frac{1 - \cos(\Delta\beta L)}{(\Delta\beta L)^2} \\ &= L^2 \frac{\sin^2(\Delta\beta L/2)}{(\Delta\beta L/2)^2} \\ &= L^2 \text{sinc}^2 \left(\frac{\Delta\beta L}{2} \right) \end{aligned} \tag{2.33}$$

Assuming the phasematching condition has been achieved in a waveguide, the power generated through SHG is vastly dependant on the electric field overlap between the guided pump mode and the generated mode. The generic mathematical relationship of SHG generated power, P_3, to the input power, P_1, is presented as

$$P_3 = P_1 \tanh^2(\Gamma L) \tag{2.34}$$

where the so-called nonlinear drive is defined as

$$\Gamma = \left(\frac{8\pi^2 d_{\text{eff}}^2 \mathfrak{I}_{ov}^2}{\lambda_1^2 \epsilon c n_{\text{eff}}^3} P_1 \right)^{1/2}. \tag{2.35}$$

The nonlinear overlap integral, $\mathfrak{I}_{ov}$, is found in the nonlinear drive parameter and is formally defined as

$$\mathfrak{I}_{ov} = \frac{\iint\limits_{-\infty}^{\infty} E_3(x,y) E_1^2(x,y)\, dx dy}{\left[\iint\limits_{-\infty}^{\infty} E_3^2(x,y)\, dx dy \right]^{1/2} \iint\limits_{-\infty}^{\infty} E_1^2(x,y)\, dx dy}. \tag{2.36}$$

However, equation 2.34 is a universal description of the SHG power profile from the low-conversion regime towards complete conversion of the input radiation. In the low-conversion efficiency regime and assuming negligible propagation loss for both wavelengths, P_3 is given as [9]

$$P_3 = \frac{8\pi^2 d_{\text{eff}}^2 \mathfrak{I}_{ov}^2}{\lambda_1^2 \epsilon_0 c n_{\text{eff}}^3} P_1^2(z=0) L^2 \tag{2.37}$$

Some potentially inconvenient conclusions arise from analysing the overlap integral. As the integral involves electric fields rather than intensity profiles, anti-symmetric functions may theoretically lead to a net-zero numerator of the overlap integral equation; this is dependent on the respective polarisation for each propagating wavelength. Thence, some modes may not present themselves during experimental characterisation; however a non-uniform d_{eff} caused by the diffusion profile of the material used to create the refractive index increase may lead to the revival of these generated modes. The various types of PPLN waveguides used in the literature are discussed in the following chapter, section 3.4.

2.3.2.2 QPM grating structures

Via QPM, the crystal structure is re-engineered to achieve a conservation of momentum between the design wavelengths and a net gain in signal intensity. For the case of SHG, this will essentially maximise the relationship given in equation 2.33. This can be achieved through a variety of grating patterns but the simplest of which are 1st and 3rd order periodic domain reversal, as seen in figure 2.6. For the special case of SHG, the numerical solution of equations 2.31 and 2.30 is illustrated in figure 2.7(a) to demonstrate the intensity growth of the SHG signal as a function of crystal length, which is represented as the number of coherence lengths into the crystal, for both 1st and 3rd order gratings. Whilst it appears QPM is less efficient than birefringent phasematching by a factor of $2/\pi$, it enables the use of a larger nonlinear coefficient, d_{33}, in lithium niobate. As mentioned previously, the greater range of capability makes QPM materials the ideal candidate for bespoke applications. It is clear that a first order grating is more efficient for wavelength conversion than a third order grating, as seen in figure 2.7(a). Nevertheless, this may be required for some applications if fabricating smaller periods is beyond the capabilities of the patterning or poling technologies. A numerical example using the couple-mode equations can be seen in figure 2.7(b) for a PPLN crystal which is phasematched for SHG of 780 nm light to 390 nm (chosen as an example due to the application presented in Chapter 4); this is equivalent to the analytical solution given in equation 2.33 for this particular parametric process. While the analytical solution is computationally less taxing, numerically working with the ODEs allows for the potential to investigate apodised or chirped gratings or a variable $\Delta\beta$ along the propagation axis, which will enable the work discussed in Chapter 5.

Table 2.3 contains the poling periods, Λ, required for SHG of some commercially available pump wavelengths (1560 nm and 1064 nm) and then the wavelengths of interest in Chapter 4 (780 nm) and that of interest in Yb^+-ion trapping (739 nm). Operating at these dimensions for domain inversion add extra challenges to the fabrication of such a device.

As may be inherently assumed by this point, quantum mechanics and the quantisation of photons is a key point when discussing the limitations of some nonlinear optical processes. While the work in this thesis will not directly investigate the role of pump-depletion, such as a previous thesis in this research group [51], the conservation of photon number is a vital part to any discussion of nonlinear optics. The relation to

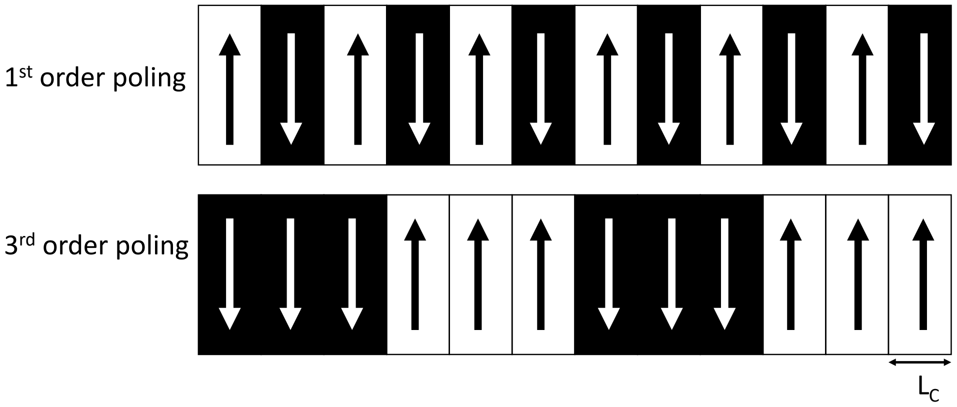

FIGURE 2.6: Definition of the structures referred to as 1^{st} and 3^{rd} order gratings which can be imprinted onto lithium niobate as a method of phase matching. Arrows represent the spontaneous polarisation direction of the crystal.

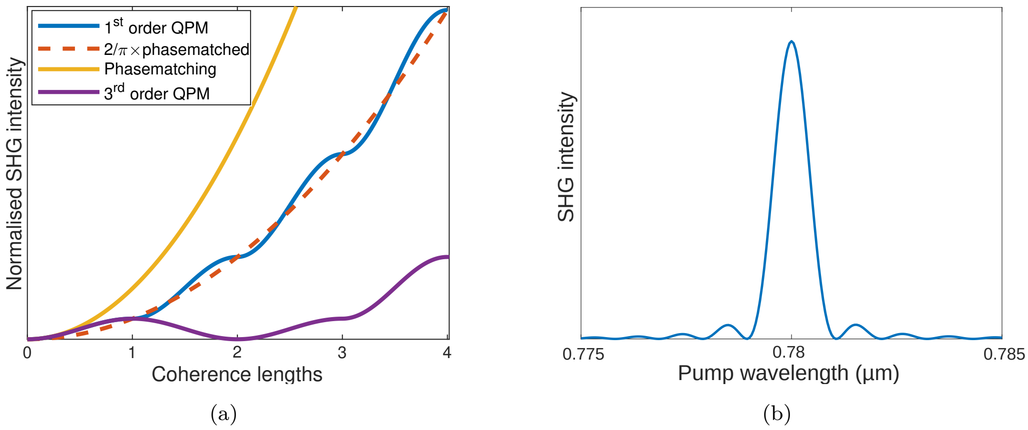

(a) (b)

FIGURE 2.7: (a) Relationship between perfect phasematching and the first and third order poling technique for SHG conversion efficiency using the three-photon coupled-mode equations. It is clear that first order QPM is a factor $2/\pi$ less efficient than perfect phasematching but greater flexibility in applications prove it to be advantageous. (b) Characteristic sinc^2 curve in the vicinity of the phasematching wavelength which has been numerically constructed via the three-photon coupled mode equations.

TABLE 2.3: Calculated poling periods required for SHG of the pump wavelength for some commercial 5mol%MgO:PPLN chips and the wavelengths investigated in this work. All periods correspond to a PPLN crystal at room temperature.

Pump wavelength (nm)	Λ (µm)
1560	19.73
1064	6.98
780	2.44
739	1.99

mathematically present this result is commonly given as

$$\frac{d}{dz}\left(\frac{I_2}{\omega_2}+\frac{I_3}{\omega_3}\right)=\frac{d}{dz}\left(\frac{I_1}{\omega_1}+\frac{I_3}{\omega_3}\right)=\frac{d}{dz}\left(\frac{I_1}{\omega_1}-\frac{I_2}{\omega_2}\right). \tag{2.38}$$

These set of equations are known as the Manley-Rowe relations [52]. They are a semi-classical description implying the conservation of photons in any parametric process, such as those illustrated in figure 2.1. This relation will inherently be adhered to in the three-photon numerical coupled-mode theory, equations 2.30 and 2.31, but it provides an analytical relation which has been applied as a method of enforcing energy conservation in a range of applications, from electrical circuits to atmospheric physics.

2.4 Nonlinear optic focussing conditions

Although a considerable portion of this thesis is dedicated to the development of novel waveguiding structures (Chapters 4 and 5) there is still much work to be done in this development when vastly different wavelengths are hypothetically guided in a single device. Büchter *et al.* achieved this via photolithographically-defined indiffused, tapered waveguides to assist launching conditions and then to guide a mid-IR beam [53]. At the University of Southampton, we focus on scalable waveguide architectures based on ultra precision machining which is limited to straight ridges; the literature and advantages of waveguides will be discussed in section 3.4. Hence, bulk focussing conditions are still required to utilse and explain the optical design of the the experimental work in Chapter 6.

This area of research has primarily been developed by Boyd and Kleinman [54], Guha and Falk [55] and Tukker *et al.* [56] and further information can be found in these key papers and also the textbook by Boyd [23]. As this research area is well established, it is well known that the efficiency of the nonlinear interaction is proportional to laser focussing conditions and material properties. For the case of SHG, where the pump beam is identical in focussing conditions for the two photons required for this process, the SHG power, P_3 is

$$P_3 \propto P_1^2 L h(\beta, \xi, \mu) \tag{2.39}$$

where h is defined as a function of optimizable variables, L is crystal length and μ is a function of the position of focal point in the crystal. β is related to the spatial walk off constant in the crystal of which only decreases the conversion efficiency when non-zero. $\xi = l/b$ and b is the confocal parameter,

$$b/2 = z_R = \frac{n\pi w_0^2}{\lambda}, \tag{2.40}$$

and z_R is the Rayleigh length of a beam, corresponding to the distance from focus in which the beam expands to a factor of $\sqrt{2}$ larger than at the focal point. Setting the walk-off parameter to be negligible and the focus at the centre of the crystal, Boyd and Kleinman concluded the maximum efficiency was found when $h = 1.068$ and $\xi = 2.84$. These assumptions are relevant in for application to QPM crystals as the direction of propagation in the crystal is perpendicular to the facet. This establishes that the confocal parameter should be designed to be comparable to the crystal length, if possible, for an efficient nonlinear conversion.

Guha and Falk and Tukker *et al.* describe the effects of different focussing parameters in non-resonant parametric conversions for the non-degenerate cases of SFG and DFG, respectively. Both articles develop on the seminal work carried out by Boyd and Kleinman. Respectively, both works also conclude the conditions for an efficient SFG or DFG is to have an approximately equal Rayleigh range for both input beams and focus at the centre of the crystal.

2.4.1 Gaussian beam methodology

The theory of Gaussian beam propagation has been thoroughly discussed in a number of texts. This short section does not intend to justify the entire theory but is included for completeness in terms of the extent of which it has been used in this thesis; this theory is primarily used in the experiment presented in Chapter 6, to achieve a relatively efficient nonlinear interaction, as per section 2.4. The so-called ABCD matrices provide a route to numerically model and design a laser's profile as it passes through various optical components. The convenience of this method lies in the simplicity of compounding matrix multiplication as more optical components are added to a design. This method was initially proposed by Kogelnik and Li in 1966 [57].

TABLE 2.4: Examples of the operation and corresponding matrix associated with the ABCD method for optical design

Optical operation	Matrix
Distance travelled	$\begin{bmatrix} 1 & d \\ 0 & 1 \end{bmatrix}$
Thin convex lens	$\begin{bmatrix} 1 & 0 \\ -1/f & 1 \end{bmatrix}$
Refraction	$\begin{bmatrix} 1 & 0 \\ 0 & n_1/n_2 \end{bmatrix}$
Curved mirror	$\begin{bmatrix} 1 & 0 \\ 1/R(n_1/n_2-1) & n_1/n_2 \end{bmatrix}$
Curved boundary	$\begin{bmatrix} 1 & 0 \\ -2/R\cos(\theta) & n_1/n_2 \end{bmatrix}$

$$\frac{1}{q(z)} = \frac{1}{R(z)} - \frac{i\lambda}{z_R} \tag{2.41}$$

The matrices are multiplied and a single matrix can be used to characterise the beam at any point. Letting this final matrix be known as G, it is typical for literature on this method to show

$$G = \begin{bmatrix} A & B \\ C & D \end{bmatrix}, \tag{2.42}$$

which is where the name of this method is derived from.

The complete transformation of a beam through any arbitrary optical system can be represented by q_2,

$$q_2 = \frac{Aq_1 + B}{Cq_1 + D}. \tag{2.43}$$

where the initialisation of the imaginary component using some known or measured beam parameters allows for the creation of the beam in a numerical model; since the Rayleigh length z_R is known from equation 2.40.

$$w^2 = \frac{|\mathrm{Im}(q_2)|\lambda}{\pi n}, \tag{2.44}$$

being careful to select the refractive index of the material the beam is being evaluated in and not simply letting the refractive index equal 1, as this term is commonly ignored in laser cavity design of which the ABCD method is mostly described for. This will be in addition to an angle, θ, if a beam is not collimated. This is calculated utilising the small angle approximation,

$$\theta = \frac{\lambda}{n\pi w}, \tag{2.45}$$

where n in this equation will typically equal 1 as θ will be of concern in the collimation of a free space beam, rather than inside a PPLN crystal. This brief introduction to some simple Gaussian optics is the extent that will be used in this thesis. Further usage of the ABCD matrix method for requirements such as laser cavity design and stability can be found in any of the following sources [58, 59, 60].

2.5 Conclusion

This chapter has covered some of the underlying theoretical concepts for QPM, specifically regarding PPLN, which is one of the most academically and commercially prominent $\chi^{(2)}$ materials. This discussion has included the expectations of experimental results when we tune around the phasematching point via temperature or frequency of the source and the corresponding mathematical formulation; this will provide the basis of the work in Chapter 5. We are now in a position to discuss some of the fabrication and technological aspects and challenges for creating PPLN and the work other research groups have achieved in the literature on this topic.

Chapter 3

Fabrication of QPM crystals and nonlinear waveguides

3.1 Introduction

Having been first introduced as a theoretical concept more than half a century ago [3] and successfully demonstrated in the early 1980's [41, 42, 61], QPM technologies are still at the forefront of academic research with a range of new applications and fabrication techniques being presently investigated. This chapter will discuss some of the current research and competitive technologies, including the choice of nonlinear materials, ferroelectric domain reversal methods and waveguide technologies.

For a thorough review of QPM devices and historical progression, the reader is directed to a review paper by Hum and Fejer [62], whom provide preliminary details on all aspects from other choice materials and the applications of different grating designs. While the focus of this literature review will be on more recent developments in this area of optical engineering, there will be inevitable overlap with mature technologies and honourable mentions of the pioneering work in early research.

3.2 Choice of nonlinear crystal

Lithium niobate is a second order nonlinear material with a high nonlinear coefficient and a broad transmission window, from below 400 nm to above 5 µm. A high degree of success with regards to conversion efficiency has made it a key material in applications for nonlinear crystals and the material in which this chapter, and indeed the rest of this thesis, will primarily be concerned with. However, no discussion of QPM materials would be complete without a comment regarding potassium titanyl phosphate (KTP). This material has gained a vast amount of interest due to its unique dispersion profile which conveniently overlaps with high-quality telecommunications components in the C-band. For primarily this reason, PPKTP has had a surge in usage for quantum optical experiments and theoretical studies [63, 64, 65, 66]. Additionally, the electro-optical properties of KTP are advantageous and will therefore create a commercial drive in production of this crystal.

Lithium tantalate (LT) is a closely related material to LN and has a higher transmissivity at the blue/UV [67] regime but its lower nonlinear coefficient allows for LN to potentially outperform a LT device. Mizuuchi *et. al* have gone as far as demonstrating the generation of 340 nm previously in LN [68]. Table 3.1 summarises some key material parameters for LN and LT. LT also provides the following range of challenges: difficulty in acquiring good quality magnesium doped LT for high power applications, a lesser understanding in the literature for fabricating waveguides, and the requirement of domain inversion procedures to be developed for MgO:LT which is now available commercially in limited quantities. The limited application range has resulted in the development of this material not being prioritised although recent work by Oka [69] has shown promise with the development of PPLT for green generation.

Due to the limited transmission windows of materials which are currently used in a QPM, deep UV generation typically uses birefringent phasematching of bulk BBO or LBO crystals and these have been thoroughly ingrained in commercial systems. On the other end of the electromagnetic spectrum, materials such as orientation-patterned (OP) GaAs [70] and GaP [13] are emerging as a technologies as solutions to the challenges surrounding far-IR sources.

TABLE 3.1: LN and LT Comparison table

Material	d_{33} (pm/V)[27]	Lower wavelength cut-off (nm)	Curie temp. (°C)
LN	25.7	330	1165
5% MgO:LN	28.4	320	1215 [71]
LT	15.1	277	601
7% MgO:LT	?	272	?

Transmission is not the only parameter to be considered when choosing a nonlinear crystal; although sometimes availability and practicality removes many potential options. For example, there are many UV transmissive crystals but maintaining beam quality is vital for applications requiring fibre-coupling of the SHG beam, of which birefringent phasematching methods are susceptible to distorted beam shapes as discussed in section 2.3.1. For the example application of Doppler cooling ions, discussed in Chapter 1 the restraint to operate in the CW regime means the lower peak power of the laser reduces the conversion efficiency vastly. These disadvantages essentially rule out the use of BPM materials in a single-pass configuration. Alongside these facts, the maturity of LN as a commercially available material and the established collaborative partners,

Table 3.2: Commonly available $\chi^{(2)}$ crystals, the usual phasematching method utilised and further notes on the material's applications. For this table, BPM refers to birefringent phasematching.

Crystal	PM method	Notes and key benefits
MgO:LN	QPM	Wide transmission window in a useful range (blue to MIR). High nonlinear coefficient and mature technology
LT	QPM	Preferential transmission in UV. Poling technologies are not as mature and lower nonlinear coefficient
KTP	QPM	High electro-optic coefficients, useful dispersion properties
OP-GaAS/GaP	QPM	Far-IR transmission and very high nonlinear coefficient but challenging to fabricate
BBO	BPM	Deep UV transmission
LBO	BPM	Deep UV transmission, high damage threshold

solidifies it as the most appropriate material choice, at present, for the work in this thesis. An excellent review paper was written by Ebrahim-Zadeh *et al.* [72] primarily for the nonlinear optical application of a 1064 nm fibre lasers but the reasonings behind the choice of crystals for a particular frequency range is coherently presented.

3.2.1 MgO:LN transmission

To provide evidence for the application of LN in the fabrication of devices for nonlinear conversion to UV wavelengths, spectrophotometry was carried out quantify the transmission properties of the specific material used in this work. Differential spectrophotometry is designed for measurements such as this as it considers the Fresnel reflections from the sample in order to remove this from the calculation. The technique requires two different sample thicknesses to undergo the measurement. As a differential spectrophotometer was not available, the transmission spectra were taken directly after one another to limit the effect of the light source drifting in power in a standard spectrophotometer (Varian Cary 500 UV-VIS NIR). 1 mm and 0.5 mm thick 5%MgO:LN samples (Crystal Tech.) were used as they were readily available dimensions. To calculate the propagation loss, α , the power transmission into material is taken to be

$$t = (1 - R)^2 \exp(-\alpha L) \tag{3.1}$$

where R is the associated Fresnel reflection. Taking the ratio of the two thickness, R can be eliminated from the equation and the ratio can be Taylor expanded to

$$\frac{t_1}{t_2} = 1 - \alpha(L_1 - L_2). \tag{3.2}$$

Some straightforward rearranging provides the final equation for propagation loss,

$$\alpha = \left(\frac{1}{L_2 - L_1}\right)\left(\frac{t_1 - t_2}{t_2}\right). \tag{3.3}$$

The raw transmission data and the calculated propagation loss as a function of wavelength are shown in figure 3.1. For the 369 nm light needed for Yb$^+$ ion trapping, MgO:LN has an attenuation coefficient of 0.155 cm^{-1} or 0.67 dB cm^{-1}. This may still be more efficient at 369 nm generation in comparison to LT due to the much higher nonlinear coefficient even considering the higher attenuation. This will be investigated in future work. Doping LN with MgO is currently considered as a requirement for use in nonlinear optics as it reduces the photorefractive damage (PRD) occurring in the crystal. Without MgO, PPLN needs to be operated at temperatures above 90°C to reduce PRD, which is considered too high for most commercial applications. The photorefractive effect occurs in materials which are both electro-optic and photoconductive in which a refractive index change is proportional to the gradient of the input beam intensity. It is accepted that the origin of this effect is due to metallic impurities in the crystal introduced during crystal growth. Excited electrons can locally gather and are

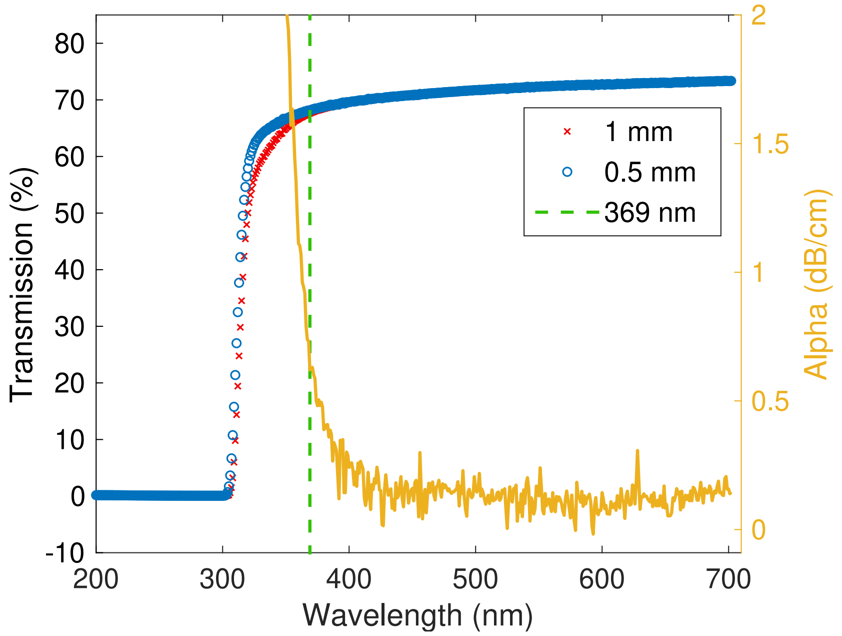

FIGURE 3.1: Transmission data of 1 mm and 0.5 mm thick MgO:LN samples. The dashed line indicates propagation loss value, α, of MgO:LN at the wavelength required for Yb$^+$ ion trapping experiments.

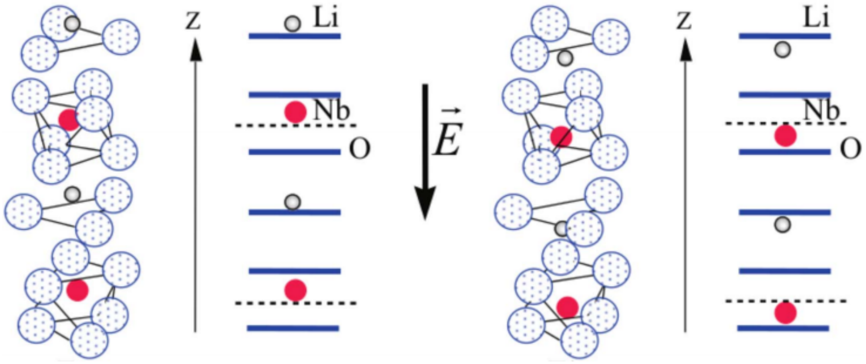

FIGURE 3.2: Location of the Nb and Li ions upon a poling electric field to create the periodic structure of material polarisation reversed sections. Image taken from [73].

unable to redistribute themselves; inducing a highly localised refractive index change via the electro-optic effect. The addition of Mg into the lattice structure increases conductivity and enables redistribution of excited electrons to reduce this photorefractive effect. This allows for the use of higher power lasers to be used to pump a PPLN crystal. Additionally, Mg doping is known to reduce the lower cut-off wavelength for optical transmission. However, Mg is not unique regarding what elements can decrease the effect of photorefraction. This will be further discussed in section 3.4.2.

3.3 Ferroelectric domain inversion in LN

Lithium niobate is a ferroelectric material with a broad transparency range and a high nonlinear coefficient. As will be detailed in the ensuing chapter, the ferroelectric nature of this material enables the versatility of its applicability. This is a result of the quasi-phasematching (QPM) technique which was presented in Chapter 2.

Following the work by Feng *et al.* [40] who successfully periodically poled LN for the first time for SHG of 1.06 µm light, there has been a cohort of success and applications for bulk PPLN devices. This work by Feng *et al.* imposed the periodic structure by temperature fluctuations during the crystal growth. This method was not a viable option for adoption as it required doping the melt with yttrium and a 50/50 duty cycle of the alternating ferroelectric domains. Hence, application of an electric field post crystal growth is more commonly used as the route for modification of the domain structure. The application of an electric field exceeding that of the coercive field, results in displacing the Li ion through the adjacent oxygen plane. This, in turn, repels the Nb ion. As a consequence of this new crystal configuration, the spontaneous polarisation of LN is reversed, providing the sign reversal of the nonlinear coefficient required to achieve QPM and nonlinear generation, discussed in section 2.3.2.

Early poling regimes for the fabrication of high quality PPLN for use as a bulk optical component was carried out here in the University of Southampton [74]. This method of poling uses a standard, positive photoresist which is spun on the -z face, baked, patterned and developed. This photoresist forms the dielectric barrier to enable a periodic path for current to pass through the LN wafer. Electrical contact is made using a gel electrode which moulds into the photoresist openings. This method allows for simpler cleanroom processing steps to be used in contrast to other techniques which used deposited structured metal electrodes.

The poling routine used to fabricate the PPLN used in this work has been discussed in previous works [51, 75] although some steps may be proprietary and are intellectual property of Covesion Ltd. The routine implements a series of high voltage pulses to assist in the creation of local nucleation cites of reversed domains. These pulses are approximately 10 ms in duration. This is followed by a constant voltage just above the coercive field. This two-step process minimises the spreading of domains to avoid domain merging, to an extent, and ensures the domains are able to grow at the same rate.

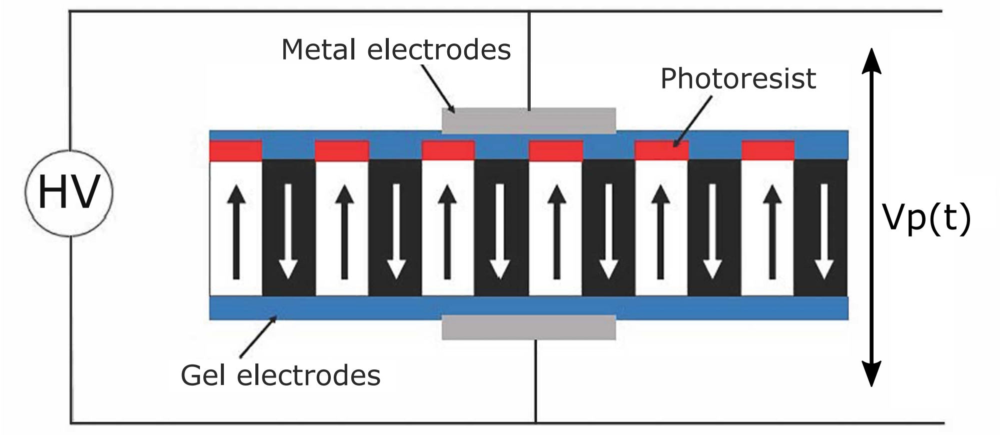

Figure 3.3: Patterning and poling technique used by Covesion Ltd. for the PPLN devices used within this project.

For temperatures below the Curie point of LN, approximately 1100 °C, the metallic ions in the crystal structure sit off-axis from the surrounding oxygen atoms, as shown in figure 3.2. The Curie temperature is the temperature at which the permanent spontaneous polarization orientation is replaced with a net-zero polarization structure as the metallic ions move into the oxygen plane. The permanent structure imprinted on the ferroelectric domains is, hence, erased when the temperature of the crystal is brought above this point. This is key information when high temperature processing steps are being used in the fabrication of LN waveguides, such as those discussed in Chapter 4.

3.3.1 Surface and thin film poling

Certain other reasearch groups worldwide, and for other specific applications, the fabrication of PPLN in which only a few microns on the top surface has a periodic domain

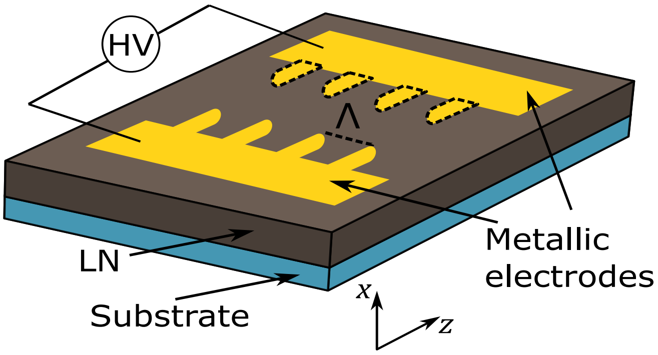

FIGURE 3.4: Simplified schematic of the surface poling techniques used in literature from other research groups. Dashed lines around the electrodes indicate these protruding sections of the electrode is not always present.

reversal may be all that is required. These technologies cannot be used as a bulk crystal in higher power applications or as intra-cavity components but they do serve as a route for high conversion efficiencies via the tightly confined modes of the pump and generated SHG mode profiles.

The directionality of the domain reversal propagation for thin films of LN mean that the crystal is x-cut as per the domain reversal process laid out in figure 3.2. Hence, the linear polarisation launched into any further fabricated waveguide is parallel to the surface of the substrate, the so-called TE mode, to interact with the d_{33} nonlinear coefficient. The substrate beneath is typically either SiO_2 or lithium tantalate; both have refractive indices lower than MgO:LN and the bonding technologies are mature enough to be commercially purchased prior to novel research being undertaken. For example, NANOLN is a commercial manufacturer supplying LN on-insulator (LNOI), supplying films of LN as thin as 300 nm [76].

Varying degrees of success have been achieved using these techniques. For example, Younesi *et al.* [77] does not achieve domain reversal across the entirety of the surface between the electrodes and is hence limited to a single waveguide per sample for further experimentation or application. Following work from the same research group, verified a 90% poling quality where this term is related to the optimal area of the grating but achieved only a 1 µm depth for the domain reversal. Wang *et al.* [11], from Harvard University, demonstrated a surface poling technique using a common surface electrode recipe of a chromium adhesion layer prior to gold deposition; with a total poled area to provide the further fabrication of three waveguides. They achieved a 39% poling duty cycle. However, their strong geometric dispersion in these thin films required a $\Lambda = 4$ µm to phasematch a 1550-775 nm SHG process, approximately one-fifth of the poling period in bulk MgO:PPLN, perhaps providing an additional challenge in applying this technology to blue/UV generation which already requires a vastly reduced poling period.

All of these technologies which enable the poling of thin-film LN play a role in applications moving towards hybridized, integrated photonics platforms. Manipulating the mode size to match the further optical circuitry, which may occur in a high refractive index-contrast platform such as silicon, will permit the reduction in coupling losses between the waveguide technologies.

3.3.2 Commercial availability of periodically poled LN

This brief section is included for completeness and context as to why availability of short period gratings is still of commercial interest. This is not intended to be a complete catalogue and is simply a record of availability on cited websites; each respective company may offer further bespoke components of varying quality. In addition to the quoted poling periods available from Covesion Ltd., table 3.3, and prior to the commencement of the short period work presented in this thesis, they have also demonstrated a bulk 844-422 nm SHG grating as a bespoke sample for academic interests regarding Sr^{+}-ion trapping with a $\Lambda = 3.75$ µm [78].

Table 3.3: Commercial availability of QPM grating periods.

Company	Λ range	SHG wavelength range (nm)
Covesion [79]	5.17 - 35.97	488-1650
HCP [80]	5.17-36.00	488-1700

In addition to these companies, NTT is a well-known supplier of PPLN and waveguiding technologies. Raicol Crystals and Tailored Photons AB are suppliers of PPKTP for operation within the transparency range of KTP, 400 nm to 4000 nm. As a University of Southampton spin-out company, the periodic domain inversion of LN shall be carried out in partnership with Covesion Ltd. for any PPLN devices discussed or used in this thesis. More details on this specific technology may be found in [51, 81].

3.4 Periodically poled LN waveguides

Fabricating waveguides in nonlinear optical materials for $\chi^{(2)}$ processes such as SHG can be significantly beneficial due to the potential to greatly enhance conversion efficiency. The theoretical reasoning for this will be briefly alluded to in this section along with the additional fabrication challenges waveguides provide. Equation 2.37 from section 2.3.2.1, provides a number of criteria for achieving high efficiency waveguides. For an efficient interaction, a high overlap integral between the fundamental and second-harmonic fields is required, it is preferential for propagation loss to be low, α_i, and that the phasematching condition is now dependent on the effective index, n_{eff}, of the waveguide instead of the bulk refractive index. Given this, the equation is adapted to account for propagation loss to ensure an appropriate numerical fit to experimental data; this is given as:

$$P_3 = \frac{8\pi^2 d_{\text{eff}}^2 \Im_{ov}^2}{\lambda_1^2 \epsilon_0 c n_{\text{eff}}^3} P_1^2(z=0) \left(\frac{\exp(-\alpha_1 L) - \exp(-\alpha_3 L/2)}{\alpha_1 - \alpha_3/2} \right)^2 . \tag{3.4}$$

This equation converges to equation 2.37 in the limit of negligible loss where the portion in parentheses is sometimes referred to as the effective length, L_{eff}, in lossy waveguides (not to be confused with an effective length presented in early bulk QPM literature in which the QPM grating quality was the parameter under review). Nevertheless, this adapted function still represents the L^2 dependence shown for plane-wave interactions when propagation loss is low. Calculating propagation loss and investigating a route to minimize this will clearly have a severe impact on the conversion efficiency, as can be seen in figure 3.6.

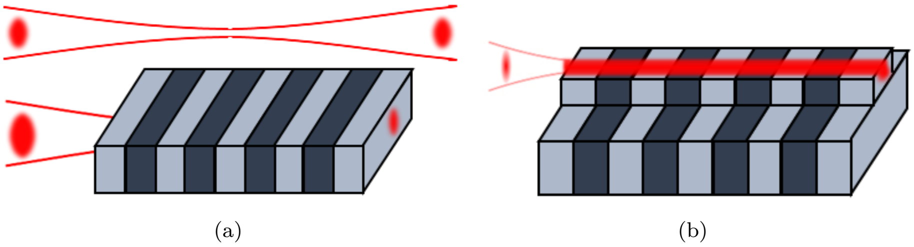
(a) (b)

FIGURE 3.5: Am illustration of laser coupling into PPLN for (a) bulk crystal and (b) a generic ridge waveguide. The clear advantage of waveguides can be seen from the beam confinement which leads to a larger overlap integral between the fundamental and SHG beam intensities.

In a waveguiding device, calculating the poling period for a particular SHG conversion wavelength would require knowledge of the effective index, n_{eff}, of the waveguide being used. In practice, this value is not known prior to fabrication of a waveguide in the early stages of research although large-mode waveguides permit this to be an adequate assumption as geometric dispersion is not dominant. An illustration to demonstrate the enhanced spatial overlap due to beam confinement in a waveguide is shown in figure 3.5. In waveguiding platforms in the literature, the conversion efficiency of a device is commonly presented as

$$\eta = \frac{P_3}{P_1^2 L^2} \times 100 \quad [\%\text{W}^{-1}\text{cm}^{-2}]. \tag{3.5}$$

The underlying reasoning for this normalisation to length is to account for the different length devices presented in literature. Hence, a conversion efficiency value like this should also accompany other characterising parameters, primarily the absolute output power P_3, as this allows a reader to conclude the power handling capabilities of the device.

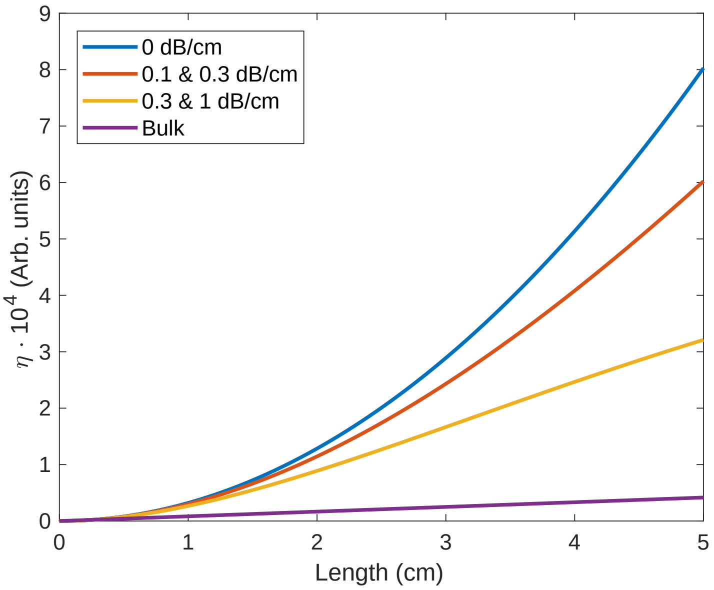

FIGURE 3.6: This graph illustrates the efficiency of waveguides with different propagation loss values in comparison to conversion in a bulk crystal as a function of crystal length. The advantage of nonlinear waveguides can clearly be seen. The curves representing waveguide data correspond to a variety of propagation loss values for the pump and signal beams for the case of SHG, respectively, as denoted in the legend. The figure is reproduced from example parameters given in Ref. [82].

3.4.1 Common methods for fabricating LN waveguides

One of the first methods of fabricating waveguides in LN was the proton exchange (PE) method in the early 1990's [83]. This process involves the use of a molten acid in contact with one surface of the LN crystal. Masking a LN chip with a metal layer prior to PE allows for the fabrication of channel waveguides. Hence, benzoic acid is a common choice [84, 85, 86] as it does not chemically etch metals. PE earns its name due to the out diffusion of the Li^+ ion and replacement with a H^+ ion i.e., a proton. With regards to nonlinear optical properties, PE is not considered a candidate for waveguide fabrication as it has been seen that the $\chi^{(2)}$ coefficient can essentially reduce to zero [85]. However, this was not always seen as an issue as PE LN could be investigated for applications as a modulator technology [87, 88].

It was discovered that if the PE LN waveguide was annealed, the nonlinear coefficient could be somewhat recovered as a stable, low-loss waveguide [89]. The annealed proton exchange (APE) technique essentially diffuses the proton-rich layer further into the substrate. However, this was still not an optimal solution as the fundamental and SHG modes typically had different, asymmetrical profiles which lead to a reduced overlap integral, figure 3.8. In an effort to tackle this asymmetry, lithium could be reintroduced to the upper surface of the LN waveguide, so-called reverse proton exchange (RPE). In a eutectic melt of LN, sodium nitrate and potassium nitrate, RPE is achieved and resulted in a normalised conversion efficiency of 150 %W cm^{-2} [90]. RPE and APE result in a positive refractive index change only for extraordinarily polarised light, making them inapplicable for use in Type-2 conversion processes, as defined in table 2.1.

The current state of the art for UV-generation in PPLN waveguides is the generation of 340 nm by Mizuuchi *et. al* [68] in ZnO:LN. These waveguides were formed by binding a PPLN wafer to another LN wafer with an adhesive resin. The PPLN layer was thinned to 3.1 µm and a ridge waveguide was precision machined into the surface. 22.4 mW of 340 nm was generated from an 81 mW input with a multi-longitudinal mode titanium-sapphire laser. While an efficiency of 340%/W provides a benchmark to achieve, the fabrication process utilised is complex, with very challenging tolerances to be met due to the grinding process for thinning. Altogether, this makes it non-ideal for commercialisation.

As previously indicated, the competitive technologies in integrated PPLN devices utilise either a channel, rib- or ridge-type waveguiding geometry. The subtle difference between these geometries is shown in a simplified illustration in figure 3.9. Pal *et al.* [92] carried out an investigation whether either channel or ridge geometries held an advantage over the other. It was determined that the ridge waveguides possess a higher threshold for photorefractive damage, previously described in section 3.2.1. The authors contribute this to a higher index contrast of the effective index of the guided modes in this geometry. A feature of the photorefractive effect is the blue-shifted detuning of the phasematching wavelength. The ridge platform is found to be two orders of magnitude more resistant, where the comparative parameter is the power of SHG light generated for an equal detuning response.

3.4.2 Incorporation of zinc into the LN crystal

After the success in optical characteristics from doping LN with Mg^{2+}, an interest developed regarding what other ions could be introduced into the LN melt during the crystal growth and extraction with a positive modification to its optical properties. Among these, Hf [93], In [94, 95], Sc [96] and Zr [97] were studied while being added to pure LN and typically had positive results in forming optical damage resistant materials.

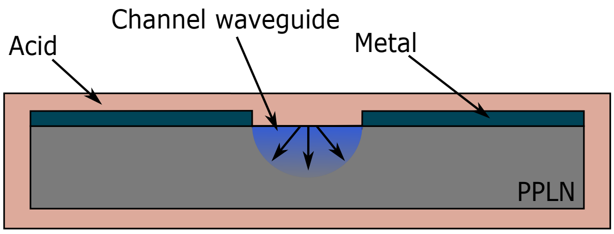

Figure 3.7: Simplified schematic of the fabrication process for proton exchange waveguides which were investigated as one of the first methods of waveguide development in PPLN.

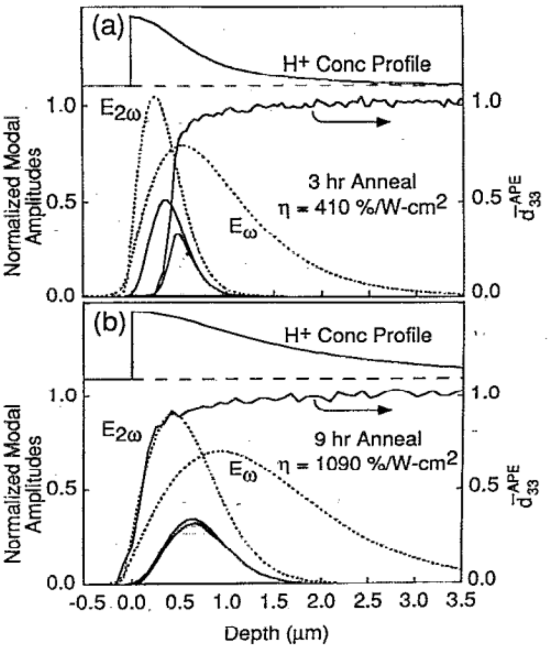

FIGURE 3.8: Highly dependent mode overlap integral with respect to the annealing parameters for a given waveguide in APE. Taken from Bortz *et. al*[91]

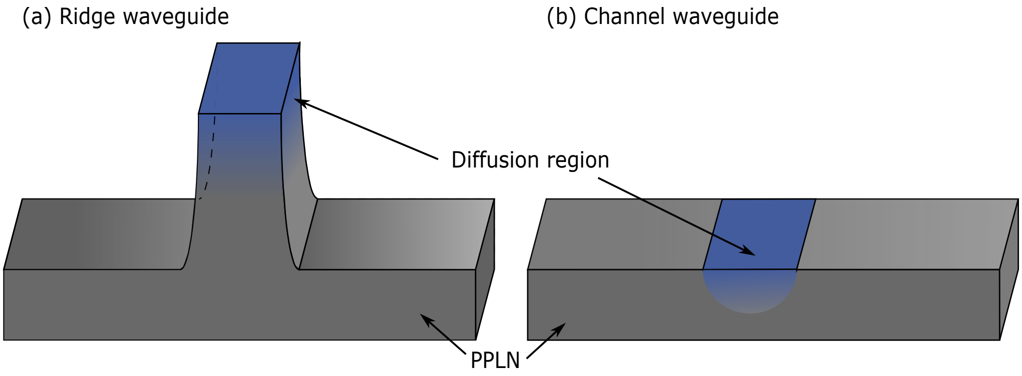

FIGURE 3.9: Simplified portrayal of the channel and ridge-type waveguiding geomtries used between the competitive research areas of which apply PPLN as a component.

However, a full review these dopants is outside of the scope of this thesis, of which we are only concerned with the diffusion of Zn into MgO:PPLN for the fabrication of a waveguide.

The first use of zinc-indiffused waveguides in LN was proposed and demonstrated by Young *et. al* [98]. Young *et. al*, from Stanford University, hypothesize that low valence ions reduce photorefractive damage and Zn^{+2} should fall into this category. While it may seem this was already an established theory, Young *et. al*'s work was carried out in the early 1990's, pre-dating the crystallographic studies which were completed in more detail in the following decade. It was also verified Zn diffusion gave a positive refractive index change for both extraordinarily and ordinarily polarised light. However, this line of research was not continued by the Stanford group. Since this work, a number of authors have had varying success with some form of zinc indiffusion [99, 100, 101, 102]. Ming *et al.*'s [99] work was carried out here in the Optoelectronics Research Centre at the University of Southampton, where the authors diffused metallic zinc into undoped PPLN to create channel waveguides. The authors report a high conversion efficiency at low power but these waveguides were found to be too difficult to fabricate long, uniform waveguides and the tolerances associated with designing a single-mode guiding condition at the pump wavelength were challenging. Adjacent projects to the research presented in this thesis were published by Carpenter *et al.*[103] and Berry *et al.*[10], of which 1560 nm-780 nm SHG was presented in the zinc-indiffused ridge waveguide platform was presented. These waveguides have been shown to display excellent uniformity for 40 mm-long waveguides, present an almost perfect phasematching spectra and have very high damage thresholds in comparison to other PPLN waveguide technologies [4].

Investigations by Zhang *et al.* [104] concluded that Zn replaces Nb ions which are sitting in Li sites and then proceed to replace Li ions. This work was carried out in pure LN which has been shown to be intrinsically laden with defects, and investigating how to dope the material to stabilise the crystal structure was the primary motivation but the Zn-doped material was found to have similar optical damage resistance to that observed for Mg doping. Volk *et al.* [105] observed a small shift in the absorption edge of LN with an increasing concentration of Zn. Approximately, the beginning of the absorption edge moved from ~370 nm to ~340 nm from pure LN to 7.2 mol.% of ZnO. While the authors were mainly investigating whether the introduction of Zn resulted in transmission anomalies for longer wavelengths, this was also a positive result and raises the optimism in developing a LN waveguide for UV generation with Zn as a dopant. No further research into this specific topic has been undertaken in the literature since the commercialisation of Mg-doped LN, although, Zn-doped LN substrates are available from NTT for academic or industrial projects as a competitive technology to MgO:PPLN.

3.5 Conclusion

The conclusions and QPM literature presented within this chapter and Chapter 2 leads us to the development of ridge waveguides formed using zinc indiffusion to create a refractive index contrast to bulk LN. These combined factors have the potential to result in higher damage threshold PPLN waveguides. Given this, the following chapters will present current research on the development of PPLN ridge waveguides. The focus of the presented experimental work will be the generation of blue/UV light and fabrication of a device which has the potential to be scalable towards a manufacturable process.

Chapter 4

PPLN Waveguides for Short Wavelength Generation

4.1 Introduction

The creation of efficient and small-footprint UV light sources for ion trapping is a topic of recent interest driven by a desire to create portable quantum systems for timing and navigation. Routes towards achieving low-footprint 369.5 nm sources are of particular interest for the Doppler cooling of Yb^+ ions [106]. It is preferable to use frequency doubling in the process of generating this specific wavelength as near-IR lasers are commercially available and may be frequency locked to molecular iodine at 739 nm [107]. It has been suggested in recent work by Mulholland *et al.* [108], during the development of a complete device for all Yb^+ ion trapping sources, that a 100 µW CW laser is the minimum requirement for this cooling application.

Although there have been examples in the literature which have demonstrated the wavelengths required (and even shorter) using lithium niobate (LN) waveguides [109, 68, 110], there is still not a commercially available device to supply quantum technology research or industrial efforts. The technology and fabrication processes in this project will aim to provide a route for scalable manufacturing of UV wavelengths to supply this rising demand. Using the technology being developed here in the University of Southampton, zinc-indiffused lithium niobate ridge waveguides were investigated as a route for efficient UV generation. The work in this chapter will present the design, fabrication and testing of these ridge waveguides for SHG of 390 nm light. This particular wavelength is chosen due to the commercial availability of 780 nm lasers and optical components. Lasers operating at this specific wavelength have developed as a mature technology due this being the probe wavelength for CD-ROM drives. Additionally, the transition frequency of rubidium occurring at 780 nm [111, 112] requires versatile sources which could be locked to the specific absorption frequency. Hence, there was a technological surge in external cavity diode lasers (ECDL) in the 1990's [113] which are wavelength tuneable due to their diffraction gratings, permitting a modification to the feedback wavelength into the cavity. However, they are typically limited with regards to maximum output power; limiting our ability to investigate the efficiency of the conversion process, with respect to the input power, for the PPLN ridge waveguides.

To investigate a total system capable of reducing the size, weight and power (SWAP) of a blue/UV source, the results from a collaboration with the Department of Physics & Astronomy in Southampton and Tampere University will be detailed in section 4.5 and further details are found in Ref. [114]. This work will provide the intermediate step to future research in driving the operational wavelength further into the UV for application with ion trapping systems. Note that Chapter 5 is a follow on study that investigates the effect of waveguide-width non-uniformity in the fabrication of these devices and hence, discussion regarding the shape of certain nonlinear phasematching spectra shall be deferred until then.

4.2 Fabrication of zinc-indiffused MgO:PPLN waveguides

The PPLN waveguides presented in this thesis are an extension of a plethora or projects which involved collaborations between the University of Southampton and Covesion Ltd. in the development of efficient 1560-780 nm conversion systems. The general fabrication flow is schematically presented in figure 4.1. The reasons for using zinc as the dopant for providing a positive index contrast in LN was described in section 3.4.2. The periodic poling was carried out by Dr. Corin Gawith using the poling routine which is the intellectual property of Covesion Ltd. The deposition, diffusion and dicing of the waveguides will be described in the following sections.

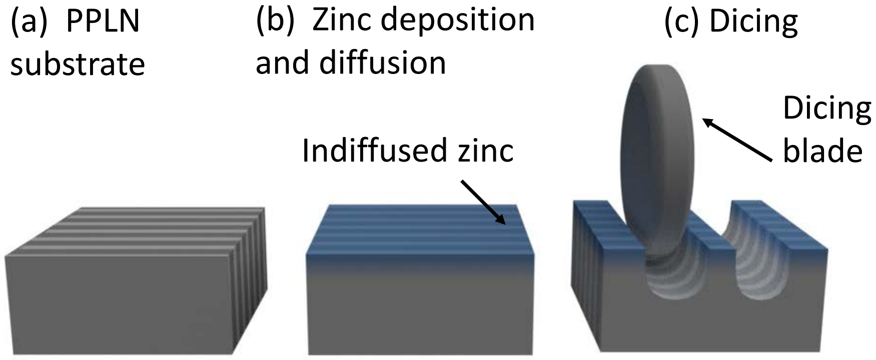

Figure 4.1: Fabrication process flow of the zinc-indiffused PPLN waveguides presented in this thesis.

4.2.1 Zinc sputtering: deposition and diffusion

Sputtering is a deposition method which is capable of depositing both metallic and dielectric films. Sputtering falls into the deposition category of physical vapour deposition, requiring a high potential difference between a target (cathode) and the substrate (anode). In distinct contrast to evaporation technologies, sputtering chambers contain a gas, argon, to strike a plasma and bombard the target to release ions. Under the influence of the potential gradient, these ions are then directed towards the platform on which the substrate sits.

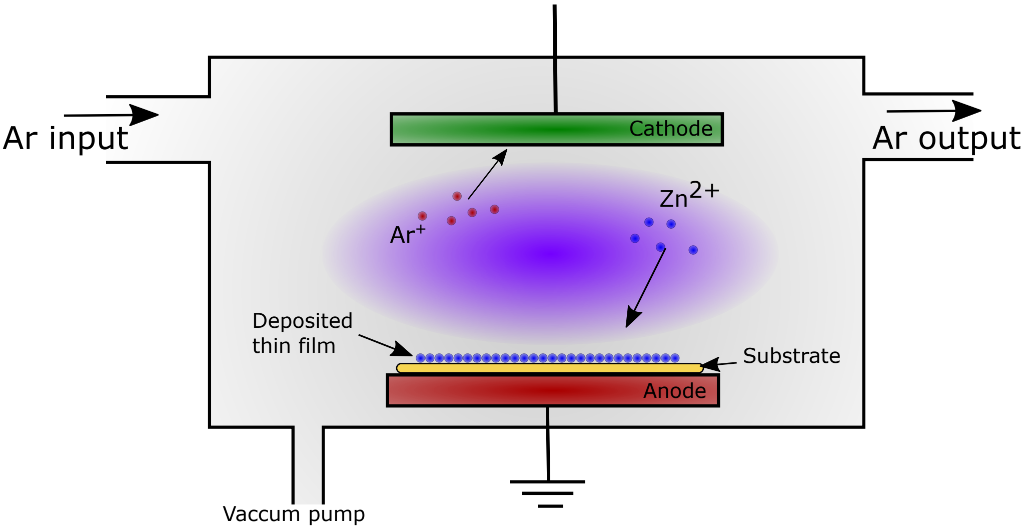

FIGURE 4.2: Basic principle of sputtering deposition.

RF magnetron sputtering is a variance in which the electric field is oscillated to avoid charge build-up on the target. It also allows for oxides to be used as the target if depositing a particular oxide is needed. This is advantageous as sputtering processes can arc due to a high density of localised charge. The primary application of RF magnetron sputtering is deposition of tantalum oxide and aluminium oxides. In general, the low cost of sputtering makes it an attractive deposition choice.

Indiffusion of the zinc layer is performed in a furnace in an oxygen environment. The presence of oxygen promotes the growth of ZnO for any remaining metallic zinc. This dielectric layer will benefit the propagating mode's properties in comparison to a metallic layer which would greatly enhance the propagation loss, due to its non-negligible extinction coefficient. This route of fabrication is in contrast to this research group's prior work in which a ZnO layer was directly deposited using atomic layer deposition (ALD) [103]. This fabrication route was discontinued as ALD is inherently slow and expensive to undertake.

4.2.2 Dicing

The description of the ultra-precision dicing processes used to fabricate our PPLN waveguide devices shall be limited as this research area is primarily the work of Dr. Lewis Carpenter, who gained expertise and developed the optical dicing processes in his own PhD work [115]. However, a brief explanation of the process is required for completeness and an understanding of why this is discussed and commented on in Chapter 5. The PPLN waveguide fabrication described in this work (ridge formation, facet preparation and singulation) uses a Disco DAD3430 machine, figure 4.3.

Figure 4.3: Photograph of the dicing machine used for the fabrication of the zinc-indiffused PPLN ridge waveguides presented in this thesis. Photo courtesy of Dr. Lewis Carpenter.

While dicing processes are more commonly applied to singulation of die as one of the final steps in large-scale semiconductor chip manufacturing, the technique applied here has been finessed for application to optical quality facets and waveguide side-wall definition. This is possible due to prior projects exploring the application of dicing in the so-called ductile dicing regime in which material can be removed from a sample and/or substrate without chipping. For brittle materials, such as silica or lithium niobate, a typical stress-strain curve is observed with a sudden curve prior to cracking [116], as seen in figure 4.4(a). By careful investigation of machining parameters such as rotational speed, depth of cut and translational speed, ductile removal of material can be obtained, thus allowing for un-scattered optical transmission. Applying shear stress beyond the plastic limit will permit the propagation of cracks and formation of a pitted surface [117]. A clear demonstration of this and an example parameter set can be found for silica in Carpenter *et al.* [118]. Additionally, dicing of lithium niobate has been shown to achieve roughness values of 0.29 nm [119], representing the mean height from lowest surface value, typically denoted as S_a; sub-nm roughness is the benchmark for lapping a polishing facet preparation [120] although a variety of different roughness parameters are used to demonstrate this. Figures 4.4(b) and 4.4(c) show example images of successful ductile dicing and early stage research before the machining parameter set is well defined, respectively.

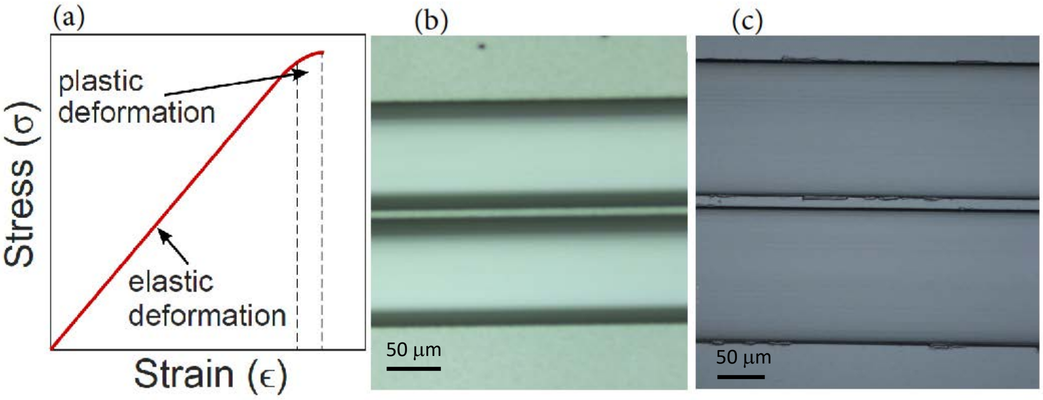

Figure 4.4: (a) Typical stress-strain graph for a brittle material such as silica or LN. The dashed lines indicate the region of plastic deformation for ductile removal of material. Optical microscope images of lithium niobate ridge waveguides with (b) smooth side-walls from the ductile dicing process and (c) a chipped waveguide in the early stages of waveguide development. The centre, horizontal line is the protruding waveguide in both images.

Experience with optical dicing processes and the versatility of applications has been a key part in the publication output of our research group for 10 years, primarily for silica-based optical waveguide technologies and lithium niobate waveguides. Although this is not a complete list, and excluding PPLN research which will be more thoroughly discussed, optical quality dicing has lead to a demonstration of miniaturised external cavity diode lasers [19], micro-cantilever arrays for force sensing in a planar platform [121], cantilever and cavity fabrication in an integrated optical fibre [122] and allowed for convenient facet preparation in a cohort of other projects [123, 124].

4.3 Fabrication characterisation: methodology and results

As a practical and simple route to optimising the waveguide mode to be used for the 780-390 nm SHG in the Zn-indiffused PPLN ridge waveguides presented in this chapter, I quantified this measurement by evaluating the mode field diameter of the waveguides; this is very similar to the adjacent project for 1560-780 nm SHG waveguides. As laid out in the immediately prior sections, the route for optimisation is to first choose a planar diffusion parameter set (of the zinc layer) to proceed with, followed by an investigation of ridge widths formed via the dicing process. The mode field diameters measured in this work make use of an optical characterisation setup developed by Dr. Rex Bannerman [125].

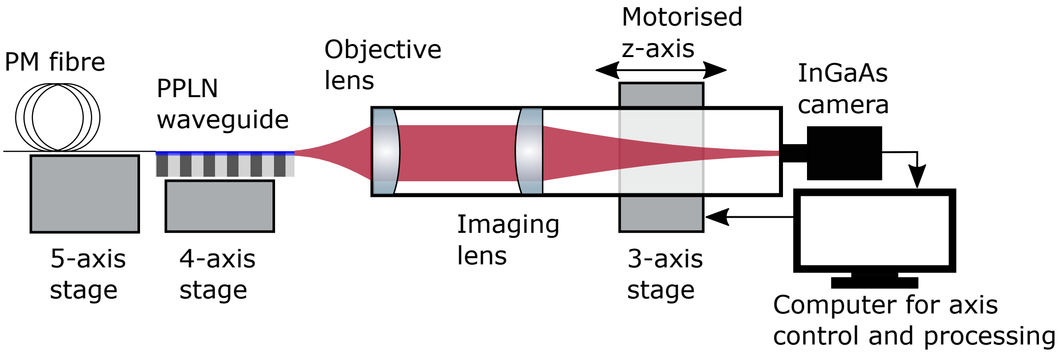

Figure 4.5: Schematic diagram of the optical system used for measuring mode profiles of the zinc-indiffused PPLN waveguides presented in this work.

The optical characterisation system uses a high resolution InGaAs CCD camera (Raptor, Owl 640) with calibrated z-translation steps to measure the diverging beam on the output facet of an integrated waveguide. This system is schematically presented in figure 4.5. This enables the analysis of the numerical aperture (NA) of a waveguide but in this work, it is simply used as a route to determining the MFD. While the InGaAs detector is most sensitive to 1550 nm sources, its broad absorption band, typically 400-1700 nm allows its application for the wavelengths used here also. The intensity profile of the beam is recorded for a series of camera distances from the waveguide facet. These profiles are then fitted via the so-called second-moment analysis [126] to evaluate the MFD. For this work, I selected the smallest MFD to represent the waveguide, after examining the quality of the NA fit to ensure the fitting algorithm ran correctly.

Figure 4.7 displays the vertical MFDs of a range of LN substrates with a Zn indiffused layer. The thickness represents a nominal, design thickness prior to diffusion. The temperature recorded is the peak indiffusion temperature which was held for 1 hour before ramp down. Samples were present in the chamber for the ramp up and ramp down stages to prevent thermal shock and damage to a substrate. A Zn thickness of 150 nm and a diffusion temperature of 900°C were chosen as the fabrications parameters due to the minimal MFD obtained with these values.

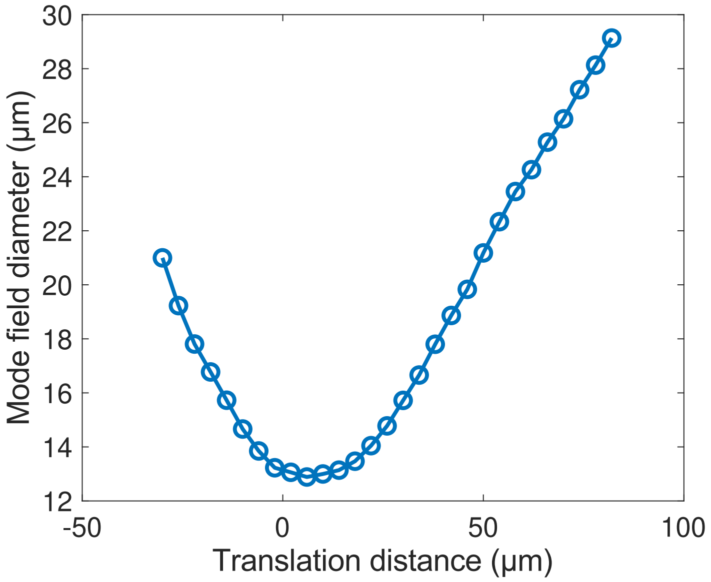

Figure 4.6: Example of data measurement set for mode profiling of the zinc-indiffused PPLN waveguides.

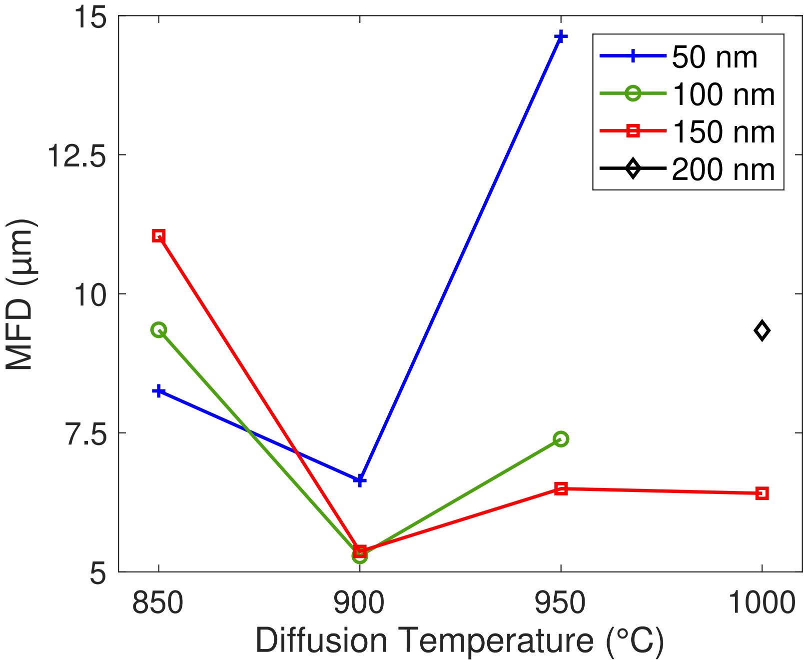

Figure 4.7: MFD values for a range of different deposition and diffusion parameters. The goal was to find a minimum value to maximise potential for overlap between modes and for single-mode operation.

The grating period, Λ, for 780-390 nm SHG in bulk MgO:PPLN is 2.44 µm, as calculated from equation 2.16. Previous experimental research carried out in this group determined SHG of 1560 nm light phasematched in a similar waveguide with a poling period of 18.5 µm. This is in comparison to the 19.2 µm grating calculated for a bulk PPLN crystal at 114 °C [4]. A straightforward ratiometric offset calculates the grating period

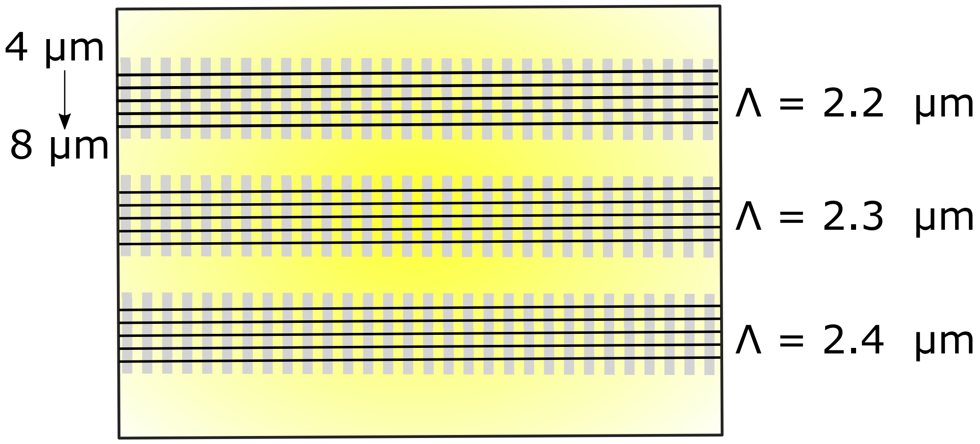

FIGURE 4.8: Simplified blueprint design of the 780 nm doubling PPLN. The ridge widths displayed on the left are present in each of the three grating periods and are nominal design values. Black horizontal lines represent the location of ridge waveguides and the grey vertical lines with a 50/50 duty cycle illustrate the direction and orientation of the periodic domain reversal.

for 780-390 nm SHG to be 2.35 μm. However, the Sellmeier coefficients are not well defined below 400 nm; the shortest wavelength Gayer *et al.* [46] calculates refractive indices for is 500 nm. Hence, 2.2-2.4 μm was chosen as the range for experimentally investigating and was imprinted in a standard z-cut, 0.5 mm-thick MgO:LN wafer. Each Λ contains 5 × 200 μm with a small gap between each set to minimize local merging.

Almost all of the work and results presented in this chapter originate from one of two samples that were designed as per figure 4.8 and named in table 4.1. They were selected and ridges diced for regions of which the poling looked to be of good quality. This is due to the huge technical challenge associated with domain reversal of a 2.2 μm-period in bulk PPLN. I will explicitly state which chip was used for each data set presented but, typically, C121A was used for nonlinear optical generation only, including the higher power conversion presented in section 4.5. C121B was used for phasematching and modal characterisation and (after being determined to be less efficient than C121A), it was used for the SEM imaging presented in figure 4.9.

Although it will be explicitly discussed later, no SHG was observed in the PPLN ridge waveguides with 2.3 or 2.4 μm gratings using our current laser sources. Hence, all SHG characterisation presented in this thesis is a result of the nominally 2.2 μm period grating. There is no underlying physical reason that the longer period gratings did not phasematch except that the available laser was wavelength limited to below ~790 nm; a 0.1 μm grating period increase corresponds to a 8 nm increase for the wavelength required for phasematching in the 780 nm spectral region in a bulk MgO:PPLN crystal. Therefore, it is expected the 2.3 and 2.4 μm gratings will potentially phasematch at 789 nm and 798 nm, respectively, with an appropriate pump laser.

Table 4.1: Naming of the 780 nm frequency doubling Zn-indiffused PPLN chips which contain waveguides and are commonly referred to in this thesis.

Waveguide length	Waveguide given name
14 mm	C121A
11 mm	C121B

SEM micrographs of the fabricated ridge waveguides can be seen in figure 4.9. Sample, C121B, was gold coated with approximately 10 nm of gold prior to the imaging. Figures 4.9(a) and 4.9(b) were taken in secondary electron mode and backscatter mode, respectively. The choice of imaging mechanism was mostly defined by the quality of image obtained by minimising edge effects and selecting a suitable depth of focus; I was not necessarily searching for an elemental profile. However, it is interesting to note the diffusion region in the uppermost section of the ridge waveguide was not apparent even via the backscatter detector which is preferential in differentiating between elements or concentration of elements [127].

Following the optimisation of the planar waveguiding layer, presented in figure 4.7, waveguides were diced to nominal widths ranging from 4-8 µm for a further investigation into this fabrication parameter. Single-mode guiding in the horizontal axis is a preferable condition but ultimately, maximising the potential for the overlap integral of the pump and SHG modes, equation 2.36, is the parameter which we have the most control over. The mode outputs are presented in figure 4.11 for each respective waveguide at the pump wavelength.

This is a vital step in our development and understanding of these waveguides not only for the overlap of the modes but also the effective index of the modes which are generated. Recalling SHG phasematching equation 2.15, k-vector phasematching is performed for waveguides as the propagation constant, typically denoted by β. The devices tested and used in this research were laid out as shown in figure 4.8. The values for ridge width noted, 4-8 µm are nominal from the design and not measured. While it is challenging to have confidence in the waveguides width from optical microscopy, measured values and how this was estimated will be discussed when the value is presented for the respective waveguide.

Figure 4.10 displays the horizontal and vertical (x and y) MFDs for each of the waveguides. A superluminescent diode (SLED) with a peak wavelength at approximately 780 nm was used for the characterisation of the pump mode. This source has been magnification calibrated. As expected, the difference of y-axis MFDs is minimal over the range of waveguide widths available; ranging from 5 µm to 6 µm. The x-axis MFD for the pump mode is seen to have a slight minimum for the nominally 5 µm-wide waveguide. Hence, one would expect this to have highest conversion efficiency as having the largest potential for a high intensity beam. The depth of the waveguide with respect

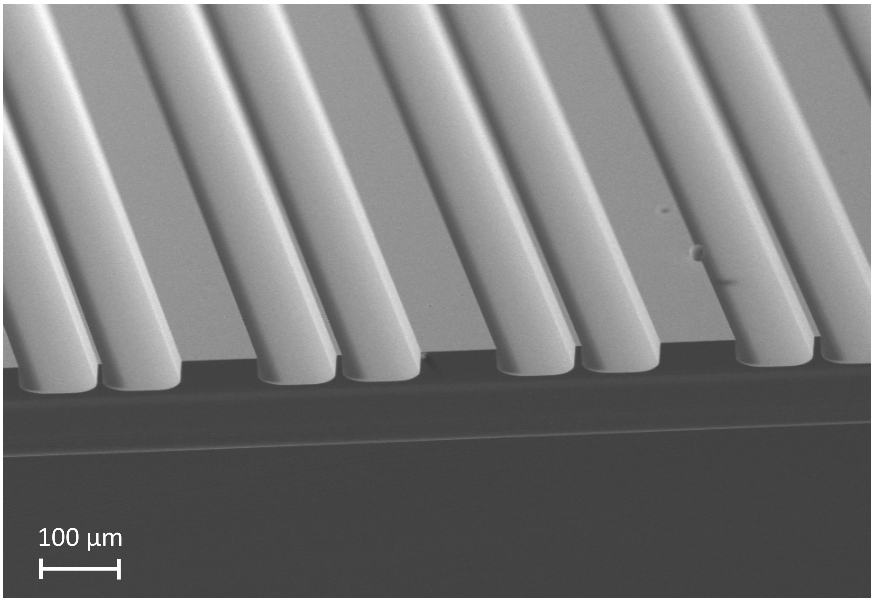

(a)

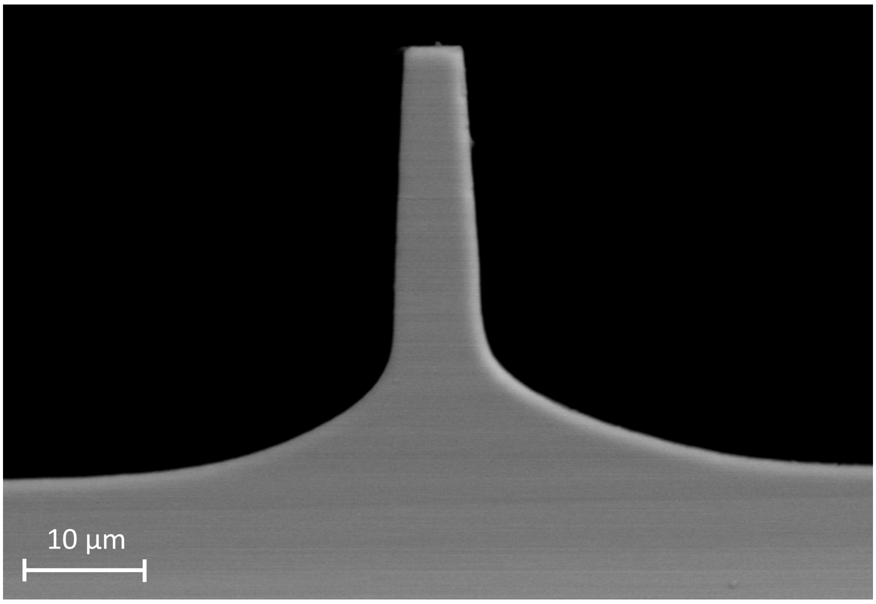

(b)

FIGURE 4.9: SEM images of fabricated waveguides in chip C121B. ; (a) Multiple waveguides presented to display the layout of the waveguide definition layout. Note, the vague white line below the waveguides which shows the depth of the facet preparation cut. (b) Backscatter SEM image of the narrowest ridge waveguide on this chip and a clear display of the.

to the upper diffused area is chosen due to prior research in which this depth provided the optimal side-wall roughness and also verticality; this is the reason why the aspect ratio of the waveguides characterised and displayed in figure 4.9(b) may seem a little excessive. Additionally, the planar waveguide region observed between each waveguide, as seen in figure 4.9(a) exists to limit potential damage between ridges.

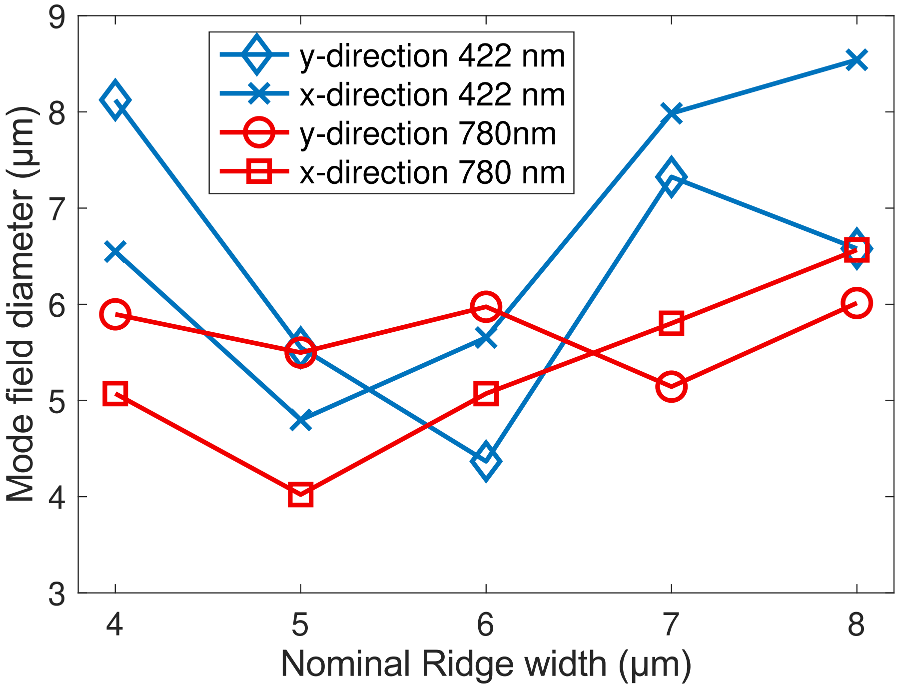

FIGURE 4.10: Waveguide mode field diameters for each waveguide of the chip C121B. Data points are connected only to assist the eye in deciphering which points are related. The data representing waveguide characterisation using the 422 nm source should be considered qualitative and is thoroughly discussed in the main text.

While the 422 nm characterisation is presented, it does not assist in the development of these waveguides. This is due to a plethora of reasons: (a) the wavelength available for mode profiling does not match the generated SHG wavelength from these waveguides, (b) our current mode profiling configuration is not calibrated for blue light as this was the only project requiring its usage, (c) the source is a laser (Toptica Photonics, LD-0405-0030-4) and hence the image is prone to superimposed interference fringes, which increases the error in measurement and finally (d) the launched mode was the fundamental mode but the blue/UV mode generated in experimentation, section 4.4, was a first-order mode. Hence, we should look at the blue MFD as qualitative only for future projects which may exploit SHG of the fundamental-to-fundamental interaction for these wavelengths. Viewing this as qualitative, it also appears the nominally 5 μm-wide waveguide is an ideal candidate due to its minimal MFD. As will be discussed in the following sections, the narrowest waveguide was observed to be the most efficient. The nominally 5 μm-wide waveguide, which may have had the highest efficiency potential, demonstrated an interesting phasematching profile which then led to the work presented in Chapter 5. The conversion efficiency of these waveguides will be investigated in 2 regimes: a low power, tunable ECDL to determine phasematching conditions and a higher power VECSEL source. Both will be discussed in the following sections.

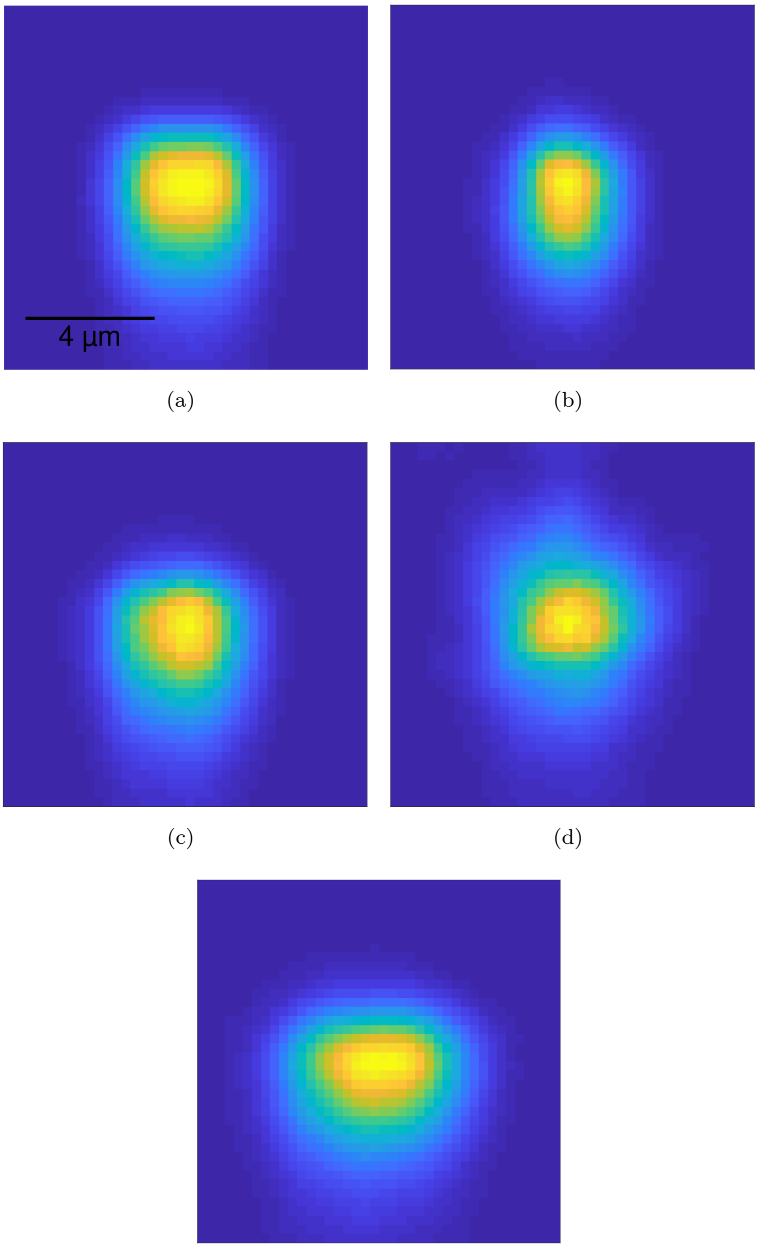

(a) (b) (c) (d) (e)

FIGURE 4.11: Waveguide mode profiles of sample C121A using a broadband SLED source centred around 780 nm. These correspond to the waveguides of nominal ridge width (a) 4 µm, (b) 5 µm, (c) 6 µm, (d) 7 µm and (e) 8 µm. Scale bar presented in (a) is representative of all mode profiles presented here.

4.4 Low power, nonlinear optical characterization

An optical test setup was designed and built for nonlinear characterisation of these new waveguides designed for SHG of 780 nm light using a tuneable external cavity diode laser (ECDL) and lock-in detection to enable measurement of low optical powers. The fine positional adjustments to enable the launch and collection optics were mounted on a Newport Corp. 5-axis stage (M-562F-TILT-LH and M-562F-TILT-LH) and a 3-axis stage (M-562F-XYZ), respectively. The input beam was shaped via a fibre zoom collimator (Thorlabs, ZC618APC-B) and a B-coated aspheric lens (AL) for final focusing into the waveguide. The schematic for this preliminary interrogation of these waveguides is displayed in figure 4.12 and a photograph of sample C121A and the surrounding optics is shown in figure 4.13.

The 780 nm tuneable laser used in this work is a motorised ECDL (Sacher Lasertechnik Littman/Metcalf Lion series) and supplies approximately 9-10 mW to the APC fibre input after free-space fibre coupling. This is dependent on the power output from the laser which is a function of its wavelength. This can be monitored throughout a wavelength scan via a dichroic mirror, if the experiment requires it. Such an optical power measurement setup is presented in figure 4.21 for a different pump source. In this section, characterisation of the waveguides and phasematching conditions are the primary objective and the setup is displayed in figure 4.12. The lock-in amplifier used was a

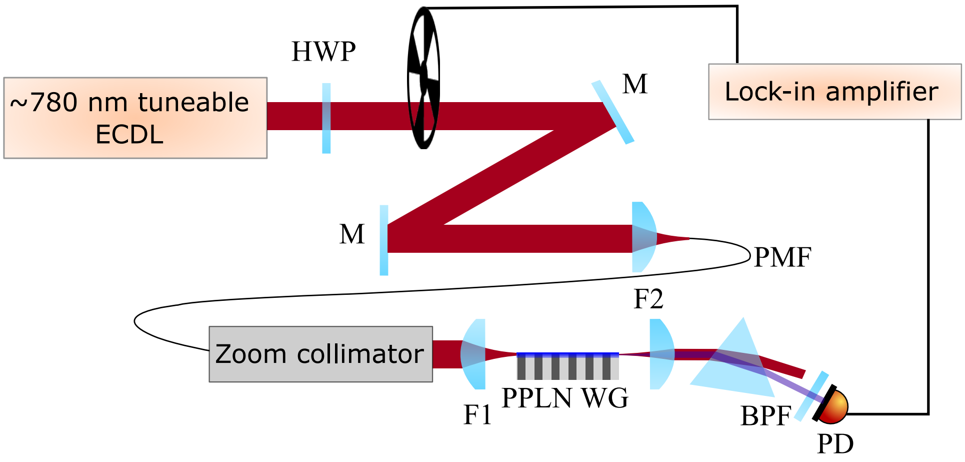

FIGURE 4.12: Schematic of the optical characterisation setup for measuring SHG of 780 nm in our zinc-indiffused PPLN waveguides with low-pump powers from a commercial, tuneable ECDL. Note the prism separation of the pump beam and the generated SHG to enable isolation of the low 390 nm signal.

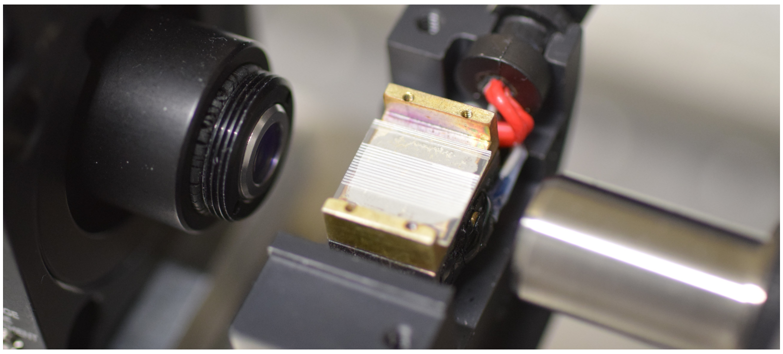

FIGURE 4.13: Photograph of the PPLN sample C121A alongside the launch and collection optics.

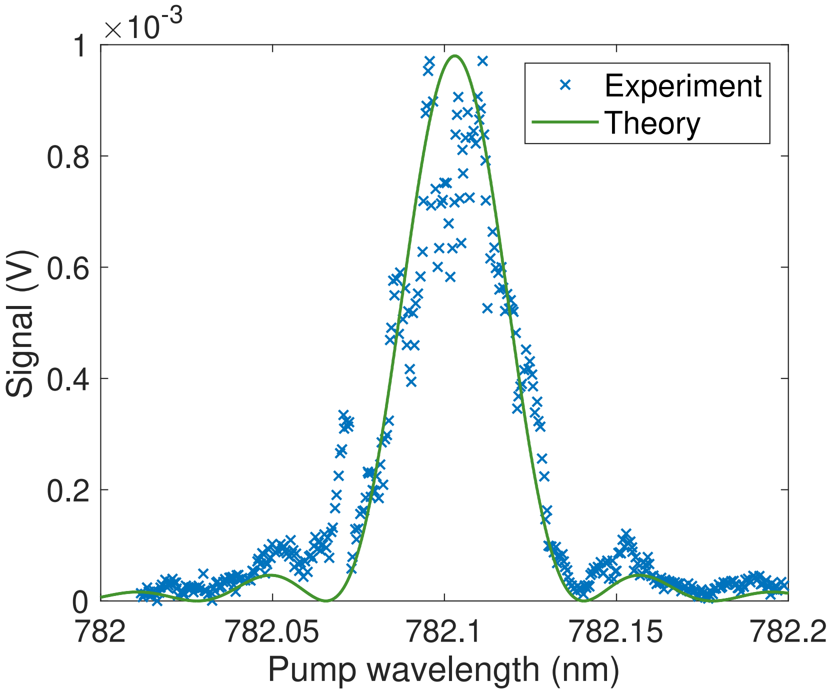

FIGURE 4.14: Phasematching spectrum of the most efficient waveguide, measured in sample C121A-4 µm. The solid line represents a theoretical sinc^2 for a device 14 mm in length (the length of the waveguide) using bulk MgO:PPLN parameters. This waveguide is nominally 4 µm-wide with a 2.2 µm poling period, diffused at 900°C for 1 hour and characterised at room temperature.

Stanford Research Systems product, SRS830. The detector used was a balanced silicon photodiode (Thorlabs, PDB210A). Only one photodiode was utilised and the other was covered as the balanced functionality was not required. Lock-in detection enables a clear, non-quantisation limited phasematching spectrum to be recorded, which was advantageous for the numerical modelling comparison, presented and discussed in Chapter 5.

Through initial power-recording characterisation, it was apparent the narrowest (nominally 4 µm-wide) waveguide was the most efficient. The phasematching spectrum for this waveguide, as a function of pump wavelength from the ECDL, is presented in figure 4.14. A theoretical sinc^2 using bulk MgO:PPLN parameters for a 14 mm-long waveguide is presented alongside this data, scaled to the value of maximum voltage acquired from the spectrum. A comparison for the width of a spectra provides some qualitative information regarding the quality of grating and waveguide fabrication. The phasematching spectra associated to waveguides 5-7 µm-wide and the wavelength associated to maximum SHG efficiency for each waveguide in samples C121A and C121B are presented in figures 4.16 and 4.17 respectively. Calculating the spectra which would result from any arbitrary grating structure or one suffering from a particular fabrication feature, such as chirp or missing domains, would require an in-depth theoretical study as discussed in early work by Fejer *et al.* [128]. Accurate knowledge of the location of every domain

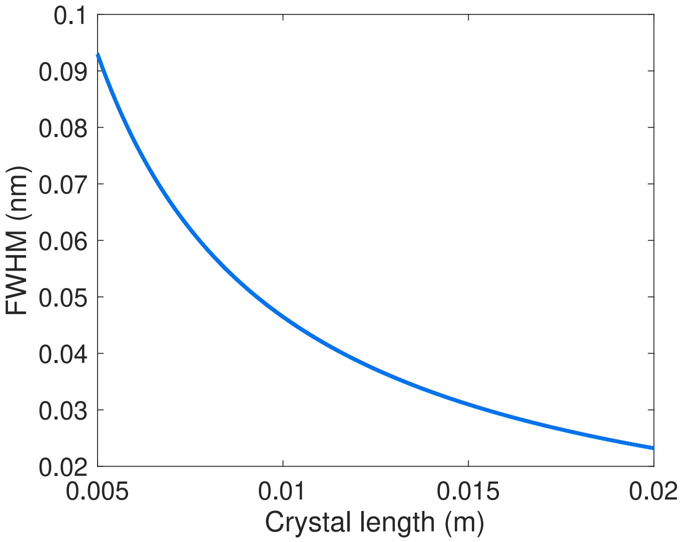

Figure 4.15: Theoretical full width half maximum of PPLN phasematching spectra for the pump wavelength as a function of crystal length assuming an ideal structure.

location, width and orientation is also required. This is not the work undertaken here but rather a simple visual comparison. Additionally, Fabry-Perot fringes are observed, figures 4.14 and 4.16, because the waveguide is not anti-reflective coated or angle cut. However, this qualitative comparison should be used with caution as a 10% increase in FWHM, which may be barely noticeable with experimental noise, would be an effective length reduction of 1 mm for a 14 mm device for SHG of 780 nm light.

Nevertheless, features of the comparison to the bulk sinc^2 provide some further insight to the quality of the waveguide; the symmetrical data indicates our fabrication process is capable of creating uniform waveguides at the narrower dimensions (in comparison to adjacent projects [4, 10]). Longer waveguides, having a much narrower phasematching bandwidth, will be far more sensitive to any broadening effects. In future work and utilising long devices, the comparison of FWHM to its theoretical value will provide far greater insight into the quality of the PPLN ridge waveguide fabrication. This relation between FWHM and crystal length is shown in figure 4.15, for reference.

4.4.1 Numerical modal estimation of the waveguides to extract physical parameters

Recalling equation 3.4, the nonlinear overlap integral is required to parameterise these waveguides and allow for numerical fitting to quantify and remaining parameters which are not experimentally measured. To calculate the nonlinear overlap integral, I use a simple numerical model which has been constructed in FIMMWAVE. Since the fundamental MFDs in both axes are known, the model is adapted for waveguide width and diffusion depth until it closely matches the measured MFDs for the fundamental 780 nm

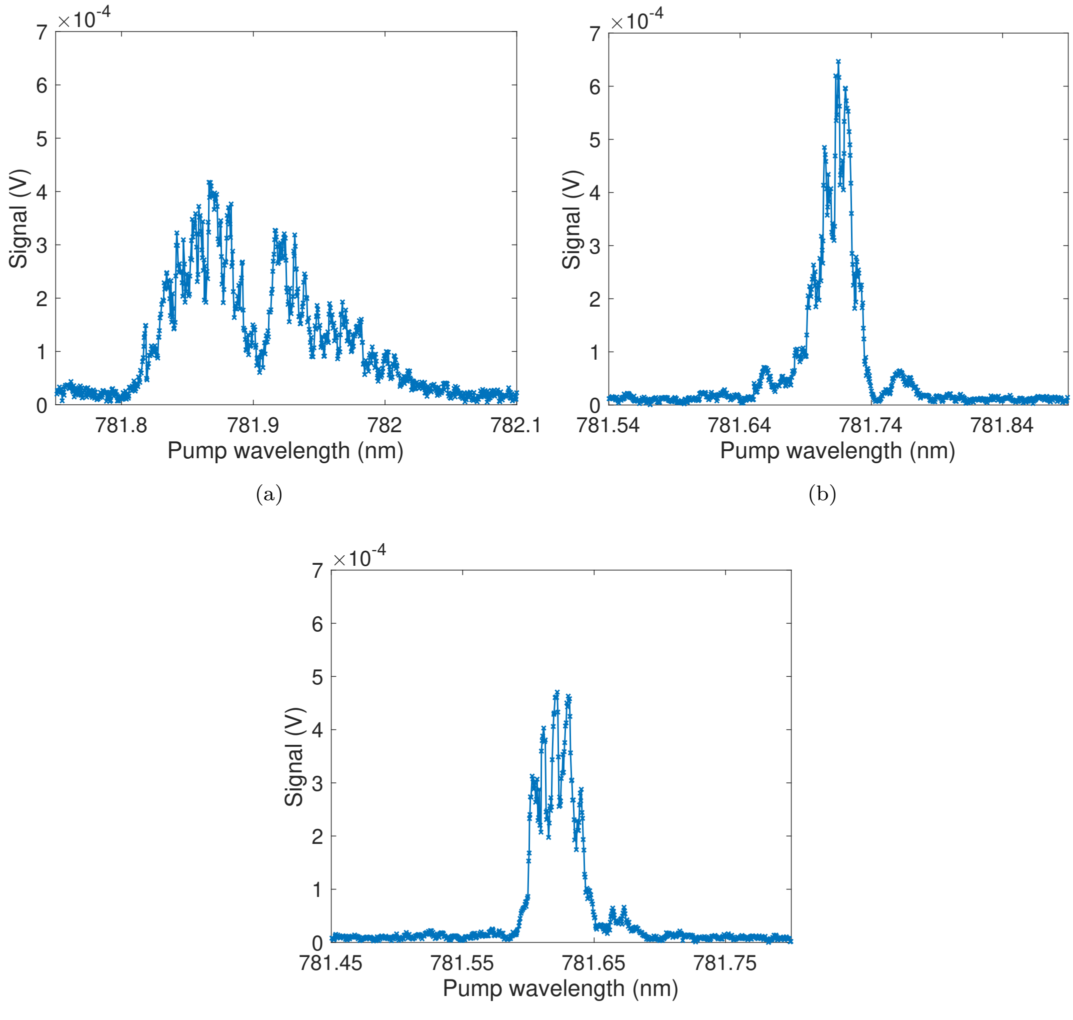

(a)

(b)

(c)

FIGURE 4.16: Phasematching spectra of zinc-indiffused ridge waveguides in chip C121A for their nominal widths: (a) 5 µm (b) 6 µm (c) 7 µm. Data presented as voltage as it was taken via lock-in amplification for detailed spectra of low signals.

propagating mode. The maximum refractive index differential is maintained as 0.03, as per Young *et al.*[98], with the base LN refractive index of $n_{780} = 2.17$. The diffusion profile used to estimate our waveguides in this early work is one side of a Gaussian profile with an associated standard deviation, $\sigma = 7$ µm. This mode is shown as the red contour plot in figures 4.18(a) and 4.18(b).

Given the defined waveguide dimensions, the modal solutions of the 390 nm mode are readily investigated; the base refractive index of the LN is modified to that resulting from the corresponding Sellmeier equations, equation 2.17, giving $n_{390} = 2.33$. The contour plot of where the fundamental and first order solution modes are positioned in the waveguide are visually presented in figures 4.18(a) and 4.18(b) as the blue lines. The associated electric field amplitude distribution is displayed in figures figures 4.18(c) and 4.18(d). The negative amplitude associated to the first order mode makes this nonlinear

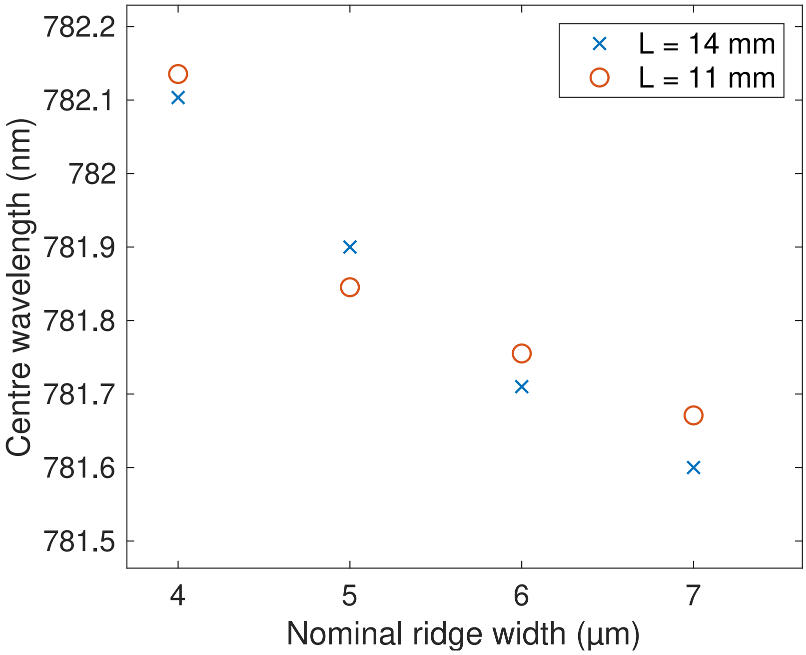

FIGURE 4.17: Centre wavelength of each of the waveguides tested in the two-most used chips investigated in this work.

conversion process obviously less than ideal by reducing the associated integral. The overlap integral, $\mathfrak{I}_{ov}$, for these numerical modes are evaluated to be 1.91×10^5 m^{-1} and 9.475×10^4 m^{-1} for the fundamental to fundamental and fundamental to first-order interactions, respectively. Surprisingly, the reduction of $\mathfrak{I}_{ov}$ by approximately a factor of 2 is not as low one might expect as it appears the overlap is dominated by the lower modal lobe. Nevertheless, this would play a substantial difference in conversion efficiency due to the squared-dependence of SHG power on this term.

Assuming a perfect end-facet for coupling light, the theoretical coupling efficiency, η, is dependent on the profile of the electric fields for the launched, A, and waveguide ,B, modes. This is given as

$$\eta = \frac{|\iint_{-\infty}^{\infty} A(x,y)B(x,y)dxdy|^2}{\iint_{-\infty}^{\infty}|A(x,y)|^2dxdy \iint_{-\infty}^{\infty}|B(x,y)|^2dxdy} \tag{4.1}$$

assuming no phase changes across the face of the mode. This relationship of modes to coupling efficiency is a major reason for the 1560-780 nm PPLN waveguides presented in Refs. [10, 103] having a similar mode profile to standard telecoms optical fibre, SMF-28. Future projects and commercial prospects rely on efficiently fibre-coupling these waveguides for field deployment and long-term stability in the launch alignment.

Due to the adaptability of the alignment optics and using an optimal launch mode obtained from the single-mode optical fibre, I assume the launch has the ability to reach a theoretical maximum, i.e., the beam diameter and position relative to the waveguide

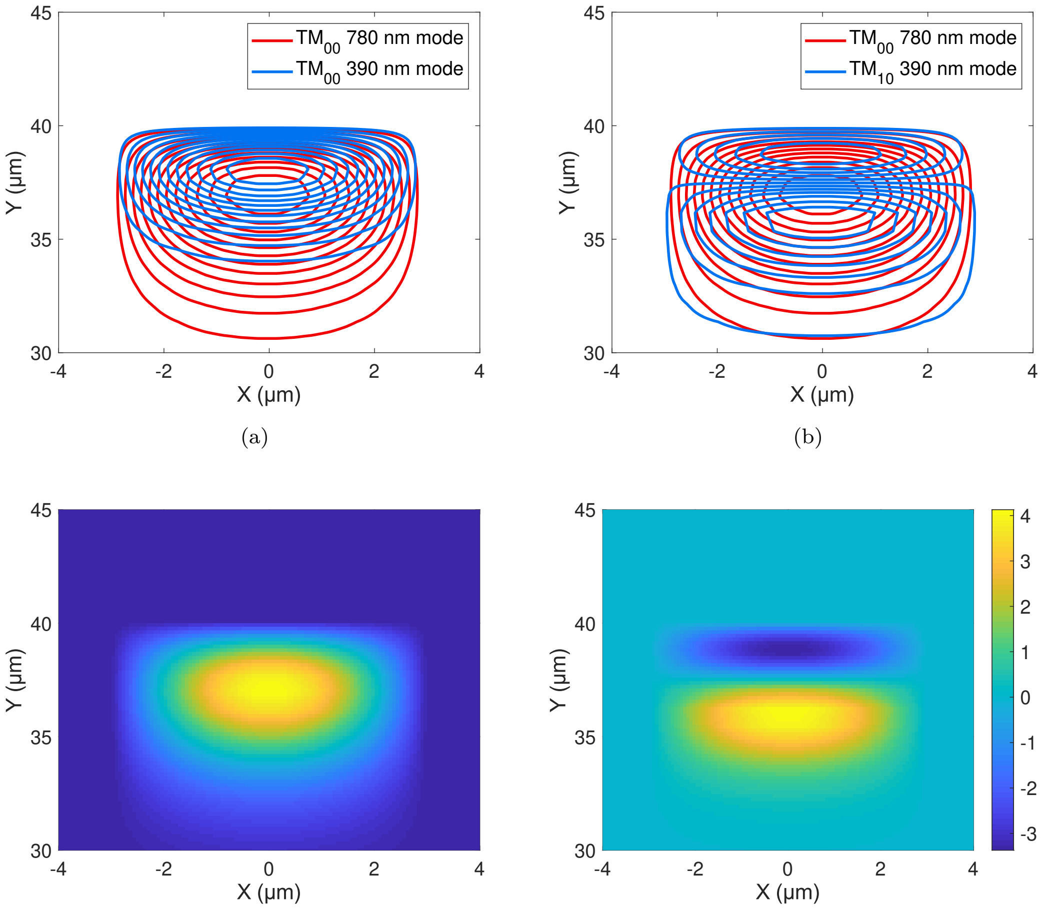

(a) (b)

(c) (d)

Figure 4.18: Numerical analysis of the mode profiles for the zinc-indiffused PPLN waveguide used in this work. Theoretical modal placement of the fundamental pump with the (a) fundamental SHG mode and (b) the first-order SHG mode. Vertical electric field distribution of the (c) fundamental SHG mode and (d) the first order SHG mode for use in calculating the overlap integral between these modes and the pump mode.

mode can be controlled. The intensity profile of this theoretical, launched Gaussian beam [129] is

$$I(x,y) = A\exp(\frac{-2r(x,y)^2}{w^2}) \tag{4.2}$$

where r is the distance from the centre of the beam and w is the beam waist radius. This equation is typically presented as a function of the propagation distance z but here I use it simply for modal overlaps at a single point in space and the amplitude, A, of the beam will also be normalised. The integral of the experimental measured mode is subject to a vast amount of noise and detected scatter so the raw data actually should not be integrated over an infinite space and limits should be placed on the outermost perimeter of the waveguide. Alternatively, a Gaussian filter could be applied to remove higher order features. The data presented in figures 4.19(a) and 4.19(b) represent the raw and filtered data, respectively; corresponding to a 91.9 % and 63.3 % coupling efficiency, η. The filtered data uses an unbound integral but the severe drop in efficiency

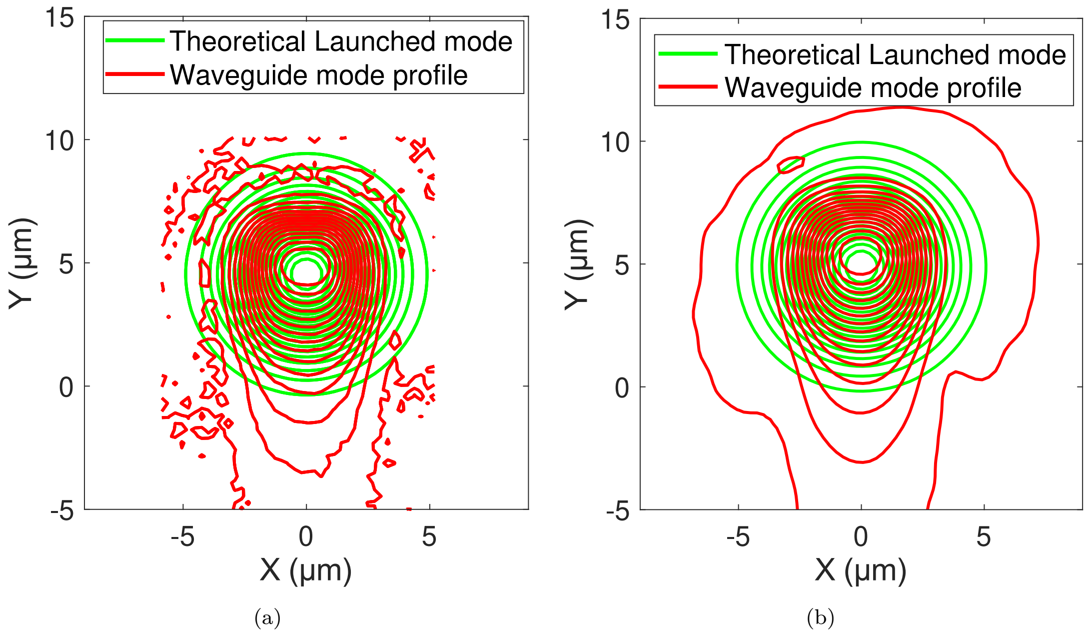

Figure 4.19: Modal overlap of the waveguide mode and a theoretical launch mode. (a) The raw data which has had integration limits placed on it it presented and (b) the same waveguide profile with some of the noise features filtered out.

is still a result of light outside the bounds of the waveguide contributing to the integral. Hence, limits were still applied but at the outer bounds of the data displayed in the figures. Thence, the coupling efficiency associated to the filter data is now calculated to be 88.9 %. The typical insertion loss of these waveguides never exceeded 3 dB; we can now estimate the propagation loss of the narrowest waveguide of chip C121A which was used in the future sections for nonlinear conversion by simply accounting for this calculated launch efficiency and the Fresnel reflection, R, occurring at the waveguide facet,

$$\alpha_{780} \quad [\mathrm{dB/cm}] = \frac{1}{L} 10 \log_{10} \frac{\eta(1-R^2)}{P_{out}}. \tag{4.3}$$

Using the two previously calculated coupling efficiencies for the raw and filtered data, the propagation loss for the 780 nm mode, pump, is now estimated to be 1.4 dB/cm or 1.3 dB/cm, respectively. It should be noted this is likely to be the upper limit of an estimation for propagation loss as experimentally achieving a nigh-perfect coupling efficiency is implausible. Nevertheless, these values give some indication as to the order of magnitude of the propagation loss and will be of use in future sections to extract a nonlinear coefficient estimation for the SHG conversion process in this waveguide.

4.5 Vertical external cavity surface emitting lasers

Moving towards a small footprint system that includes the pump laser and nonlinear waveguide, I investigate the applicability of using a new vertical external cavity surface emitting laser (VECSEL) as the source to pump the SHG process in the waveguides presented in this chapter. VECSELs are a relatively new gain medium in the laser development area of research. Briefly, the gain medium is designed as a series of quantum wells in which the energy bandgaps of the material and quantum well spacing is engineered to achieve the desired gain-bandwidth. For the application of mode-locked sources or highly tuneable sources, the gain bandwidth can be designed to sacrifice power output for a broad gain-bandwidth by aligning the resonance peaks within the structure out of sync with the quantum wells. A saturable absorber is the typical choice of dispersion compensating material for mode-locking. An in-depth review of this technology can be found in Tropper and Hoogland [130]. Ideally for application with nonlinear conversion, a VECSEL would be used in a narrow gain-bandwidth, single-axial mode configuration with high efficiency and power output. However, the information as to how they are typically utilised is relevant as the development is costly and vastly time-consuming. The cost is associated to the highly precise quantum well growth mechanism required and commonly performed via molecular beam epitaxy. For this reason, a broad-band structure will be used in this early-stage collaborative research and has been spectrally narrowed at the loss of power and laser stability. This will be briefly discussed, along with preparation of the VECSEL gain sample, in the following results but the main focus remains on the performance of the lithium niobate waveguide. This work is part of a collaboration with Dr. Jonathan Woods from the Department of Physics and Astronomy in Southampton and Prof. Mircea Guina's group in Tampere University, who supplied the gain material.

4.5.1 VECSEL preparation

The VECSEL gain chip is prepared in-house with the main purpose being to create the heat-sink for the gain material. We utilise silicon carbide as the heat spreader material which needs direct contact with the gain material for efficient heat transfer. For this reason, the two substrates are bonded together via a liquid capillary bond. The underlying physical mechanism for this is the pulling together of two surfaces by surface tension in the liquid [131]. This preparation process will be outlined in this section.

The silicon carbide wafer is diced on a MicroAce dicing machine using the parameter set given in table 4.2. As the edge quality is not critical here, the dicing parameter set was empirically determined with the simple criteria of not damaging the blade and to take a realistic amount of time. The top-side of the wafer is coating in spray-on photoresist prior to dicing to protect the surface from SiC particles during dicing. This is quickly removed with acetone later.

TABLE 4.2: Silicon carbide dicing parameters

Blade	1008 Diamond resin, 400 grit
Speed	0.2 mm/s
RPM	10 k
Depth per cut	100 µm

The SiC and VECSEL gain chip die now undergo a relatively standard cleaning process prior to bonding. This processing step loosely follows advice from the VECSEL material grower but was adapted due to initially poor success with this bonding process. The process is detailed as follows:

- The die are mechanically cleaned and irrigated with methanol, acetone and IPA
- In individual glass beakers, die are sonicated at 50 °C for 30mins in IPA
- Transferred to a shallow IPA bath, figure 4.20(a). Surface bonding is started under liquid
- Removed from the IPA bath and then the interface is compressed with a soft plastic tweezers

The sample is then mounted into the copper heat-sink which will be water-cooled when in operation. Ideally, following the cleaning and bonding steps, the interference fringes

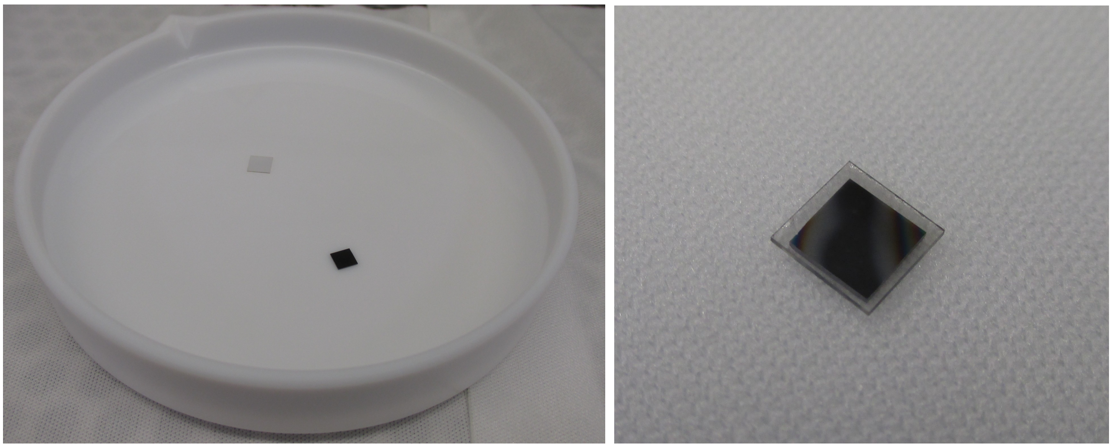
(a) (b)

FIGURE 4.20: Photograph of the process which lead to successful bonding of the VECSEL gain sample and the SiC heatspreader. (a) Initial submersion in IPA in a shallow Teflon tray. (b) A demonstration of the distortion in the fringe pattern observed when there is a successful bond prior to clamping in the holder displayed schematically in figure 4.21.

caused by the gap between the SiC and the gain chip will decrease in frequency. The interface appears dark when a bond has been successful, figure 4.20(b), but some success was had with a bond with the fringes still visible prior to clamping.

4.5.2 Zn-indiffused PPLN waveguide characterisation

The VECSEL cavity structure is shown in figure 4.21 along with the placement of the PPLN waveguide within the testing setup. The primary requirement in the design of this cavity was the placement of the birefringent filter which allowed for wavelength selection via filtration of the cavity's longitudinal modes, by introducing loss into the other modes as the filter is placed at the Brewster angle to the cavity mode. It is for this reason that the phasematching curve in obtained by temperature sweeping as the large discrete steps in wavelength did not have the resolution required to characterise the waveguide.

Furthermore, the collimated cavity mode prior to the output-coupler, OC, was advantageous for the nonlinear waveguide characterisation as it required a single lens to focus into the waveguide. For future work in which a VECSEL could be developed for the miniaturisation of such a UV source utilising a nonlinear waveguide, it is likely that the device would benefit from fibre-coupling the VECSEL output for alignment stability into the PPLN waveguide. In this work, two mirrors were used to direct the 780 nm-light to the PPLN launching station, as indicated by the travel path of the dotted beam, but this was only for preferable optical-bench placement. If one wished for this to be a commercial, miniature product, placing the PPLN waveguide and launching lens directly at the OC would be apt. Further details on this cavity can be found in ref. [114] as this PhD thesis is primarily centred around the operation of the nonlinear conversion elements. A further band-pass filter is implemented prior to the SHG photodiode, PD2, to ensure isolation of the correct signal. The loss of SHG power associated with the DM and BPF is 0.37 dB and is accounted for in any presented data. This is the same BPF used in previous low power, lock-in detection characterisation of these waveguides.

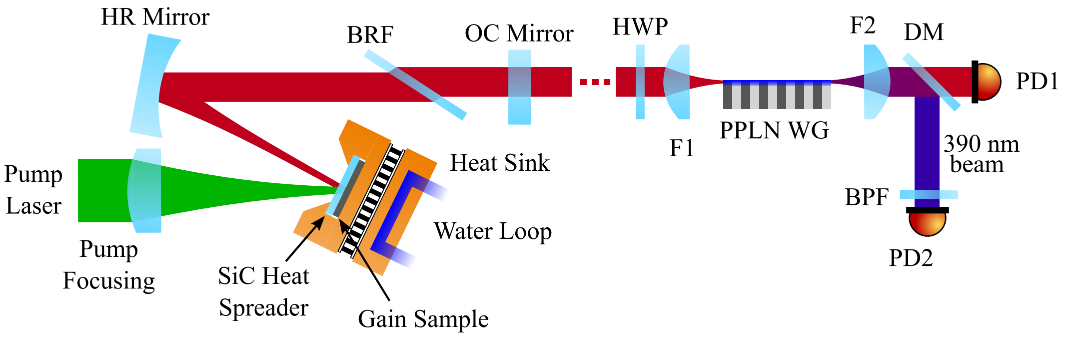

Figure 4.21: The VECSEL cavity configuration and the position of the PPLN waveguide in the setup. The previously described bonded sample is labelled as the gain sample and the PPLN is tested as an extra-cavity, single-pass component.

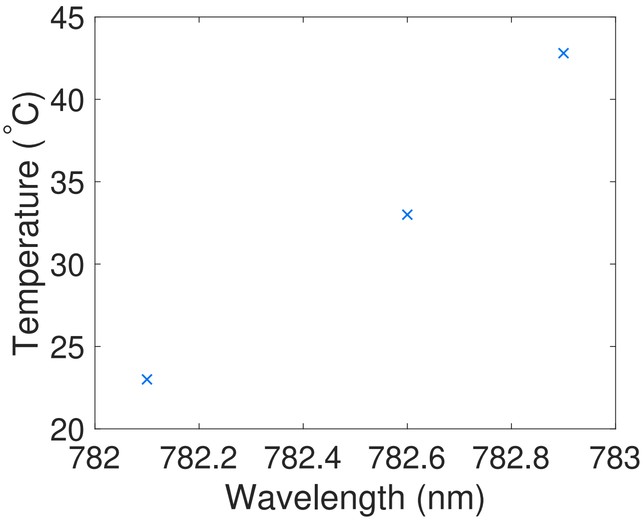

FIGURE 4.22: Phasematching temperature for the PPLN waveguide used in combination with the VECSEL source with respect to pump wavelength. Data deduced from both the previous ECDL characterisation and VECSEL wavelength selection. The wavelength separation in the higher two data points corresponds to the minimum resolution of tunability with the VECSEL source.

The analytical solution for the generated SHG power, $P_{2\omega}$, in nonlinear optical waveguides is calculated as [9]

$$P_{2\omega} = \frac{8\pi^2 d_{\text{eff}}^2 \mathfrak{I}_{ov}^2}{\lambda_\omega^2 \epsilon_0 c n_{\text{eff}}^3} P_\omega^2(z=0) \left(\frac{\exp(-\alpha_\omega L) - \exp(-\alpha_{2\omega} L/2)}{\alpha_\omega - \alpha_{2\omega}/2} \right)^2, \tag{4.4}$$

where n_{eff} is the effective index of the guided SHG mode and d_{eff} is the effective second-order nonlinear coefficient. It is now possible to estimate d_{eff} given the previous evaluation of the overlap integral and loss, given in section 4.4.1. At this point, it should be noted the requirement to utilise numerically calculated values for $\mathfrak{I}_{ov}$ and $\alpha_{\omega/2\omega}$ is not strictly necessary. Other work from our research group, presented in [103], used a Fabry-Perot loss measurement technique to estimate this value for a waveguide designed for 1560-780 nm SHG. Other works using similar waveguides made use of an InGaAs camera for modal characterisation for both the pump and SHG wavelengths. A portable, higher power EDFA enabled *in situ* SHG to image the exact mode generated [4], once the 1560 nm signal is sufficiently extinguished prior to imaging. This enabled fewer assumptions and numerical investigations to extract a value for the nonlinear overlap integral and is an area for development in future work.

A nonlinear least-squares fit using the calculated propagation loss for the pump wavelength as 1.3 dB/cm to the data presented in figure 4.24 can ascertain a value for d_{eff} once all other parameters in equation (4.4) are known or calculated. I approximate the propagation loss of the SHG mode is $2\alpha_\omega$ as this is an assumption historically taken in literature, specifically by Parameswaran *et al.* [132]. Given the requirement for $P_\omega^2(z=0)$, this is calculated by accounting for the propagation loss calculated for the 780 nm mode.

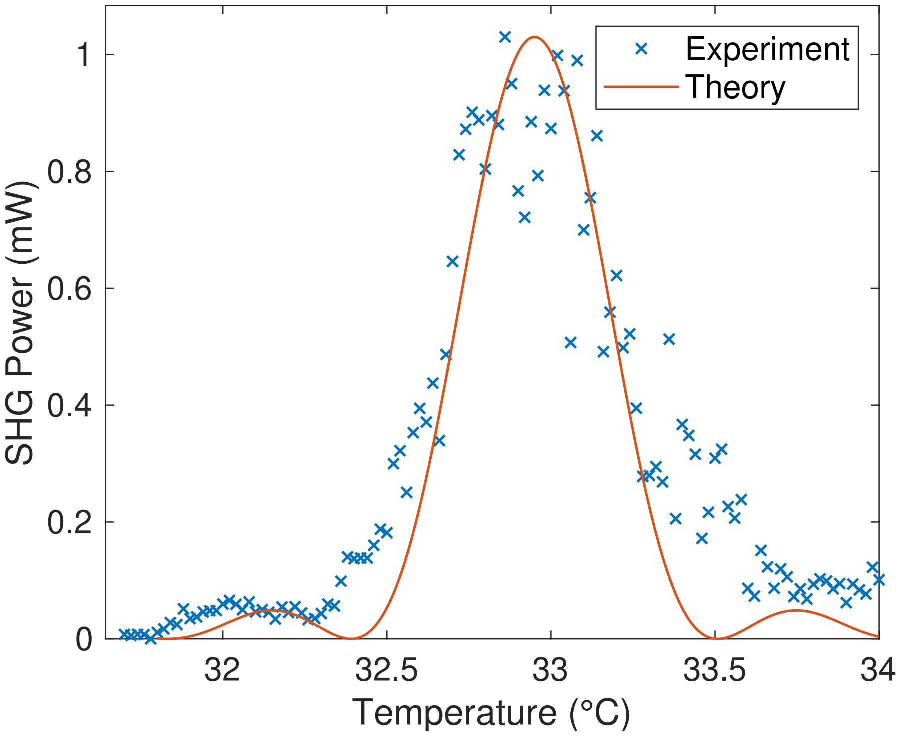

FIGURE 4.23: Temperature sweep for the maximum SHG power obtained throughout these experiments using a VECSEL as the pump source for SHG to UV light. The theoretical curve shown is calculated using the standard Sellmeier equations for bulk MgO:PPLN.

Thence, d_{eff} is evaluated to be approximately 2.7 pm/V, or a d_{33} of 4.3 pm/V. This fit equates to a normalised conversion efficiency of 5.45 ± 0.08 %/W. This maximum efficiency obtained was 6.9 %/W which was obtained for the data presented in figure 4.23.

While it is typical to see reduced d_{eff} values for waveguides in comparison to bulk crystal values for LN [27], in our work we anticipate this is a result of the diffusion profile of zinc into the crystal's lattice structure resulting in a non-uniform profile of d_{eff} across the propagating mode. Secondly, the fabrication challenges associated to the fine-period domain poling will also feature in an overall reduction of the observed nonlinear coefficient as the domain grating has not been accounted for in the calculation. Finally, the estimation methodology of propagation loss plays a key role in the d_{eff} evaluation as the propagation loss of the SHG mode is likely higher than estimated as, at this blue/UV wavelength, material absorption is non-negligible. The rigorously evaluated d_{eff} from higher power telecoms sources and a more mature version of this technology developed for 1560-780 nm evaluated d_{eff} to be 7.6 pm/V [4]; potentially indicating the grating is averaging to perform as efficiently as a third-order grating structure. To date, these waveguides are only modestly efficient with respect to other competing research in this area. For example, Eigner *et al.* [133] recorded a similar efficiency in their recent work for an output power of 4.9 µW for the SHG of 396 nm light. Given the identification

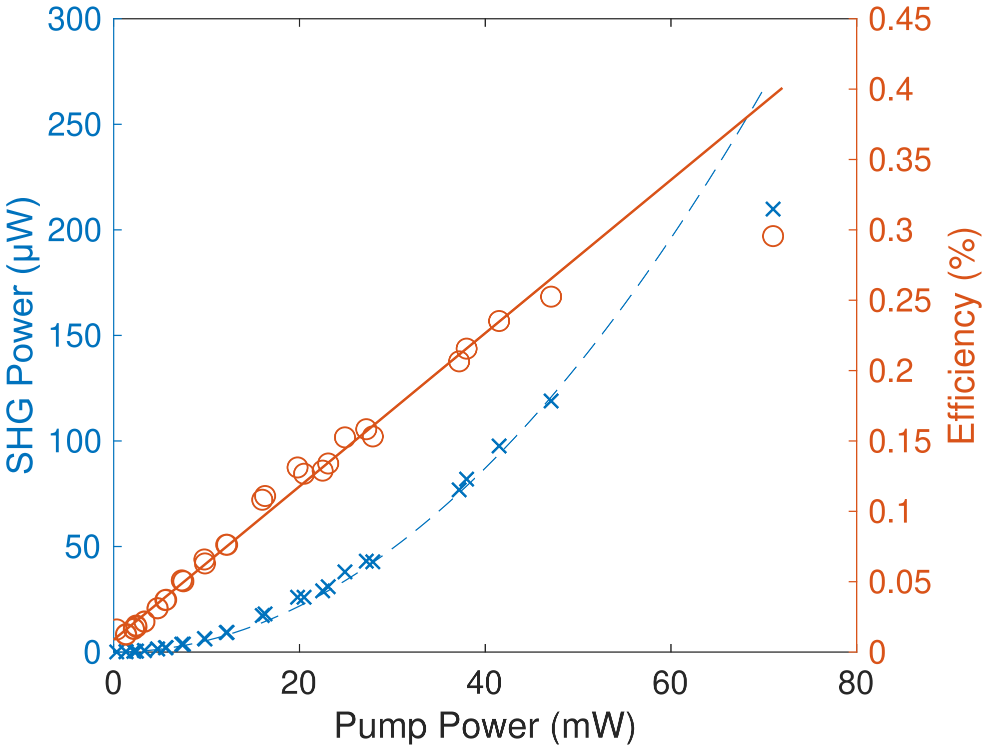

FIGURE 4.24: SHG power as a function of pump throughput power for low pump powers. Taken via attenuation of the VECSEL beam directly after the output coupling mirror.

of the challenge associated to the fine period QPM grating, there is the potential to intentionally use a third-order grating and fabricating a 40 mm-long waveguide; the limited length waveguide selected in this work was chosen for the region in which the QPM grating qualitatively looked optimal and intact. Given recent work demonstrating the high damage thresholds of this technology [4], there is currently no evidence that the waveguides operating at these wavelengths will not also have a high damage threshold; enabling future applications requiring higher optical powers of blue/UV light given the development of an appropriate pump source.

4.6 Conclusions

Nonlinear waveguides designed for conversion of 780 nm to 390 nm have been presented. This work is a key step in developing the zinc-indiffused PPLN waveguiding technology for shorter wavelength conversion. This technology builds upon the expertise in the fabrication of bulk crystal PPLN which has been developed here in the University of Southampton and Covesion Ltd. and knowledge of high-precision, optical quality dicing processes.

After initial testing, the most efficient waveguide was demonstrated to operate for conversion to 391 nm with the SHG being a first-order waveguide mode at room temperature in a 2.2 µm period grating. Knowledge of the grating period alone is key information in the development of this technology as the process parameters are empirically mapped for the currently unknown effective index of these waveguide due to the indiffusion of zinc into the LN lattice.

Finally, due to the limitations of commercial lasers working in this wavelength band, a collaboration with VECSEL researcher groups was undertaken and discussed. This provided a novel route for creating small footprint blue/UV sources for application in ion trapping systems and enabled the zinc-indiffused PPLN waveguides to be tested with higher optical power to investigate nonlinear parameters which are extracted from the corresponding quadratic relation to input power. With further work being completed in the development of shorter wavelength, narrow linewidth VECSEL sources, this collaboration has potentially opened a door to testing shorter grating period PPLN waveguides in future projects.

As previously alluded to, there is a lot of detail and interesting fabrication-related information which can be extracted from the phasematching spectrum of the nonlinear conversion process. The waveguide which was nominally 5 µm-wide in the 2.2 µm period grating on chip C121A provides the basis for Chapter 5 in which a characterisation methodology is detailed and utilised.

Chapter 5

Numerical technique for investigating PPLN waveguide uniformity via SHG phasematching spectra

5.1 Introduction

It is well-known that the conversion efficiency of a nonlinear waveguide, and indeed the base nonlinear material, is vastly dependent on the fabrication quality [134]. For waveguides, it is the uniformity of the guided mode which is of vital importance. In ridge waveguides, a constant waveguide width is the foremost concern following the optimization of side-wall roughness to minimise propagation loss of the guided beam. However, conversion efficiency is not always the main concern when utilising nonlinear waveguides. For experiments and technologies which rely on quantum optical properties of nonlinear conversion, adhering to the theoretical spectrum required for certain schemes which make use of either time-spectral entanglement [135] or uncorrelated photon pairs [136] necessitates the fabrication process does not nullify the theoretical efforts. The search for uncorrelated pairs has driven a vast amount of research to investigate the uses of nonlinear material and wavelength choice to optimise this [63, 137, 138, 139] but work employing spectral engineering via the nonlinear crystal has permitted a versatile engineering route while still using PPLN as the nonlinear material [51, 140].

Hence, an obvious requirement is the means to characterise the dimensions of the fabricated waveguides to troubleshoot faults in the process flow when the obtained spectra does not match theoretical predictions; allowing for distinction between issues with diffusion or side-wall definition as the two predominant steps to create a ridge waveguide such as that shown in figure 1.2. Additionally, the manufacturing cost per waveguide can be substantial and therefore a non-destructive physical characterisation is preferential. Prior to the development of optical waveguides in $\chi^{(2)}$ materials, fabrication of the QPM grating structure was the primary concern and this was discussed in detail by Fejer *et al.* [128]. This work included rigorous discussions regarding missing domains, unintentional grating chirp and random error in domain position. While PPLN fabrication is still not trivial, advances in photolithography equipment and cleanroom conditions have reduced the emphasis in current literature's discussion on bulk PPLN fabrication challenges. As discussed in Chapters 3 and 4, waveguides provide the potential for an increase in longitudinal spatial confinement between the pump and generated signal in comparison to bulk crystal focusing conditions developed by Boyd and Kleinman [54]. However, the numerical means to investigate the fabrication limitations in these waveguides has not been thoroughly examined.

In previous years and decades, there was limited literature in the area of numerical modelling of waveguide non-uniformity. This is justifiable as the first developers of the fabrication process could simply dispose of waveguides that are non-ideal in their conversion efficiency. However, some investigations regarding waveguide width uniformity have been undertaken. Laurell and Arvidsson discussed diffusion fluctuations in channel waveguides in birefringent phasematched lithium niobate (LN) [85]. They assume a parabolic propagation constant function to act upon their phasematching conditions with good experimental agreement. More recent work by Umeki et al.[134] assumes a sinusoidal function with an inverse dependence on waveguide length to conclude their bonded, thinned and diced PPLN waveguides are close to optimal fabrication. Nevertheless, Umeki *et al.* clearly correlated the distortion of a measured phasematching spectrum in their waveguides with a decrease in maximum conversion efficiency. Chauvet *et al.* also numerically investigated how a linear variation in waveguide width along the length of their LN ridge waveguides could form two phasematching peaks in their experimental spectrum [141]. In addition, they calculated that a 200 nm width variation would drop their conversion efficiency to one-third of its maximum potential; further justifying that a technique to characterise fabrication errors would be advantageous.

More recently, a surge of papers that rigorously investigate nonlinear waveguide fabrication tolerances has occurred, from both engineering and a physics/numerical point of view. With clear motivations from the application of nonlinear waveguides designed for spontaneous parametric down conversion in quantum optics experiments, Santandrea *et al.* has shown how waveguide width variational noise will have consequences on experimental results [142, 143]. Gaussian and $1/f$ noise superimposed on the waveguide's width is modelled and it clear the conclusion of this analysis is that uncorrelated noise appears to have very little effect on the phasematching spectrum. $1/f$ noise which does impose low frequency trends in the waveguide width clearly influences the spectrum away from the ideal sinc^2 curve. Interesting conclusions from this body of work include that an experiment may benefit from using short nonlinear waveguides if the fabrication process is not optimised, as opposed to aiming for the higher conversion efficiencies of longer devices. In the case of investigating waveguide nonuniformities for a chirped domain inversion grating, there exists a method by Chang *et al.* [144] that utilises frequency resolved optical gating from which spatial information can be obtained from the spectral response. This is possible as the chirped grating generates a compressed or expanded pulse generated through SHG as it travels through the waveguide but is only applicable to pulsed optical characterisation.

In this chapter, a numerical understanding of fabrication tolerances in an arbitrary PPLN waveguide is discussed, followed by a description of the method which is proposed and used to characterise the PPLN ridge waveguides presented in Chapter 4. This methodology is intentionally straightforward in its application as simple utilisation is preferable for an industry or academic designing a troubleshooting process. Finally, the preliminary success of the method is presented.

5.2 The effect of waveguide nonuniformity on the phasematching spectrum

Developing on the 3-photon nonlinear couple-mode equations given in section 2.3.2, we can numerically investigate the effect on the phasematching spectrum in which a spatially dependant propagation constant would incur along the length of the waveguide. Equation 2.31, associated to the pump photons, is only slightly modified as the effective index is changing along the length of the waveguides. In turn, this alters the phasematching relationship, expressed in $\Delta\beta$. This is essentially identical to the type of numerical models presented in Refs. [141, 134, 85] and does not deviate from standard nonlinear generation mathematics. The modification to this is a length dependant propagation constant,

$$\Delta\beta = \Delta\beta_0 + \delta\beta(L) \tag{5.1}$$

where

$$\delta\beta(L) = \beta_i(L) - \beta_{\mathrm{min}}. \tag{5.2}$$

To gain some intuitive understanding of the effect that this parameter has on the phasematching spectrum, we can now input some basic mathematical functions and numerically calculate the result. For simplicity, I shall restrict this to a straightforward investigation of linear and quadratic relationships for the $\delta\beta(L)$ term. These, at least, have some potential to be realistic as one could imagine a scenario in which a photolithographic pattern for fabricating a straight channel waveguide has an imperfection which

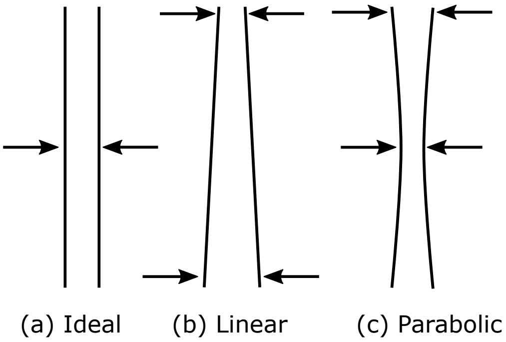

FIGURE 5.1: Simplified representation of the waveguide width profiles which may exist in fabrication devices. The actual function representing thickness will be dependent on the geometric dispersion profile but this has an almost linear relation relation in the Zn-indiffused PPLN ridge waveguides.

gets wider down its length. Or perhaps an intrinsic strain for a waveguide being fabricated in the centre of a wafer may lead a symmetric, quadratic function representing the phasematching modification in the waveguide.

Mostly, the waveguides demonstrated in this thesis operate for SHG around ~782 nm (Chapter 4) and hence, this spectral region is chosen for this numerical study. The presented results in figures 5.2(a) and 5.2(b) correspond to relatively small maximum offsets for a linear and quadratic relation, respectively. The functions are displayed in figures 5.2(e) and 5.2(f), in the same column as the numerically modelled spectrum. The $\delta\beta_{\max}$ values of $100\,\mathrm{m}^{-1}$ and $1000\,\mathrm{m}^{-1}$ correspond to total width variations of approximately 60 nm and 540 nm, respectively, for the 780 nm PPLN ridge waveguides around a centre waveguide width of approximately 6.8 µm-wide. While these values represent the extreme ends of fabrication tolerances, as will be presented in section 5.4, they are realistic tolerances of our current dicing capabilities.

The linear function has introduced a minor reduction in the quality of zero-points for the expected sinc^2 spectrum. This is somewhat intuitive due to breaking the symmetry of the power generation and growth throughout the nonlinear material. This is similar to the discussion in section 5.3.4 for the effect which propagation loss has on the phasematching spectrum. Applying the centrally-symmetric quadratic-relation results in an asymmetry from the ideal sinc^2 curve, evident in figures 5.2(b) and 5.2(d). A value of $\delta\beta_{\max} = 1000\,\mathrm{m}^{-1}$ in the ~780 nm region corresponds to a change in central wavelength of <0.1 nm if we assume a constant, uniform hypothetical waveguide. Hence, it is obvious that a width variation equivalent to this will vastly distort the phasematching spectrum. At this point, a more rigorous analysis is clearly required if one wished to investigate and troubleshoot specific fabrication issues rather than relying on common features in the phasematching spectrum; this is the basis of the body of work presented in this chapter. I now make an argument that we have the technology and numerical techniques to advance on work presented in previous literature to experimentally characterise fabricated waveguides.

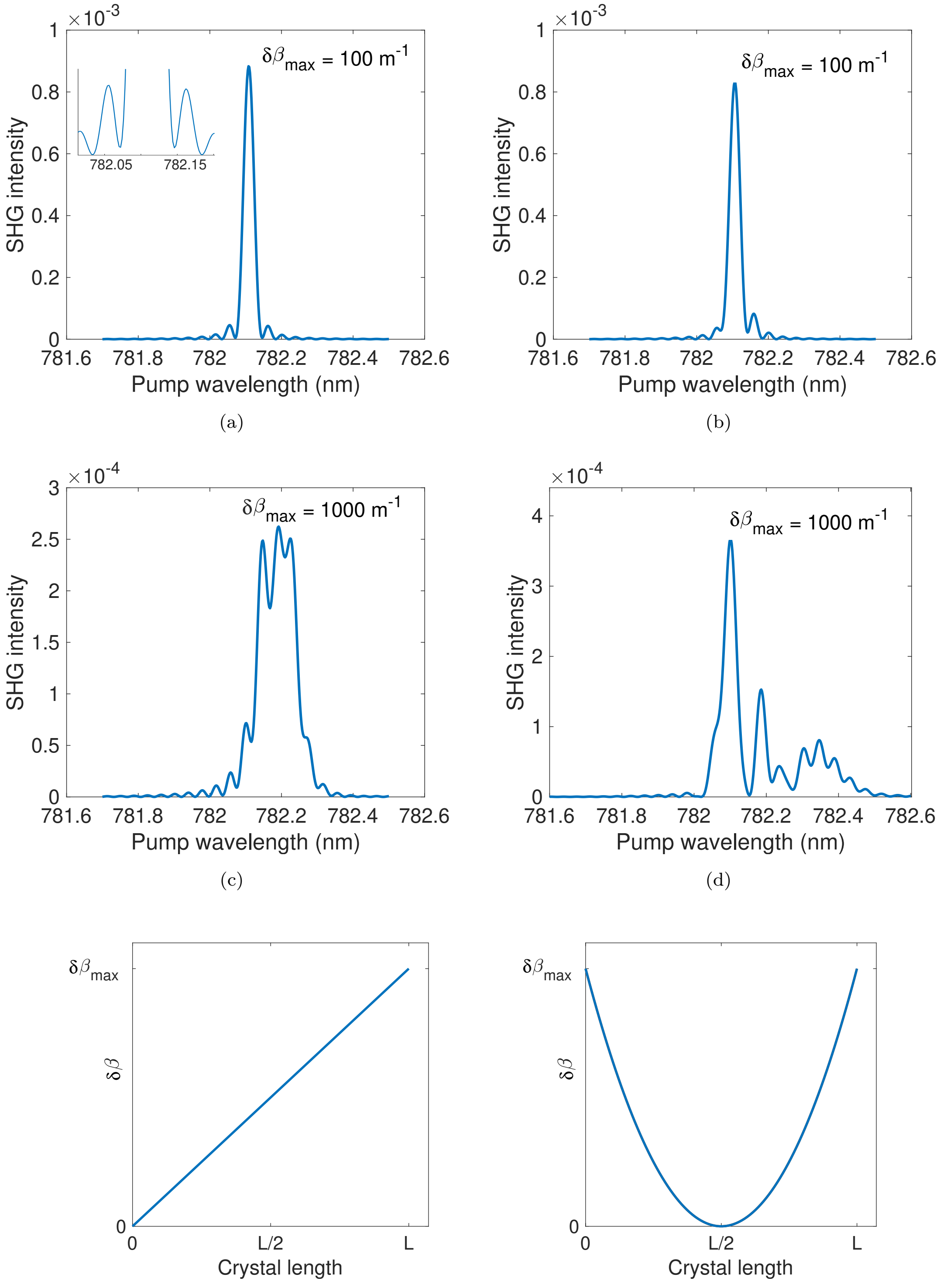

(a) (b) (c) (d) (e) (f)

Figure 5.2: The phasematching curves generated by numerically solving the three-photon ODEs with variable propagation constant along the length of the waveguide. Different maximum propagation distortion values for a linear profile is seen in figures (a) and (c). The inset to (a) inset shows symmetric non-zero points surrounding the central sinc^2 lobe. (b) and (d) correspond to centrally symmetric quadratic function imposed on the propagation constant profile. (e) and (f) present the function type of $\Delta(\Delta\beta$ superimposed on the data of the figures positioned above each, respectively.

5.3 Methodology overview

In the characterisation of ridge waveguide uniformity along the propagation length, there exists a large number of potential characterisation tools. Scanning electron microscopes (such as that used in Chapter 4) were considered but the requirement to deposit a conductive material (such as gold) on the surface increases the likelihood of damage. Atomic force microscopy (AFM) offers only a small measurement area to be imaged and the potential to damage the probe tips at the ridge edge prohibits their applicability. Stylus profilometry is a similar technique in which a (typically) diamond tip is dragged across the surface to characterise a sample's surface. Although there is potential to optimise the contact force between the probe and sample, the likelihood of waveguide damage is still a potential risk. By contrast, white light interferometry is a non-destructive characterisation technique with no requirement for a surface coating, it is inherently poor at dealing with edges (which will prove to be advantageous) and is commercially available with larger scanning areas and high precision stages to monitor position in the waveguide.

5.3.1 White light interferometry

White light intererometry (WLI), as the name indicates, utilises the short coherence length of a single, broadband light source to form an interference pattern from a reference mirror and the sample under investigation. An almost identical path length between the reference arm and sample is required to form a interference pattern. In the simple case of identical powers in each beam, the phase difference determined by path length generates the constructive or destructive intensity pattern.

The fringe pattern is generated as the path length between the sample and reference arm is altered. This translates to a vertical raising or lowering of a sample, portrayed in figure 5.3. A full translation through the coherence length will provide a moving fringe pattern associated to the changing optical path difference within the interferometer, as seen in figure 5.4. It is usually considered more reliable to fit an envelope to the fringe pattern rather than numerically fitting to the complete pattern. This process will be performed for each individual pixel to characterise the height profile of the sample and generate the surface profile. More details regarding these methodologies and algorithms for analysing the fringe pattern can be found elsewhere [146, 147], however the algorithms used by the commercial Zygo ZeScope WLI used in this work likely contain some proprietary optimization.

WLI is typically used for studying roughness of a surface, such as machined waveguides [115] or more standard deposition techniques. However, it is relatively intuitive to see that this technique relies on the directionality of the reflection beam, it will be incapable of collecting data from a rapid drop in sample height. This is often quoted as the main

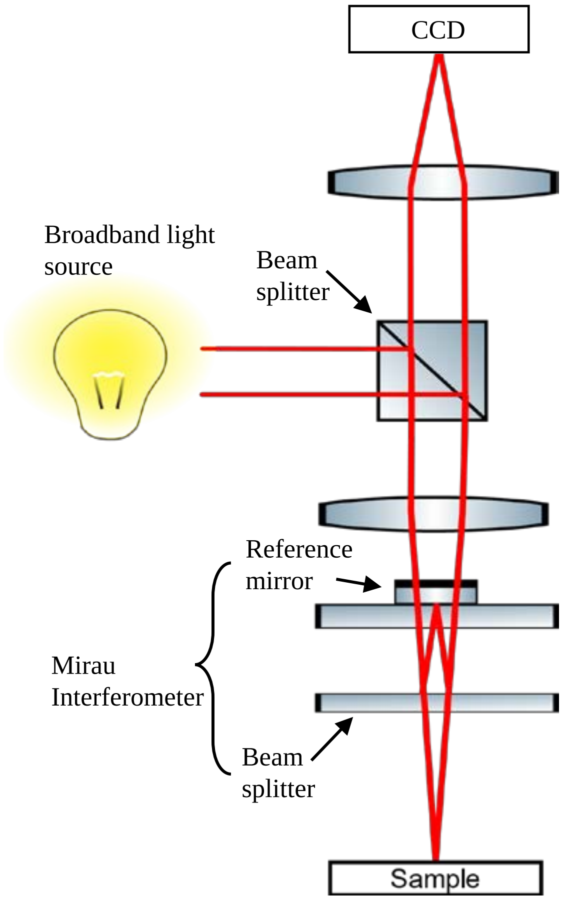

FIGURE 5.3: Simplified schematic of the commercial white light interferometer used in this work to characterise the PPLN waveguide width uniformity.

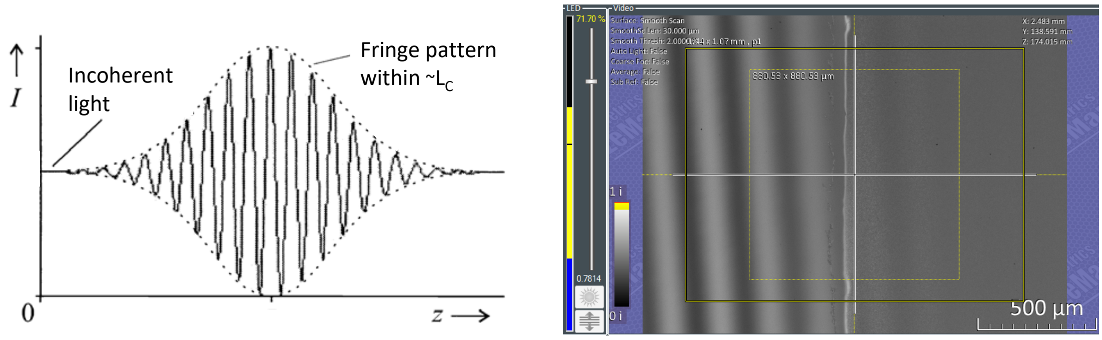

Surface: Smooth Scan
SmoothSc Len: 30.000 µm
Smooth Thresh: 2.0000 %
Auto Light: False
Coarse Foc: False
Average: False
Sub Ref: False

X: 2.483 mm
Y: 138.591 mm
Z: 174.015 mm

(a) (b)

FIGURE 5.4: (a) A typical fringe profile as the sample is raised through the range of which their exists temporal coherent; image was adapted from Ref. [145]. (b) An example fringe pattern of a sample on the particular commercial WLI and associated software used in this work. Photograph courtesy of Charlie Turner.

disadvantage of WLI and is due to the reflected light not falling within the numerical aperture of the collection lens. In terms of the final image created (greyscale/bitmap), this is an intensity reduction which can be taken advantage of to quickly and simply determine ridge waveguide width using available edge detection algorithms.

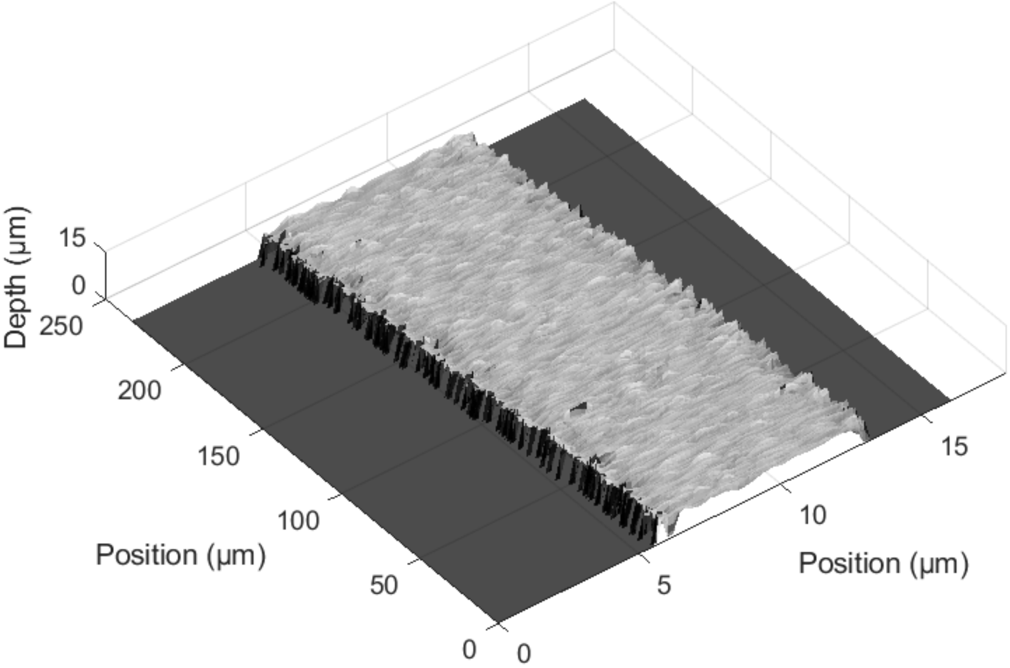

FIGURE 5.5: Example raw data which is extracted from the WLI. This data will be processed to create a single average waveguide width point for characterising the width profile of the PPLN waveguide.

5.3.2 Edge Detection: Canny Method

An edge-detection (ED) technique is now required to computationally calculate a ridge width over the length of the waveguide that is compatible with the WLI data. As this task is relatively simple given the mechanism in which a WLI computes an image, the development of a bespoke algorithm is not required. There are many potential options which would have been suitable so I will only discuss the algorithm of choice here and the reasoning behind this selection.

Full details of the Canny method can be found in the original reference by Canny [148]. Briefly, this algorithm applies a Gaussian filter to smooth the image. This removes noise with the intent to remove the number of detected points. Following the filter, the derivative of the remaining image intensity data is used to find real edges. The key difference between the Canny method and other ED techniques is the fact it uses 2 thresholds to enhances its ability to detect both strong and weak edges, both of which may be real and not caused by noise. An alternative option to this method is the Prewitt method [149] which was developed almost two decades before Canny's work.

This method is comparatively simpler and identifies intensity gradients to locate an edge.

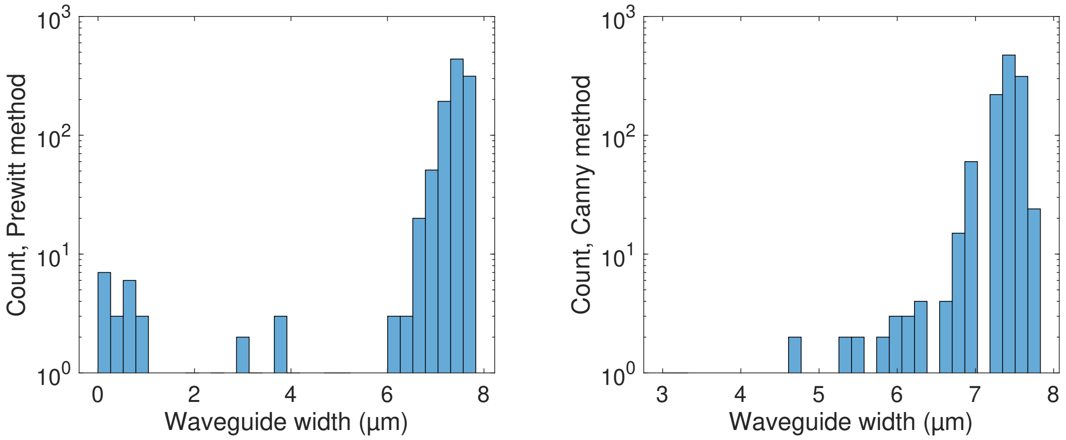

(a)

(b)

FIGURE 5.6: Skew of the associated edge detection methods can be seen, including the unrealistic error in detection for the Prewitt method on the WLI data.

While the Canny method is considered exceptionally robust for image recognition, it was selected here as it provided fewer erroneous data points. It is simple logic to conclude that the requirement to remove fewer calculated values is more honest data manipulation and analysis. The final detail of the methodology for the data in figure 5.6 is discussed in section 5.4.

The edge points detected on the top surface of the waveguide are not to be of concern here as they can be removed from the waveguide width calculation in the post data analysis process. The Prewitt method is clearly more susceptible to detecting surface roughness points as the larger number of calculated waveguide width points below 2 µm is indicative that two surface roughness points on the same row were the chosen edge points. This is clearly non-physical and provides evidence for proceeding with the Canny method.

5.3.3 Diffusion waveguide model

Prior to proceeding with the numerical model of the phasematching spectrum, a model which represents the waveguides is required. For this, FIMMWAVE (Photon Design Ltd.) can be easily applied as a mode solver. While the width of the model is to be investigated, the diffusion depth can be estimated using some assumptions. Firstly, we assume a maximum Δn of 0.003. This is in accordance with the research from Young *et al.* [98], who completed the original fabrication of zinc-indiffused waveguides and characterised the modulation of refractive index due to zinc. However, the research presented here is in MgO:LN and hence we would like to limit the assumptions to this value only; metallic zinc is also used here in comparison to ZnO in Young's work. Hence, I have not utilised any more of their empirical diffusion parameters.

A Gaussian diffusion profile is used to approximate the refractive index profile which creates the planar waveguide fabrication before dicing. As per figure 4.10, the vertical (y-axis) MFD was set to be ~ 5.5 µm. This corresponded to a Gaussian standard deviation of 6 µm. In accordance with the type-0 nonlinear interaction, the effective index of the fundamental TM mode is selected from the resulting solution modes. We now need to convert to the waveguide propagation constant, as this is the parameter required for equation 2.30. Over the range investigated, a quadratic fit easily represents a function of this dependency, as presented in figure 5.7(b)

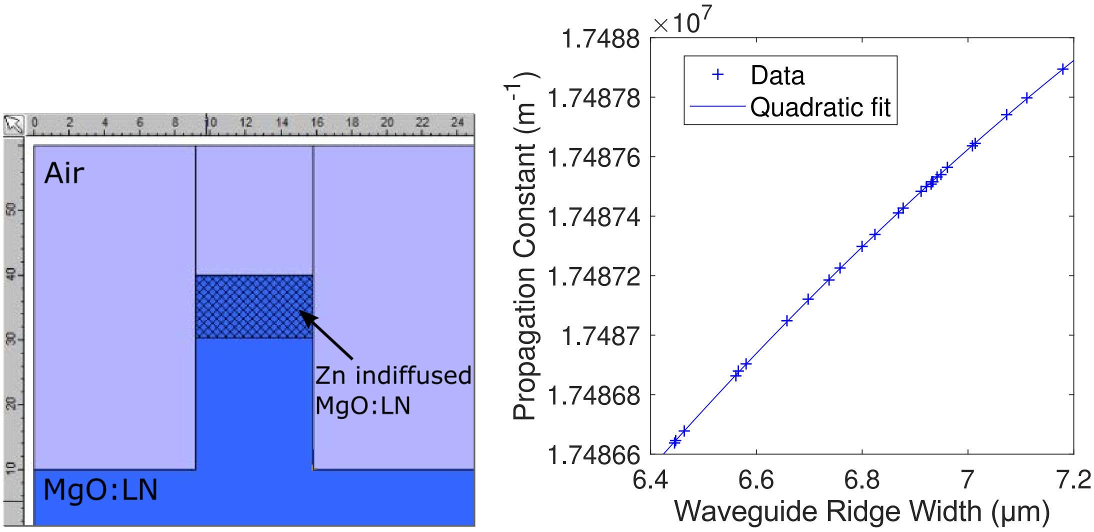

(a) (b)

FIGURE 5.7: (a) The geometrical profile of the model estimated to represent the Zn-indiffused PPLN waveguides discussed and used in this work. (b) Propagation constant of the fundamental TM mode as a function of waveguide width which was determined by the FIMMWAVE model.

5.3.4 Loss dependency spectrum

As stated, loss has not been included in the three-photon ODEs given in equations 2.30 and 2.31. This short section aims to justify this assumption. It is intuitive to understand that absorption loss will decrease the maximum conversion efficiency of the phasematching spectrum. Additionally, this efficiency reduction "flattens" the sinc^2 curve and inherently broadens the bandwidth (or FWHM) of the central sinc feature, as mentioned by Shen [150]. Due to the signal generation occurring as the pump electric field passes through the nonlinear waveguide, there is still uncertainty in the community as to whether absorption loss will cause asymmetry in the phasematching spectrum. Using equations 2.30 and 2.31, as before but now having a non-zero α_i, figure 5.8(a) conclusively demonstrates that absorption loss for any realistic value is not contributing to asymmetry in the spectrum. However, the asymmetry in signal generation due to loss in the waveguide presents itself as a removal of the zero-crossing values in the spectrum. As previously mentioned, the zero points occur at the non-zero $\Delta\beta$ value in which the generated power in the first half of the crystal is perfectly transferred back to the pump in the latter half. One can intuitively see the elimination of zero points is because this condition can not be met with high absorption loss. These first so-called zero points occur at $\pm\pi$. Using this information, we can create a situation where a single input frequency is being characterised and this satisfies the $\Delta\beta$ condition which corresponds to the $\mathrm{sinc}(\pi)$ value in an analytical solution. This is a clear demonstration of the effect propagation loss plays on the phasematching spectrum in SHG. It is convenient to be able to apply the presented method for characterisation of a waveguide without needing to know its propagation loss value.

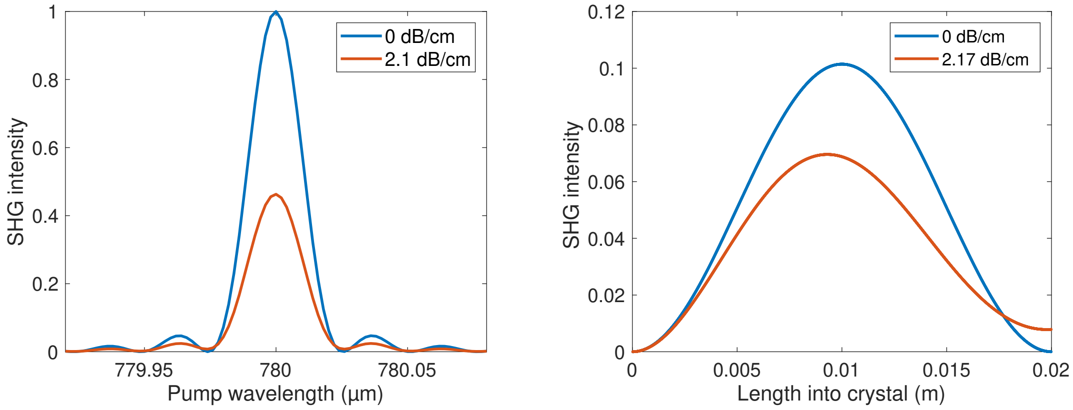

(a)

(b)

FIGURE 5.8: (a) Numerically calculated phasematching spectra for a 20 mm-long PPLN crystal for different propagation loss values and (b) the SHG power throughout the length of crystal for the first zero point of the phasematching spectra in the zero loss case.

5.4 Technique verification using a Zn indiffused PPLN waveguide designed for SHG of 780 nm

To verify the applicability of the WLI/ED methodology it naturally requires a comparison to a fabricated waveguide which can be experimentally interrogated. For relevance to this thesis, the chosen PPLN ridge waveguide was presented in Chapter 4 for 780-390 nm SHG, sample C121A. The waveguide with the furthest phasematching spectrum from the ideal $\mathrm{sinc}^2(x)$ curve is preferable to study in the early stages of making use of this method. It could be easily argued that any subtle differences could be attributed to something as simple as temperature uniformity in the crystal, hence an early investigation would want to avoid this. The chosen waveguide was that presented in figure 4.16(a), nominally called the 5 µm wide waveguide.

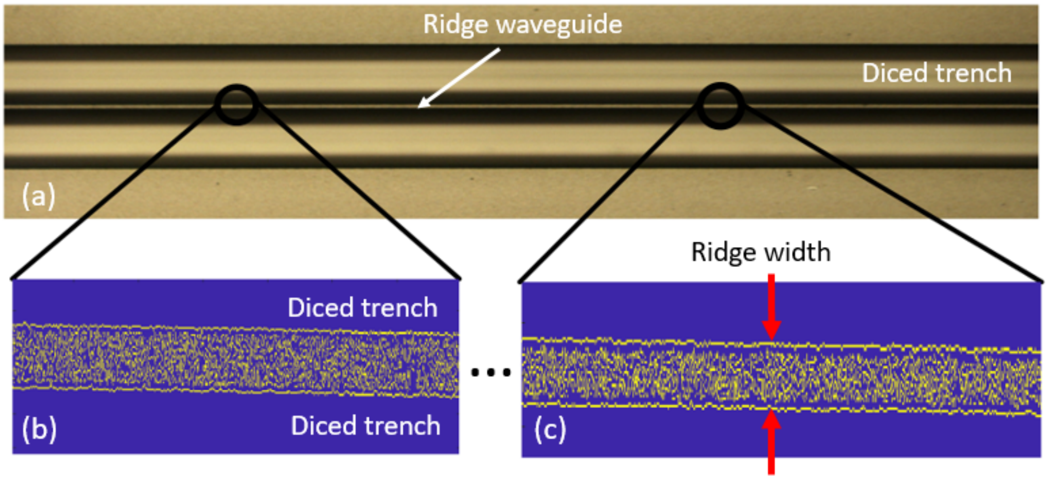

FIGURE 5.9: An illustrative representation of the method presented here to characterising the PPLN ridge waveguides. (a) A top-down optical image of the waveguide. (b) and (c) display the detected edges from example points along the waveguide. The surface roughness points which are incorrectly identified as waveguide edges are clearly observed as edges detected on the top surface of the waveguide.

We are now in a position to discuss how the data from figure 5.6 was acquired using dataset typically represented in figure 5.5. The WLI tool can characterise the surface of a sample of 250 × 250 µm when using the ×50 objective lens, as used in this work. The was the highest magnification available at the time of this work. In order to characterise the waveguide width along its length, a sample surface profile was captured every 0.5 mm. There was no expectation that the waveguide width profile would change at a higher resolution than this as it would be unlikely to guide light if this was the case. The pixel resolution in this data is ~200 nm. The edge detection algorithm is applied to the surface profile of each captured image; for each pixel column, as the data is presented in figures 5.9(b) and (c). The edge detection presents itself as a single pixel data point. The corresponding waveguide width for each column is defined as the furthest two edge points detected. The WLI technique fails to detect the surface when it is outside its interfereogram range, this enables straightforward data analysis to be performed and removing the need to extract any upper bound for waveguide width as would be necessary when handling surface metrology data from AFM/SEM etc. However, some filtering is still necessary to account for the physically undefined lower bound, as shown previously in figure 5.6(b). The data is now treated as a gaussian distribution and data bound beneath a single standard deviation is removed before the calculation of the mean width for each image. Finally, confirmation of the waveguide width data is carried out via measurement of an end facet with a calibrated optical microscope and comparing this to the value determined from the WLI and edge detection routine. The difference in width values was approximately 3 % (6.85 µm compared to 7.1 µm). While this minor difference increases confidence in the method, it was henceforth used as the calibration factor applied to all data resulting from the WLI/ED methods. The resulting width profile is now defined by the 28 mean-width values, shown in figure 5.10.

The third-order polynomial fit to the data, shown in figure 5.10, was chosen as this is the lowest order polynomial which can be logically explained from the ridge waveguide fabrication process. When considering the high precision dicing for these feature sizes, blade wear is an important consideration along the length of the cut. Additionally, the wafer may be deformed in the x- and y-axis due to adhesion to the vacuum chuck. These three factors could cause the geometry of a hyperbolic paraboloid, of which a 2-D slice through this structure is a third-order polynomial. The low-order fit also serves as a route to not over-constrain the fit to a width differential that may not be realistic, potentially remnant from the image recognition steps. We now have a simple function to use in combination with the relation of waveguide width to propagation constant, for this specific waveguide. This demonstrates the use of a 3$^{\text{rd}}$-order polynomial fit to the waveguide width data and the corresponding phasematching spectrum is in good agreement with the experimental optical characterisation data; the curves are shown to have a similar period, asymmetry around the peak lobe and an increase in efficiency of these side lobes.

It should be noted this 3$^{\text{rd}}$ order fit which appears to accurately represent the waveguide is not consistent with literature for the chosen mathematical functions to represent fabrication imperfections. However, the previous work has been undertaken to investigate thermal profiles across a heating element [85] or bonded and thinned PPLN waveguides [134]. While I have presented an argument for not over-constraining the polynomial fit, evidence still needs to be presented this is the case. To confirm my approach, the resulting phasematching spectrum from a 6th and 10th order fit to the waveguide width data are shown in figure 5.12. Both respective spectra show features which have not been seen in any experimental work carried out in this thesis characterising 780-390 nm PPLN ridge waveguides. Interestingly, these numerical spectra have not converged to a spectra which is different from the experimental data but at least similar. This highlights just how sensitive the numerically generated phasematching spectra is to the function representing its propagation constant.

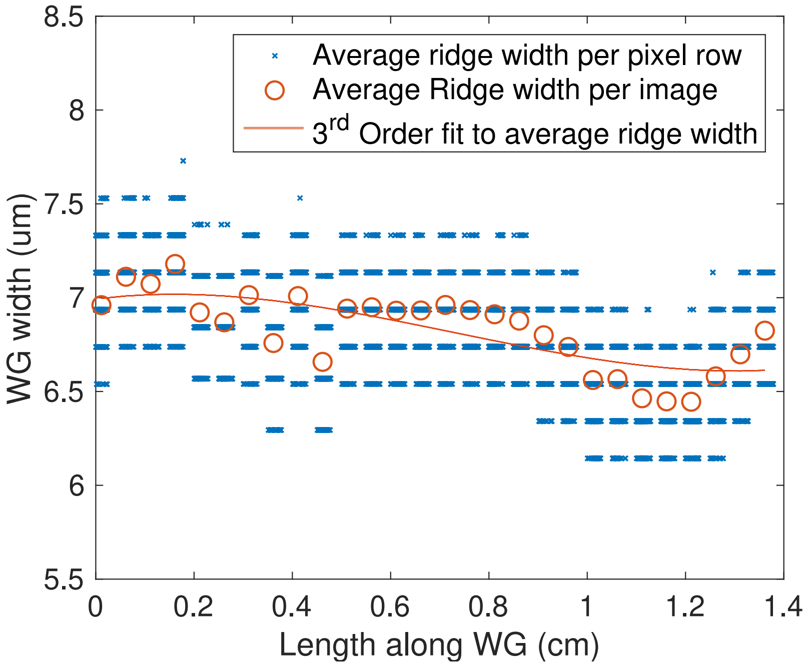

(a)

Figure 5.10: Calculated profile of the zinc indiffused PPLN ridge waveguide designed for 780-390 nm SHG from the edge detection of WLI surface profiling. The pixelation resulting from the limits of the WLI method are shown in the raw data alongside the mean and third-order polynomial fit to the mean width dataset.

5.4.1 1560 nm waveguide model verification

The WLI/ED method can also be applied to a similarly fabricated PPLN waveguide for 1560-780 nm SHG which has been verified to have a phasematching spectrum which immensely deviates from the analytical $\mathrm{sinc}^2(x)$ function for an ideal waveguide. The chosen waveguide, from sample C156 set 3, was designed and fabricated in an adjacent project led by Dr. Lewis Carpenter and Dr. Sam Berry [103, 10, 4] and they kindly provided this sample for investigation here. This waveguide has the phasematching curve presented in figure 5.14. It should be noted this optical charaterisation corresponded to a maximum SHG power generation when choosing the launch conditions. This waveguide was characterised using a seeded EDFA and optically launched using a similar system to that presented in figure 4.13. The nonlinear optical conversion was performed at low optical powers to operate within the small conversion regime. The waveguide was determined to be multimodal in the x-axis (horizontal) and the effect associated with optical launching conditions will be discussed later.

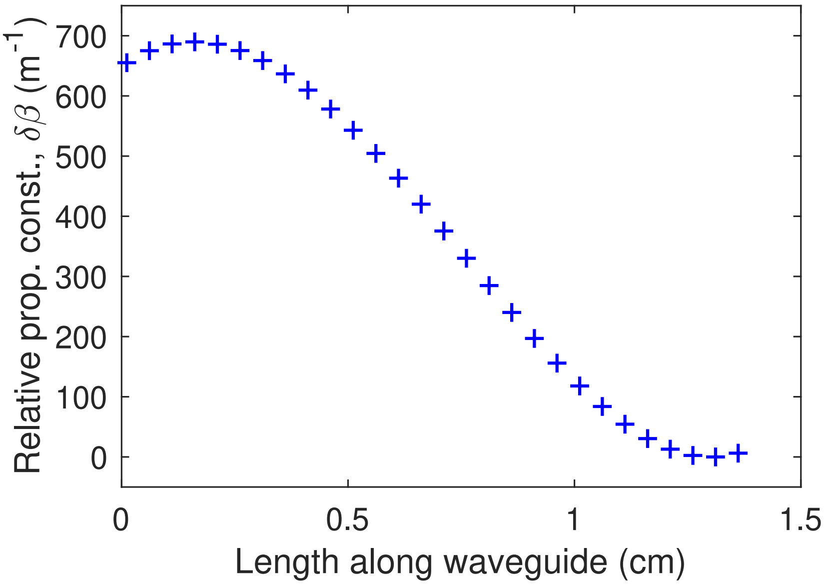

FIGURE 5.11: Deviation away from the ideal, uniform case for the waveguide used in this work. This curve results from the relation of width to propagation constant to propagation constant from a numerical mode solver and the experimentally ascertained waveguide width.

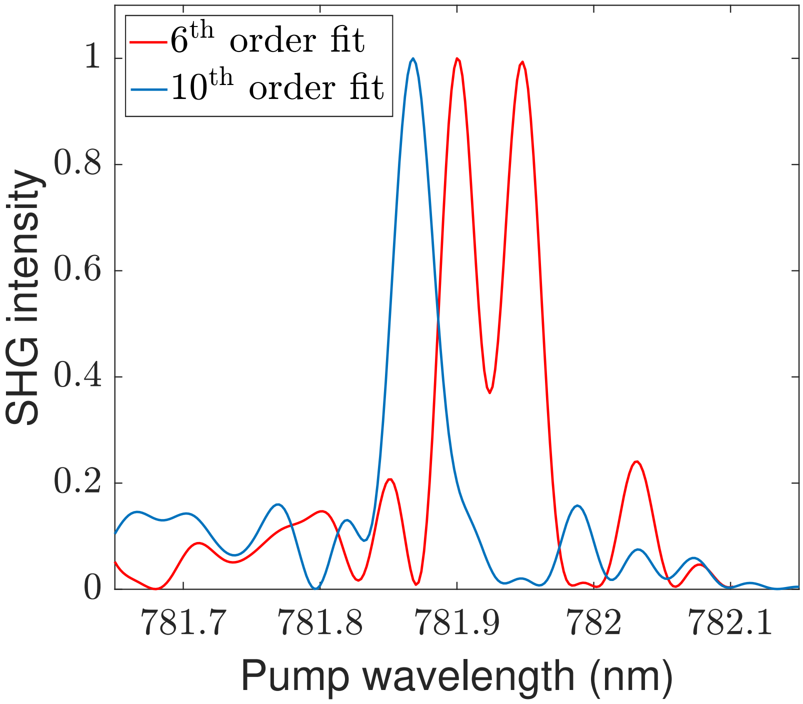

FIGURE 5.12: Higher order fits for the phasematching spectrum of the wavegudie width data from WLI characterisation. Spectra are seen to be highly different instead of converging towards the experimental data, indicating that over-constraining the fit is not an accurate representation of the fabricated waveguide.

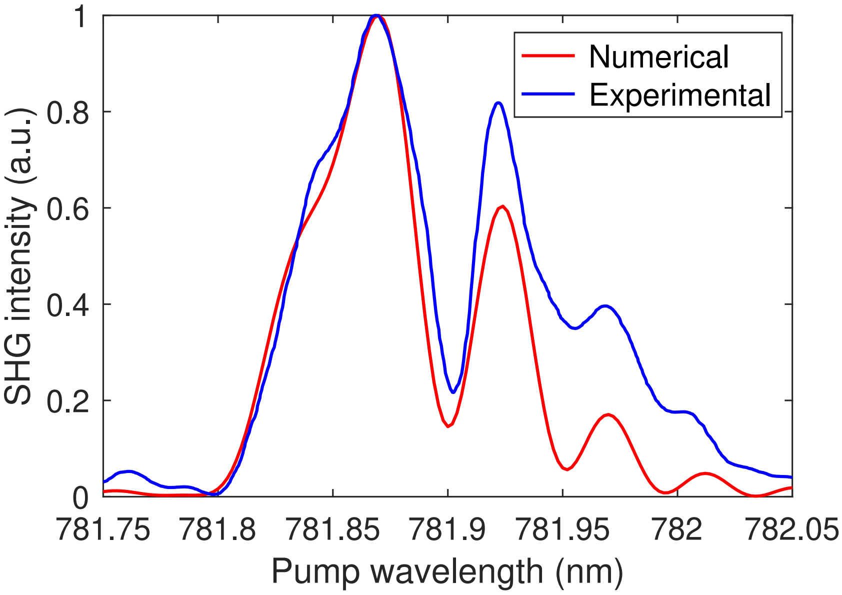

FIGURE 5.13: Comparison of numerical data versus experimental data following the image recognition method for waveguide width characterisation and the normalised optical phasematching spectrum. Similarities are observed with regards to the period of fringes and the lack of symmetry around the peak of highest conversion efficiency.

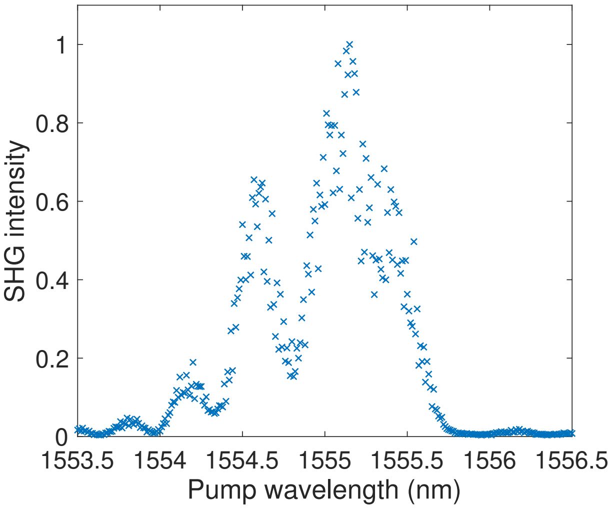

FIGURE 5.14: Experimental phasematching spectrum associated to the 1560-780 nm, zinc-indiffused PPLN ridge waveguide used in this work.

The methodology and data analysis route chosen to produce the resulting data has been thoroughly discussed in the preceding section and so the results will be presented without repetition of the procedure, except for where it may deviate. The numerical model created in Fimmwave, and shown in figure 5.7(a) is identical with the exception of the width, as will be presented. For the range given, effective index as a function of waveguide ridge width was determined to be

$$n_{\text{eff}} = -2.09086 \times 10^{-5}x^2 + 7.12772 \times 10^{-4}x + 2.12478 \tag{5.3}$$

established from a quadratic fit to the experimental ridge width data. The ridge width values of this waveguide, figure 5.15(b), can be seen to quite varied but, qualitatively, it is primarily noise as opposed to the definite features observed for the waveguide used previously, figure 5.10. Applying a simple third-order polynomial fit to the ridge width data calculated for this particular waveguide yielded the following relation in micron,

$$width(x) = -2315.91x^3 + 300.007x^2 - 12.8702x + 15.4025. \tag{5.4}$$

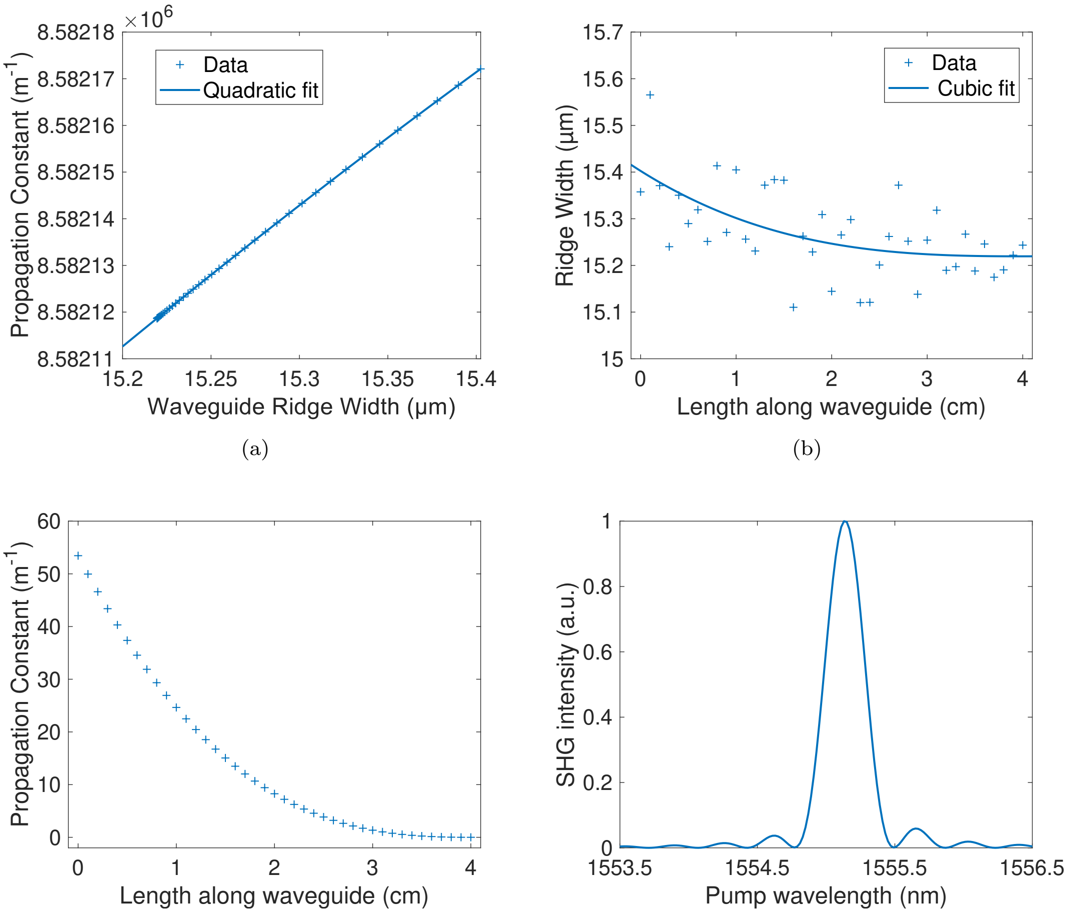

(a)

(b)

(c)

(d)

FIGURE 5.15: (a) Relationship between a zinc indiffused PPLN ridge waveguide and its corresponding propagation constant from the numerical model. The quadratic fit is shown for application in using this function for any other arbitrary waveguide width experimentally determined. (b) Measured width profile for the 1560-780 nm waveguide used in this work and (c) the corresponding propagation constant profile of this waveguide for application into the three-photon ODEs. (d) Resulting numerical model of the phasematching spectrum for the measured propagation constant profile.

Using this as the starting point for modelling the theoretical phasematching curve for this waveguide, we can see very little deviation from the idealistic sinc^2, as seen in figure 2.7(b). This was expected as the relative propagation constant offset function imposed on the phasematching condition in the ODEs governing this process, figure 5.15(c), is quite minimal. The majority of mean waveguide widths fall within a standard deviation of the widths calculated within an image equivalent to figure 5.9 for this waveguide. Hence, it can be concluded that the dicing process for this waveguide was precise to within the resolution of the WLI and fabrication process was the cause of the distorted phasematching spectrum. This particular sample was fabricated early in the process development in a furnace which was later confirmed to have poor thermal uniformity and the phasematching spectrum is assumed to be the result of diffusion non-uniformity, which is not as readily measured. The WLI/ED method has essentially enabled a quick confirmation that the waveguide fabrication process for these 1560 nm frequency-doubling devices is not limited by the dicing fabrication step and may have been a quicker troubleshooting process than that which was undertaken to conclude the furnace was unsuitable for this purpose.

Due to the multimoded nature of this waveguide, it was also of interest to confirm whether there was any interference in this characterisation being introduced from the capability of other waveguide modes to phasematch. To determine whether or not this was to be considered, the optical launch could be modified not to maximise the conversion efficiency, but to maximise the power in the first-order SHG mode. In practice, this is quite simple. Launching more optical power into a location which provides a higher overlap integral with the first-order ~780 nm mode in this waveguide and appropriately tuning the wavelength of the seed laser can generate an SHG mode which was not seen with as high efficiency in the optimal launch position. The next higher order mode was established to phasematch at approximately 1562 nm, figure 5.16(a), sufficiently far away from the fundamental-mode phasematching to not contribute to the form of the spectra. Additionally, the launch condition to satisfy this phasematching condition was sensitive enough to completely extinguish the generation occurring at 1562 nm, as seen in figure 5.16(b), which was the result of an offset in the y-axis when coupling light into this waveguide. This short investigation ruled out the potential for interference of waveguide modes causing the resulting phasematching spectrum to allow for a definitive conclusion it was the result of the diffusion process in this instance.

5.5 Conclusions

A method for investigating fabrication flaws in ridge waveguides has been presented and discussed regarding its application in nonlinear optics. The application is primarily seen for the early stages of ridge waveguides, regardless of whether that will be in a PPLN or PPKTP waveguide. Once a dispersion curve can be obtained and verified in a simpler case to be accurate, the qualitative troubleshooting method presented will enable researchers to quickly distinguish between process flaws. Further verification of

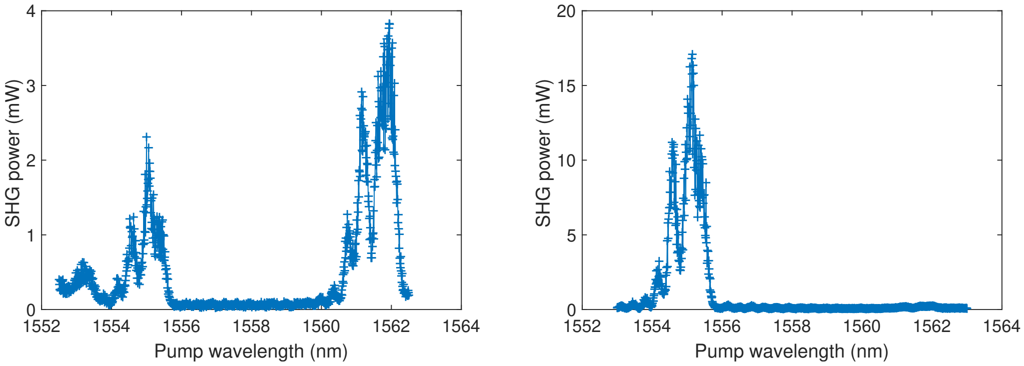

(a) (b)

Figure 5.16: (a) Phasematching spectrum of the waveguide designed for 1560-780 nm SHG where the optical coupling has been positionally altered to excited phasematching of higher order modes which occur at longer wavelengths. (b) Broader wavelength range of the phasematching spectrum when the launch is optimised for maximum pump throughput. Notice the higher order mode is completely diminished.

this method would require a more collaborative effort. For example, by utilising parts of the presented work for a nonlinear waveguide geometry fabricated by other research groups or, naturally, to use a PPKTP waveguide with a relatively well-known dispersion curve.

Future prospects to accurately simulate experimental phasematching results are seen to lie in developing dispersion curves for the generated signal wavelength. This is challenging as it would need to be guaranteed that the correct mode was simulated and selected from the waveguide mode solver software when the waveguides are multimode at the signal wavelength. This is expected to be challenging but not impossible. There may be an argument to say a full experimental-comparison numerical tool should incorporate imperfections in the ferroelectric poling, however, this would reduce the purpose of methodology presented in this chapter as it moves away from a straightforward characterisation tool. The sole purpose of its development and investigation was to find a method more simple than anything available in literature as to actually be useful to researchers developing similar technologies where time consumption is a relevant factor.

Nevertheless, the work presented here has provided interesting results but its main purpose was to persuade the nonlinear waveguide community that measurements such as this are achievable with the use of modern characterisation equipment. Hopefully, there will be a reduction the assumptions taken regarding the waveguide nonuniformity in waveguide fabrication literature.

Chapter 6

High-speed upconversion detection of mid-infrared radiation

6.1 Introduction

Although a vast amount of current telecommunications research is focussing on high data transmission rates typically through pioneering optical fibre technologies [151, 152, 153], development of free space optical (FSO) communication technologies remains an attractive route for communicating with unmanned aerial vehicles, high altitude platforms and satellites. This is alongside the abundance of bandwidth generated from multiplexing technologies [154, 155, 156]; recent review papers on the general topic of free-space communications can be found in Son and Mao [157] and Willner *et al.* [158]. The accepted atmospheric transmission bands are 3-5 µm and 8-12 µm. Given the transmission range of LN, the shorter-wave band for atmospheric transmission is more readily accessed. As a result of this, there have been recent demonstrations of mid-infrared (MIR) data transmission with upconversion to the telecommunications C-band for amplification of the signal via an erbium-doped fibre amplifier (EDFA) [159]. This work was an ideal use of high-quality C-band equipment. However, the advancements of silicon-based detectors with single-photon-level sensitivities and their reduced dimensions provides an opportunity to investigate a system in which the receiver detects in the widely used Si absorption band. This has the potential to result in a system with reduced device footprint and increased measurement sensitivity. Upconversion detection is establishing itself as a broad area of research due to the plethora of applications requiring working in the MIR radiation band. For example, upconversion detection has proven to be advantageous over conventional detectors in the near-IR region for methane detection [14], alongside imaging capabilities of thermal radiation sources. In this chapter, I target an application utilising 1550 nm and 1064 nm as well-established laser sources as these wavelengths are easily accessible and do not require custom-built system components. Nonlinear optical conversion processes are performed without cavity enhancement. The widely tuneable EDFA band would also allow a user to define a MIR transmission wavelength to avoid the narrow spectral absorption lines in the region of the generated MIR signal.

The optical setup which will be discussed and built as part of this chapter will be the building block of a new path of research at Southampton. Motivation, optical design and characterisation will of key interest, as is such is the development of any new branch of research. With prior explanations of nonlinear optical process, found in Chapter 2 and additionally in references provided therein, knowledge of this shall be assumed. This chapter will be self-contained with regard to prior art for MIR generation, detection and use in communications.

6.1.1 Mid-IR detectors

Thermal detectors provide users with a route for detecting high power laser beams due to their high damage thresholds. Additionally, the choice of absorption material, potentially anodized aluminium, has a broad absorption spectrum. This means a single detector can be comparatively cheap and applicable from UV detection to far-IR. However, they rely on the measurement of a change in temperature of the thermometer section of the detector which needs to come to thermal equilibrium to balance the incoming radiation and thermal conductance of the absorption material. This process is inherently slow as it relies on the diffusion process defined by Fourier's law. It is apparent that this operational principle is not suited to communications for data rates above the kHz region. In the thermal technologies, thermopiles consist of arrays of thermocouple typically behind a light-absorbing material. The thermoelectric effect, of which is the operational principle of a thermocouple, is amplified to measurable potential difference values due to the in-series arrays of thermocouples. These provide similarly broad absorption windows with a response time on the order of 10's of milliseconds [160].

Cryogenically cooled semi-conductor detectors are considered the next viable option, mercury cadmium telluride (HgCdTe) or indium antimonide (InSb), which fall into the category of photovoltaics. Potentially having preferable noise characteristics in comparison to the other detector types mentioned, the requirement for cooling by way of liquid nitrogen being in constant contact limits their suitability for applications where the receiver components are airborne or lack convenient access for replenishment. Hence, the search continues for technologies which can avail of the high-speed silicon or InGaAs detectors which are already deployed in telecommunication system at any given optical wavelength. Further details on the principles of infrared detectors can be found in [161]. However, in the context of this thesis, the obvious choice is using nonlinear optical crystals to frequency convert into the absorption region of the established, high-speed detectors, i.e., upconversion detection.

6.1.2 Prior art of upconversion detection

A vast amount of research has been undertaken in the MIR range, using some degree of nonlinear conversion elements, that it is now impossible to exhaustively cover it. Instead, a spread of the research topics shall be discussed to draw attention to the usefulness of the research area. Communications via upconversion detection (UCD) shall be discussed in depth in section 6.2 for the limited literature broaching this topic.

Hu *et al* [162] presented a spectrometer utilising an intracavity PPLN crystal in a unidirectional Nd:YVO$_4$ cavity. The substantial 1064 nm power ensures the high conversion efficiency of introduced MIR photons. These photons are inserted into the cavity from a butane burner. SFG occuring within the cavity and some additional filtering optics, including a Fabry-Perot filter for enhancing spectral resolution. Hu *et al.* verifies the system is capable of detecting water vapour, in comparison to gas spectral databases. An image is registered on a silicon CCD. Interference fringes are formed via the angular spread of the incoming MIR beam and the FP filter.

Continuing in the realm of spectroscopy of hydrocarbons, Wolf *et al.* [14] demonstrated a record breaking self-gated system in which they generate and detect a pulsed MIR signal to study their ability to resolve low concentrations of the gas. A delay line allowed for synchronisation of the generated pulses and another 1064 nm pump beam for suppression of background noise. Hence, they prove a concentration resolution of 1.5 ppm·m, where resolution limits closer to ~10 ppm are considered standard in methane sensing [163]. The subtle difference in units is due to the path length of the gas cell being accounted for. The 25 cm cell means the upconversion system presented by Wolf is a competitive technology.

Widarsson *et al.* [164] has recently demonstrated a single-photon counting LIDAR scheme to demonstrate the spatial resolution possible from a pulsed MIR source, using simple microscope slides as a replacement for any object which exhibits a small reflection. The authors establish a spatial resolution of a few millimetres can be achieved using their technique.

Other works in this area include MIR single photon detection [165, 166], studying the effects of thermal noise in broadband conversion systems [167], imaging [168], and further examples of UCD for LIDAR applications [169]. While these applications are expansive, their commonality is the desire to use visible (Si) or NIR (InGaAs) detectors which can, with careful experimental design, provide the potential for low noise signal detection. It should be evident now, in addition to acknowledging the atmospheric absorption spectrum, that there is an obvious progression into telecommunications using MIR signals.

6.2 Mid-IR and frequency conversion for communication applications

For a system which inherently requires two laser sources for either a DFG or SFG process, I choose to experiment with 1064 nm and ~1560 nm sources on the basis these are commercially viable laser sources with good reliability and typically accessible due to the invention of the Nd:YAG laser which has been miniaturised and vastly cost reduced over time. Lasers in the C-band (1530 to 1565 nm) are used for standard telecommunications and hence, good quality and widely accessible optical components have been developed. This includes the EDFA for achieving higher powers and the waveguide development to fabricate high-speed LN electro-optic modulators (EOM).

Hence, it is relatively clear that nonlinear conversion is a competitive option to realise MIR communications (among other applications) when the technological advantages of using C-band telecommunication equipment (laser sources, modulators etc.) and the challenges with current MIR detectors are considered. In fact, it is so highly desirable to use telecommunications standard C-band components that under-sea communications research which transfers data in the blue-green wavelength band, uses third harmonic generation (THG) to generate blue-green from a 1560 nm source [170] which would be an inherently inefficient nonlinear process; requiring SHG initially and followed by SFG of the SHG wavelength and the C-band pump source. However, the authors achieve high conversion efficiencies due to the high peak powers used.

The most relevant work to the body of work presented in this thesis is described by Su *et al.* [159]. The authors designed and built a custom-made EDFA which was seeded with a commercial C-band laser and two ytterbium doped fibre amplifier (YDFA) seeded with a 1083 nm laser as the pump source prior to frequency conversion. The separate YDFAs are used to seed the generation of the MIR beam and also the upconversion back to the C-band for detection, both stages using DFG as the nonlinear process with the transmitter system using a high-power beam combiner and broadband half-waveplate prior to the PPLN crystal. The receiver also utilises a PPLN crystal. This system design is entirely reasonable as it enables a further EDFA to amplify the weak 1550 nm signal created for detection after MIR transmission. They achieve a MIR power of ~4 mW with 2 W and 5.5 W of 1550 nm 1083 nm power, respectively. They achieve a bit error ratio (BER) in the ON-OFF keying modulation scheme better than 10^{-9}. While there are many differences in this work, these figures provide the benchmark for a system with a similar application.

6.3 Brief introduction to bit error probability

While this is not a dedicated thesis in the area of telecommunications, an explanation of future results is required for completeness. Prior knowledge of jargon in this ever-expanding field of research/industry will not be expected and avoided as best as possible in this brief section. Bit error ratio is the industry standard for characterisation of a telecommunications system as it is a very simple concept; the number of errors in the reading of a bit per the total number of bits transmitted over a period of time. It is a unitless parameter. In optical communications, the probability of a bit error occurring is typically related to a relevant parameter by the error function

$$f(Q) = \frac{1}{2}\,\mathrm{erfc}\left(\frac{Q}{\sqrt{2}}\right), \tag{6.1}$$

where Q is referred to as a representation of a digital signal-to-noise ratio (SNR). While the difference is subtle, the bit error probability and BER differ as one is the theoretical expectation and the other is the experimentally measured equivalent. I shall use the terms interchangeably while attempting to be consistent with the literature. The standard method for visualising quality of data transfer through a system is to plot the eye diagram, appropriately named as it has visual similarities to an open human eye. It is generated by superimposing segments of the bit stream over a period of time and correctly aligning the phase of the segments. Q can now be defined as

$$Q = \frac{V(x=1) - V(=0)}{\sigma(x=1) + \sigma(x=0)}. \tag{6.2}$$

where x represents the sequence of bits, $V(x = 1)$ and $V(x = 0)$ respectively are the voltage levels of the upper and lower parts of the eye and σ is the corresponding standard deviation of the respective sections of the eye diagram. This relation of the parameter Q to the bit error probability can be seen visually in figure 6.1.

An important characterising parameter when designing and testing new data transmission schemes is the back-to-back measurement. This parameter is essentially the comparison of BER between connecting the modulated signal directly after generation to the detector and by-passing whatever new transmission system is being tested. This is typically quoted as a power penalty figure (the increase in signal power required to restore the Q parameter to that if the new optical system was disregarded). Notwithstanding, this defining parameter will not feature in this work as the original optical signal is not within the absorption band of the silicon detector which will be used in this work.

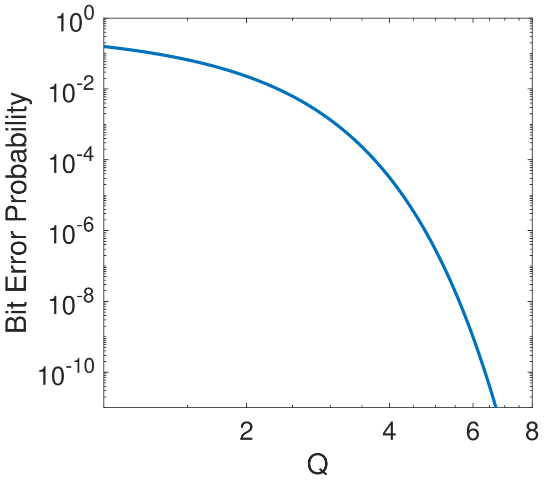

FIGURE 6.1: The relation that the SNR-type parameter Q has on the probability of incorrectly reading a data bit.

6.4 Laser noise

6.4.1 Relative intensity noise

It is commonly accepted that there exists a number of physical processes which contribute to the noise, at a certain frequency, which is present in a laser. As occurs in almost all electronics, $1/f$ is a distinct feature at low frequencies and the physical process for this is not well understood but is accepted to exist. Further sources of noise include thermal, shot, intrinsic laser dynamics etc. I will briefly elaborate on these points for clarity in what exactly is measured in the presented work here but further details can be found in Refs. [171, 172, 173]. Formally, the intensity of a laser is described as a time dependent term,

$$P(t) = \overline{P} + \Delta P(t), \tag{6.3}$$

where relative intensity noise (RIN) is defined as

$$RIN = \frac{\langle \Delta P(t)^2 \rangle}{P_0^2}. \tag{6.4}$$

It should be noted that the experimentally measured quantity is the power spectral density (PSD) of the noise source and RIN is strictly related to the integral of this parameter. RIN is a useful parameter when comparing many lasers or developing new laser sources and investigating the optimal current to drive them at, for example, for low noise operation but it is not the parameter which will be used here as I am primarily using this as part of a qualitative investigation. Nevertheless, it is the origins of $\Delta P(t)$ which can now be briefly discussed.

6.4.2 Thermal Noise

Johnson-Nyquist noise is also known as thermal noise due to its physical origin which was first discovered and explained in simple electrically conducting media [174, 175]. It essentially arises due to a Brownian motion-like of particles in a material having non-zero electrical resistance at temperatures above absolute zero. It can be measured on a simple resistor with very careful experimental conditions and optimum choice of amplifiers and is defined as

$$Noise[dBm] = 10log_{10}\left(\frac{4k_BTR\Delta f}{1\times 10^{-3}}\right) \tag{6.5}$$

where T is temperature of resistor, k_B is Boltzmann's constant, R is resistance value and Δf is the frequency bandwidth of the measurement, denoted as resolution bandwidth (RBW) when configuring spectrum analysers to perform a noise measurement. Division by 1 $\times 10^{-3}$ is to convert from dB to dBm. In the development of new lasers or new electrical devices, thermal noise would need to be measured and accounted for. However, this is not explicitly necessary when comparing commercial lasers and investigating nonlinear phenomena, as is carried out in this work. It is simply noted that this is not subtracted from any spectra presented in this thesis.

6.4.3 Shot noise

Shot noise is the phenomenon which occurs due to the quantisation of electric fields, in contrast to the early belief where it was assumed to be the quantisation of charge. This quantisation presents itself as a noise source because of the Poissonian distribution of arrival times for the quanta [176], whether that is photons or electrons. As an aside, it is worth noting the importance of electrical current in optical measurements in contrast to purely electronic systems in which voltage tends to be the defining parameter. This is because optical power is linearly proportional to the current generated from a photodiode as each single photon has the ability to create a single excitation in the semiconductor device; leading to the early misinterpretation that is was a phenomena related purely to electrons. Shot noise current density is defined as

$$i = \sqrt{2eI_{\mathrm{DC}}} \qquad [\mathrm{A}/\sqrt{\mathrm{Hz}}] \tag{6.6}$$

where e is the charge of an electron and I_{DC} is the steady-state current [177]. However, as the electrical power is proportional to the square of the current, the shot noise to be considered is

$$shotnoise \propto 2eI_{DC} \tag{6.7}$$

and hence

$$N_{shot} = \frac{2e}{I_{DC}} \qquad [\mathrm{dBc}]. \tag{6.8}$$

For a relation containing optical power, as this is preferential to work with experimentally, electrical current is easily substituted to present shot noise as

$$N_{shot} = \frac{2hf}{P_o}. \tag{6.9}$$

A further note to conclude from this is the inverse relation of shot noise to the electrical current generated, related to the responsivity of the detector. Hence indicating this noise level will increase at a noise frequency which has a lower respsonsivity for a given detector. This should be considered if one wants to compare a laser's noise profile to the shot limit, as will be discussed later.

6.4.4 Relative intensity noise and its role in telecommunications

The role of relative intensity noise in optical communication systems is considered to present itself as a power penalty to restore the BER value to the ideal[178]. Essentially, this means the voltage separation, $V(x = 1) - V(= 0)$, needs to increase. While practically this power penalty will represent a requirement to increase the laser power or EDFA gain, dependent on which is more suitable for the hypothetical system. Formally, the discussion of RIN in optical communication systems is considered in the carrier-to-noise (C/N) ratio, defined as [179]

$$C/N = -\mathrm{RIN} - 10\log(\mathrm{BW}) + 20\log\left(\frac{m}{\sqrt{2}}\right) \tag{6.10}$$

where BW is the noise bandwidth of the receiver and m is the peak modulation. Hence, it is straightforward to recognise the RIN of a laser needs to be minimized to ensure the optimal transmission of telecommunications data.

6.4.5 Experimental methodology

While a vast amount of literature presents data resulting from noise measurements of lasers [19, 180, 181], the methodology is not always clearly presented with regards to chosen units to represent data or the analysis of data. The study of the vast amount of techniques with subtle mathematical differences is outside of the scope of this work and I choose to proceed with a methodology which has been logically presented and applicable with modern high-speed, integrated detectors available in this work. The rigorous study was carried out by Tawfieq *et al.* [182] and initially set out to determine the applicability in replacing the green lasers used for pumping Ti:Sapph lasers with a cascaded PPLN configuration with a tapered diode as the IR source. For their system, they discovered an increase in the power spectral density (PSD) for the SHG beam which had been generated through the two PPLN crystals in comparison to the IR light used to generate it. Additionally, the generated beam was not shot noise limited but at low frequencies the SHG signal did not demonstrate any increase in PSD after being passed through a second PPLN crystal. The authors do not propose a physical mechanism for this although it may simply be due to the coherence of the SHG beams; where at higher frequencies there are additional dynamics which are unclear.

Tawfieq *et al.* presents a well-known method for calculating the PSD of a laser source

$$S_p(f)[\mathrm{dBc/Hz}] = S_p(f)[\mathrm{dBm/Hz}] - 10\log_{10}\left(\frac{V^2}{R_S G}\right) \tag{6.11}$$

where $S_p(f)[\mathrm{dBm}]$ is the PSD which is gathered from a radio frequency spectrum analyser (RFSA) and post processed for conversion into units of dBm/Hz. The division is carried out in the linear domain and this division value is set by the RBW of the instrument. Further information on how an RFSA operates can be found in the following sources [183, 177]. Due to our choice of detectors, the DC component of the laser source after detection is accessible where Tawfieq *et al.* calculated this value based on the responsivity of the photodiode used. Hence, equation 6.11 is slightly modified from that which was presented in previous work to account for the ratio of signal gain between the AC and DC output ports of the photodiode due to the internal bias-tee used to split these components of the incoming electrical signal. Figure 6.2 portrays a simplified schematic of the difference between the common electrical configuration used and the setup used in this work to summarise the aforementioned points.

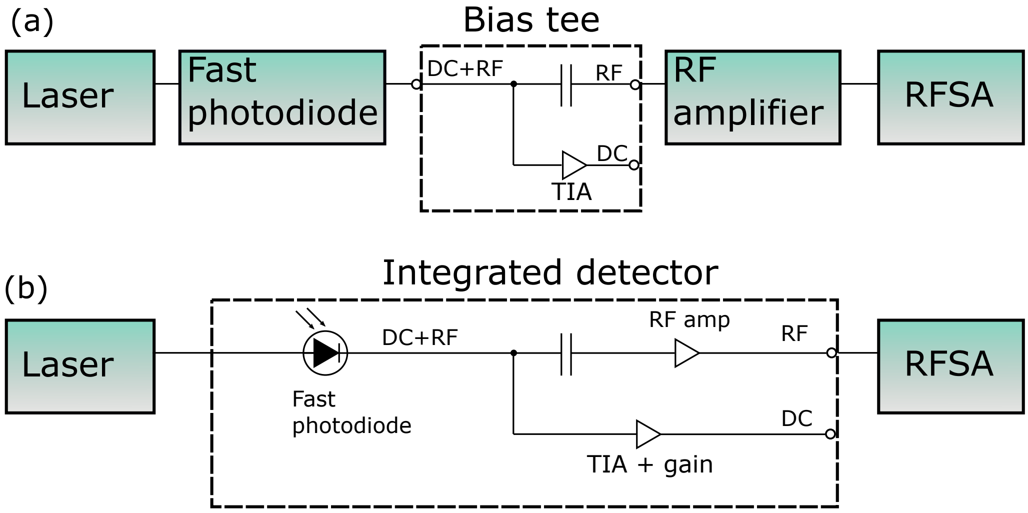

FIGURE 6.2: Subtle difference in experimental measurements of laser noise due to the availability of high-speed detectors with similar specifications to cover the wavelength range required.(a) A typical experimental configuration to measure laser noise when calibration of each component is required for absolute noise measurements and (b), the configuration used in this work to obtain amplitude noise PSD of various wavelength sources.

6.5 Optical design and Characterisation

To build a MIR transceiver and receiver, an optical configuration for the DFG and SFG process will need to be designed and built, respectively. This section shall comprise of the optical characterisation of both segments of this system. Schematically, the position and functionality that is required of the nonlinear crystals is presented figure 6.3. As previously indicated in section 6.1, I investigated the use of 1064 nm and ~1550 nm laser sources due their broad, commercial availability.

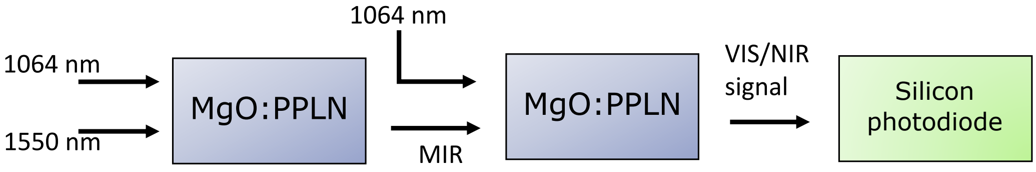

FIGURE 6.3: High-level schematic for upconversion detection using two MgO:PPLN crystals which are used for the generation and detection of MIR radiation through the DFG and SFG $\chi^{(2)}$ parametric processes, respectively.

In the presented set-up, the residual 1064 nm pump is re-used as a method to reduce experimental complexity and cost of this system. To enable communications, the transmitter will generate the 3.4 µm radiation with a pseudo-random bit stream (PRBS) superimposed in an amplitude modulation format, typically referred to as on-off keying (OOK). A fibre laser will be used as the 1064 nm source due to their excellent mode profiles; consideration of the beam shape is not required as such when using asymmetric diode-laser outputs [184]. The details regarding the optical system and characterisation of this system will be presented in the following sections; the transmitter (DFG) will be presented in section 6.5.1 and the receiver (SFG) in section 6.5.2. Additionally, the specific MgO:PPLN crystals which enabled the nonlinear optical processes to be discussed are shown in table 6.1. A labelled photograph of this system can be seen in figure 6.4.

TABLE 6.1: MgO:PPLN crystals used in this chapter.

Process/stage	Λ range (µm)	Λ used (µm)	Length (mm)
DFG/transmitter	29.52 - 31.59	30.49	40
SFG/receiver	20.90 - 23.30	22.4	40

6.5.1 Mid-IR Generation via DFG

Figures 6.6(a) and 6.6(b) are the numerical design of the focussing optics for the beam waists of the 1064 nm and 1550 nm input lasers. Both are calculated via the ABCD matrix method described in section 2.4.1. The obvious differences in initial parameter set-up is the 1550 nm source is a single-mode fibre output and hence diverges immediately

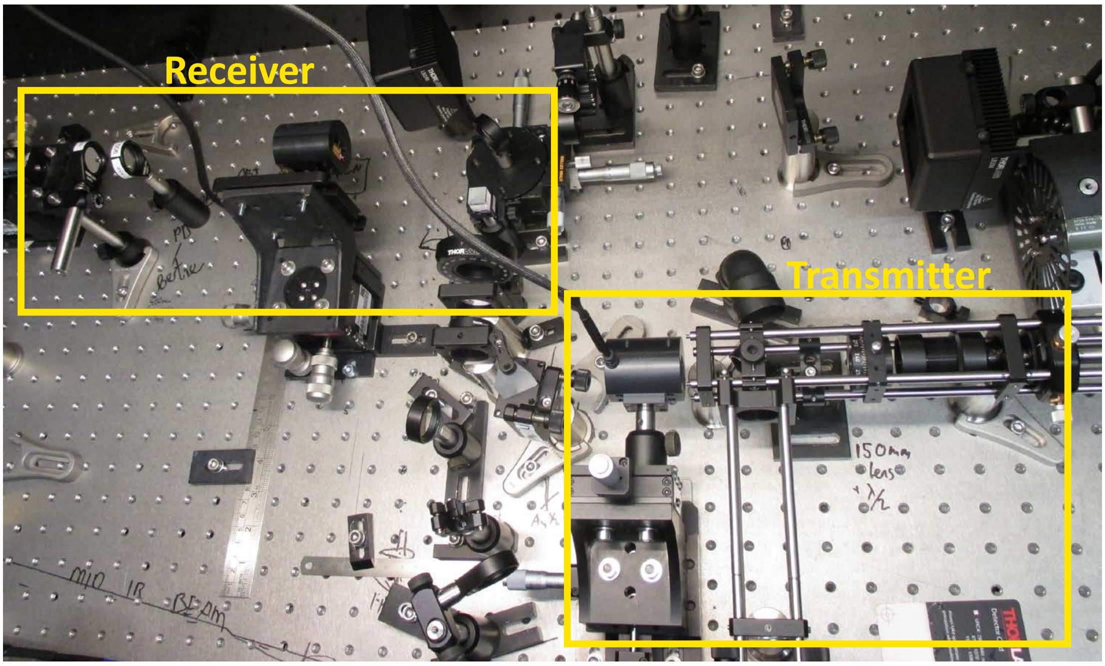

FIGURE 6.4: Photograph of the optical setup described in this work, as schematically shown in figures 6.5 and 6.9.

whereas the the commercial 1064 nm source is a fibre laser which is collimated. The starting beam diameter of the optical fibre mode is assumed to be 8.2 µm, equal to that of SMF-28, as supplied by the manufacturer of the EDFA which will be used. The initial collimated diameter of the 1064 nm beam is 1.8 mm. As portrayed in figures 6.6(a) and 6.6(b), the beam waists are designed to be 69 µm and 56 µm, corresponding to Rayleigh ranges of approximately 19.98 mm and 20.66 mm for the 1550 nm and 1064 nm beams respectively. This was implemented using 20 mm and 150 mm focal length lenses, respectively, which are readily available specifications commercially. Thence, the confocal parameter is approximately equal to the crystal length used here, providing a sufficient point to begin the alignment process to obtain a sufficient amount of generated optical power for detection and further conversion. The dichroic mirror (DM) is not accounted for in the numerical design as the experimental alignment procedure would compensate for this assumption.

These details are realised experimentally using AR coated lenses for each given wavelength. The DM (Thorlabs DMSP1180) is a short pass mirror with a cut off at 1180 nm to enable the combination of the 1064 nm and 1550 nm beams; to be mixed in the PPLN_{DFG} crystal. A half-wave plate is also present in the 1064 nm beam path prior to beam combination to align the linear polarisation along the z-axis of the PPLN crystal. The fibre laser output was not rotated as the particular version used had an armoured cable. The 1550 nm laser output fibre was rotated to align the beam's polarisation accordingly. Initial alignment is carried out using a cryogenic indium antimonide (InSb) detector to detect the generated 3.4 µm. This was placed after the PPLN crystal, prior to the prism for beam separation. A germanium window (WG91050-C9, Thorlabs) is placed in the beam path to optically filter out the shorter wavelengths for detection of the MIR signal. Following this filter, an optical chopper is also placed in the beam path to enable lock-in amplification detection of the generated MIR beam. This was a practically convenient method for initial alignment as thermal detectors are too slow and also do not have the signal-to-noise ratio to reliably perform this alignment procedure, which may only produce micro-watts of power, at first. This is required as background MIR radiation sources are simply too great an influence on a thermal power reading. The most influential and problematic source of radiation is, quite frankly, the user performing the alignment task. Hence, detecting a specific frequency associated to the optical chopping is preferable. Power loss of the MIR beam is the most critical parameter when choosing optical components for this setup up post the 3.4 µm generation. Ideally, all mirrors would be MIR-enhanced gold (a proprietary Thorlabs product). However, the absorption of gold is substantially high enough for the 1064 nm beam to damage the mirror if gold was placed following the CaF_2 prism, figure 6.5, and so a silver-coated mirror is used. The 1064 nm is then picked off using a D-shaped dielectric mirror (BBD05-E03, Thorlabs) and collimated using a 300 mm lens. The MIR beam is approximately collimated using a 250 mm focal length, CaF_2 lens for direction towards the receiver/SFG stage, discussed in section 6.5.2.

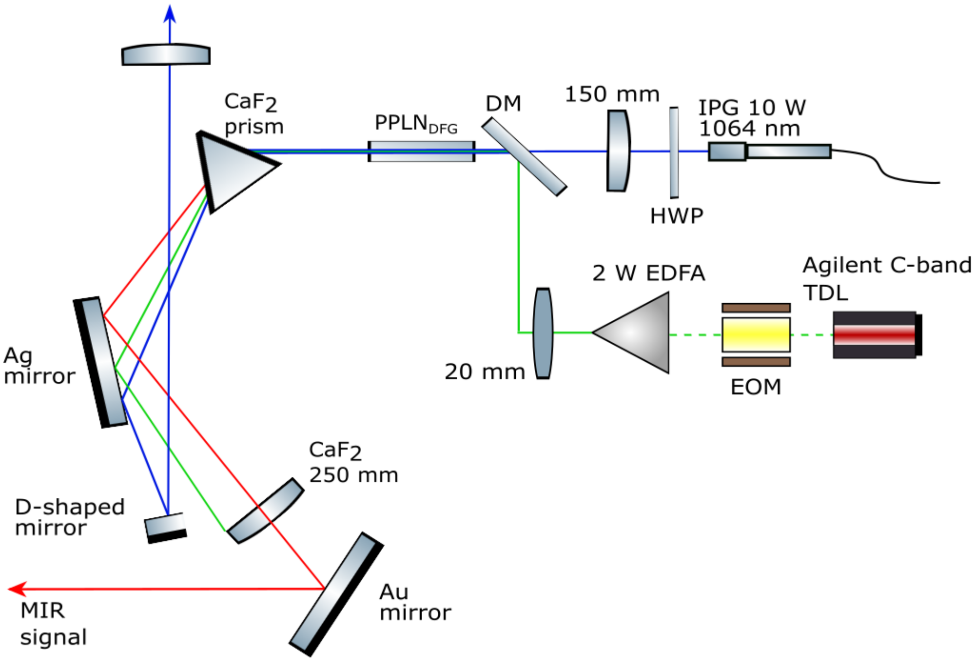

Figure 6.5: Generation of modulated MIR beam through DFG. This is represents the transmitter stage of this optical setup. The dashed line indicates the optical fibre portion of the 1550 nm beam. Solid lines represent free-space beams.

The data presented in figure 6.8 was recorded on a thermal power meter (S302C, Thorlabs) with a broadband, AR-coated Ge window to filter any residual 1550 nm signal in the beam path. The data is recorded following the gold, MIR enhanced mirror in

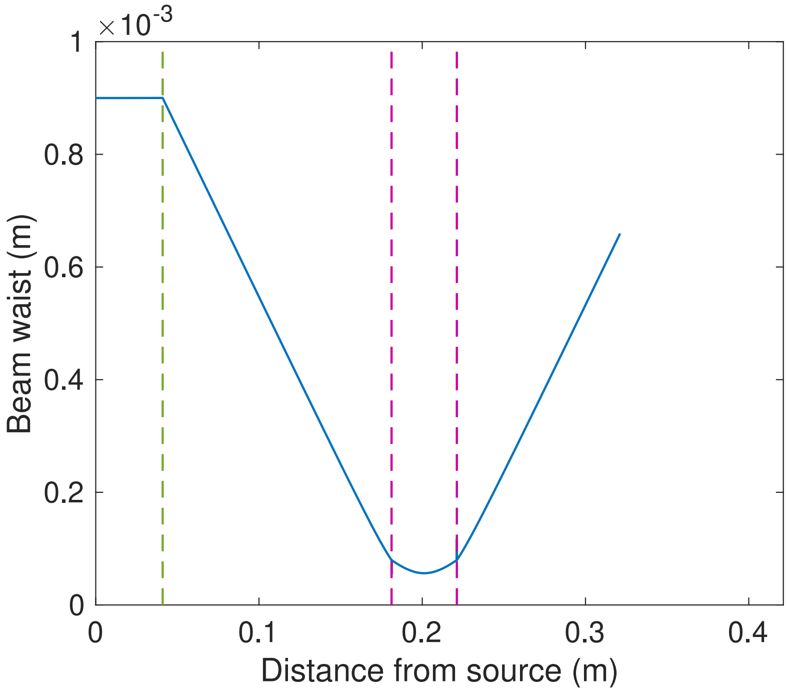

(a)

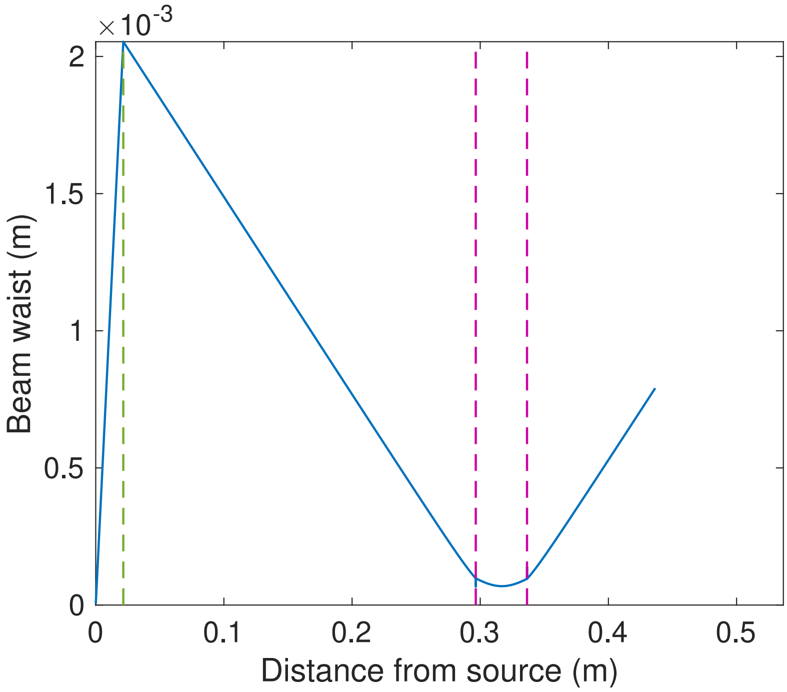

(b)

FIGURE 6.6: (a) Design of beam focussing parameters for the 1064 nm fibre laser source ; (b); Single-lens beam design from the single-mode fibre output of the 1550 nm laser source. The green dashed line indicates a lens and the pair of dashed magenta lines are the PPLN facets.

figure 6.5, to account for any inherent loss occurring on the previous optics following generation. The absorption of this Ge window at ~3.4 µm has been accounted for in

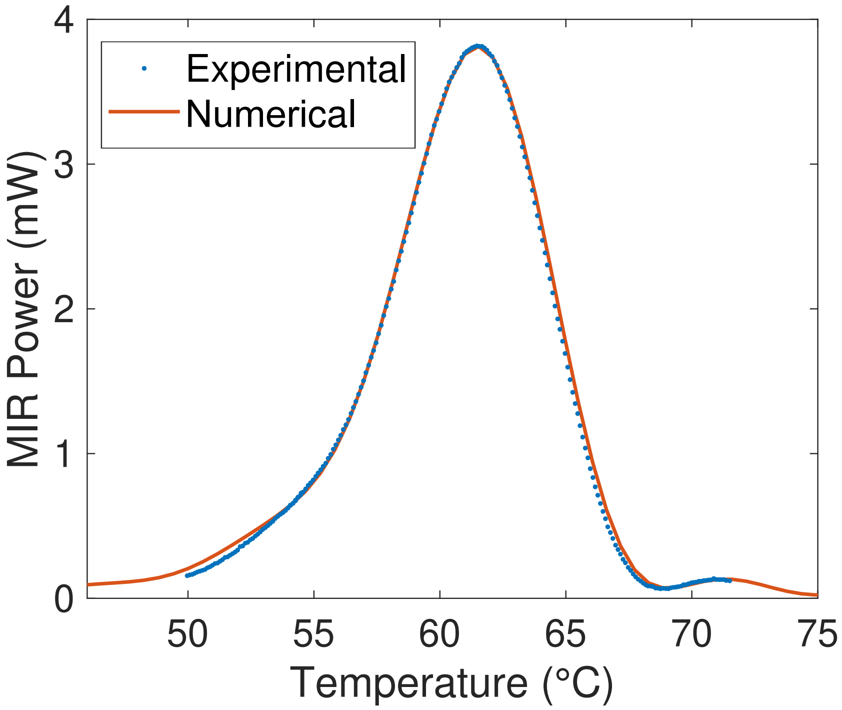

Figure 6.7: Phasematching curve as a function of temperature for the first PPLN crystal in this upconversion detection system for DFG of the pump and 1550 nm signal beams. This data represents the phasematching spectrum with the input optical powers set below their maximum output powers. Numerical curve represents the phasematching curve as a result of a focussed beam interaction, generated using the commercial software SNLO and discussed in the main text.

the presented data. The generated power is expected to have a linear relationship with respect to either input beam in the small conversion regime [56], as given by

$$P_{\mathrm{MIR}} \propto P_{1064\,\mathrm{nm}} P_{1555\,\mathrm{nm}} \frac{d_{\mathrm{eff}}^2}{n_{1064\,\mathrm{nm}} n_{1555\,\mathrm{nm}} n_{3.4\,\mathrm{\mu m}} \lambda_{\mathrm{MIR}}^2} L, \tag{6.12}$$

where L is the crystal length and d_{eff} is the associated nonlinear coefficient for this interaction. Note, the linear dependence on L is a subtle mathematical difference for focussed beam interactions [54, 55] with respect to the plane wave interaction presented in equation 2.37; the plane wave assumption is only applicable for waveguides. The numerical phasematching curve in figure 6.7 is generated using the commercial software SNLO [185]. The data corresponds to 77 µm and 94 µm spot sizes for the 1064 nm and 1555 nm beams, respectively. This model also assumes perfectly Gaussian beam shapes, focal points at the centre of the crystal and the two beams are perfectly overlapped spatially. The spot sizes correspond to a ~35% increase in comparison to the design spot sizes presented in figures 6.6. These dimensions resulted in the closest comparison to the experimental data for an equal increase in both spot sizes, relative to numerically calculated spot sizes.

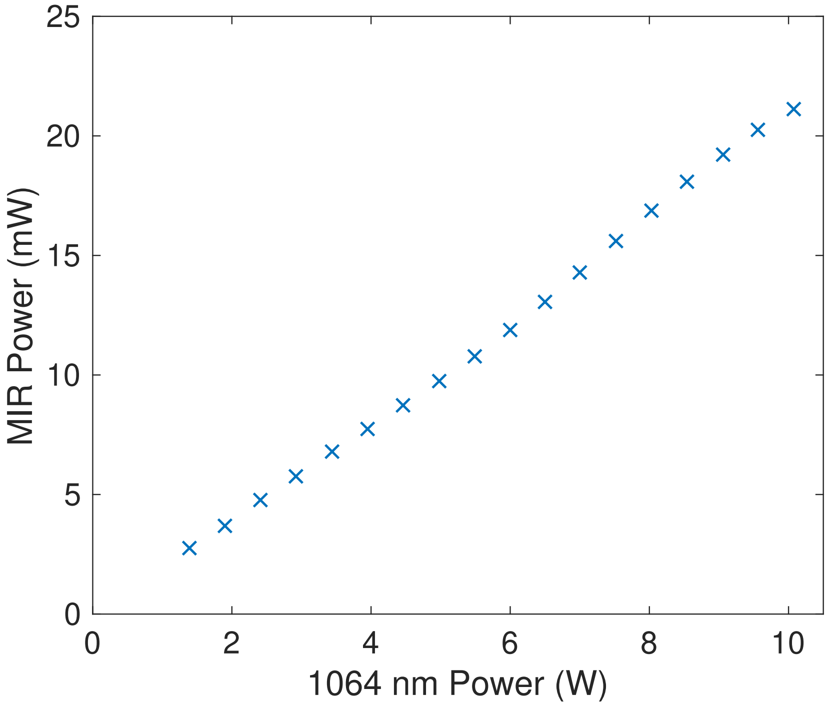

FIGURE 6.8: MIR power generated as a function of the 1064 nm laser source with the output of the EDFA constant at 2 W. The output is linear, as expected.

In comparison to previous single pass DFG works using these approximate wavelengths [159], this work is almost three times more efficient; generating 9.7 mW in comparison to 3.4 mW at 2 W of 1550 nm and 5 W of 1064 nm, which were the optical powers used in Su *et al.*'s work where they had a 50 mm-long crystal. This increase in efficiency is likely due to focussing conditions or preservation of the linear polarisation along the extraordinary axis of the LN crystal. The higher power sources available in this work are optimal for testing but the conversion efficiency is a key indicator for the potential to reduce the footprint of a transmitter source while still having enough power to reach the receiver.

6.5.2 NIR generation via SFG

Experimentally, collimation of a MIR beam is challenging with perhaps very little reward. To overcome the deviation from ideal collimation, a knife-edge measurement of the beam diameter was carried out at two points in the setup (post the Au mirror, figure 6.5, and prior to the intended position of the focussing mirror for the next nonlinear interaction). These were located 64 cm apart. The MIR beam expanded from 2.9 mm to 3.9 mm, corresponding to $\theta = 0.781$ mrad. Using equation 2.45, this enables a calculation of the theoretical beam waist, w, and the distance from the hypothetical focus can be determined from the beam waist equation [59]

$$w(z) = w_0 \left(1 + \frac{\lambda z}{\pi w_0^2}\right)^{1/2}, \tag{6.13}$$

allowing for a similar numerical design as carried out in figures 6.6(a) and 6.6(b) to determine optimal location and focal length lens for the SFG interaction. It was determined a 200 mm lens was the most applicable. The alignment procedure is carried out identically to the DFG system; an optical chopper is placed directly before the objective lens (OBJ) in figure 6.9 and lock-in amplification is utilised to initially co-align the MIR and 1064 nm beams inside the PPLN_{SFG} crystal. It was determined the fibre-coupling procedure was sufficient by removing the bandpass filter (BPF) and coupling the parasitically generated green light. Replacing the BPF into the beam path enables adequate detection. Alignment in the PPLN crystal, crystal temperature and fibre-coupling are all optimised following the initial detection of a 809 nm signal. The phasematching curve for this SFG process as a function of temperature is shown in figure 6.10. As before, the theoretical phasematching curve is also shown.

For future applications, the receiver in an industrial application of this system may be limited to certain size, weight and power restrictions. This is one of the key reasons for investigating the quality of data transfer without the capability of optical power amplification and working in the silicon absorption band. Hence, a half-wave plate and polarising beamsplitter is placed in the path of the 1064 nm beam prior to recombination with the MIR beam at the dichroic mirror, DM, in figure 6.9. This allows for safe attenuation of the 1064 nm power reaching the PPLN_{SFG} crystal to emulate a receiver which has a limited supply of 1064 nm optical power. The calibration of this attenuation is carried out with the 1064 nm laser set to output 1.9 W and a thermal power metre (S302C, Thorlabs) is placed directly before the PPLN facet to account for loss at all previous optical components. With respect to the angle offset of which a maximum power throughput was obtained, this calibration data is presented in figure 6.11. This calibration is used as a scaling factor of 1064 nm power when the laser is set to maximum power (10 W); it also serves as verification that the linear polarisation of the beam has been preserved to this point.

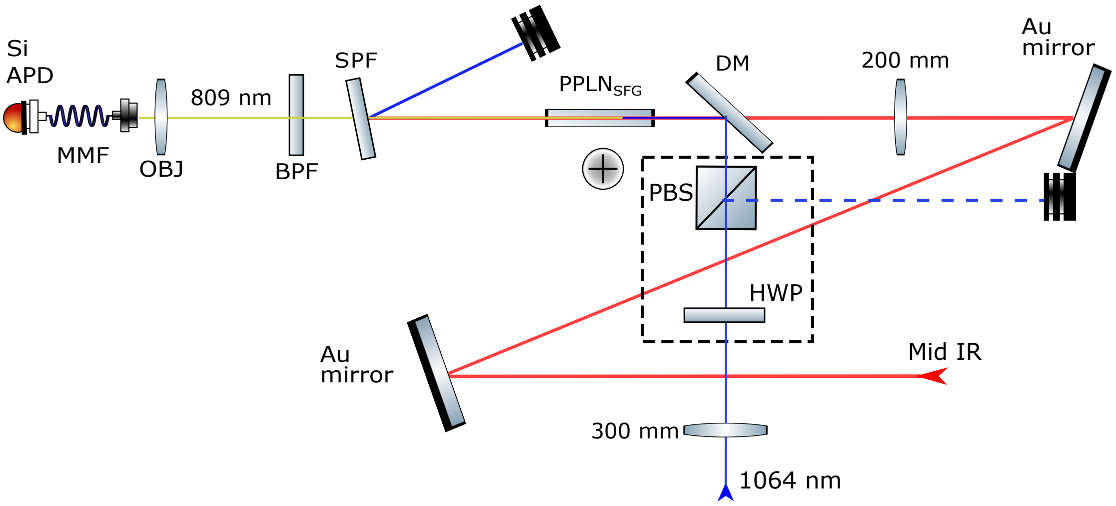

Figure 6.9: Schematic of the optical setup used to construct the SFG portion of this system to create the 809 nm light for high speed detection using a silicon photodiode. The dashed box surrounding the HWP and PBS is to indicate this system has been characterised with and without these components. The addition of these optics enabled the study of attenuating the 1064 nm power in the receiver system only with a constant power at the MIR generation stage. The dashed 1064 nm beam indicates this free space beam path is only present when the attenuation optics are in place.

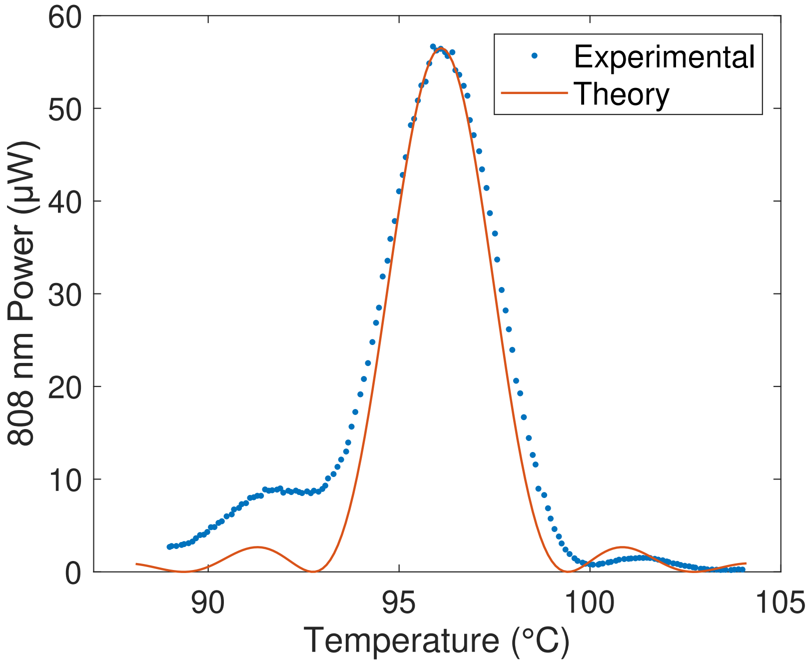

Figure 6.10: Temperature dependent phasematching spectra for the receiver PPLN crystal in this upconversion detection system for SFG of the pump and previously generated MIR beam. This data represents the maximum 809 nm power obtained from the SFG process during experimentation with the EDFA limited to 2 W.

Given this calibration, the nonlinear conversion can now be characterised for this bulk PPLN crystal and is presented in figure 6.12. The expected relationship to incident

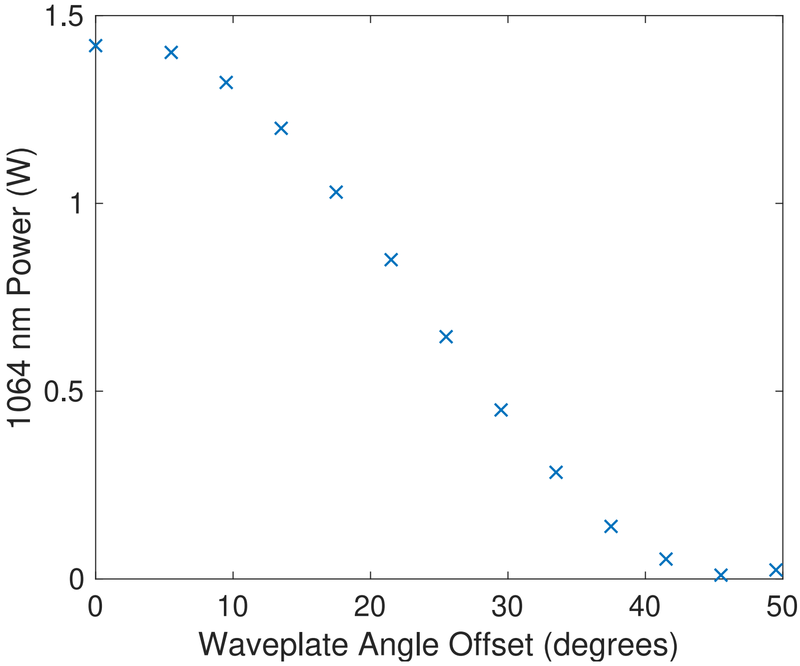

FIGURE 6.11: Modification of the 1064 nm optical power delivered to $\mathrm{PPLN_{DFG}}$ via rotation of the HWP in figure 6.9. Laser output power was ~1.9 W. This is simple confirmation that the polarisation linearity has not been negatively impacted and forms the calibration required for further experimental investigations of this system.

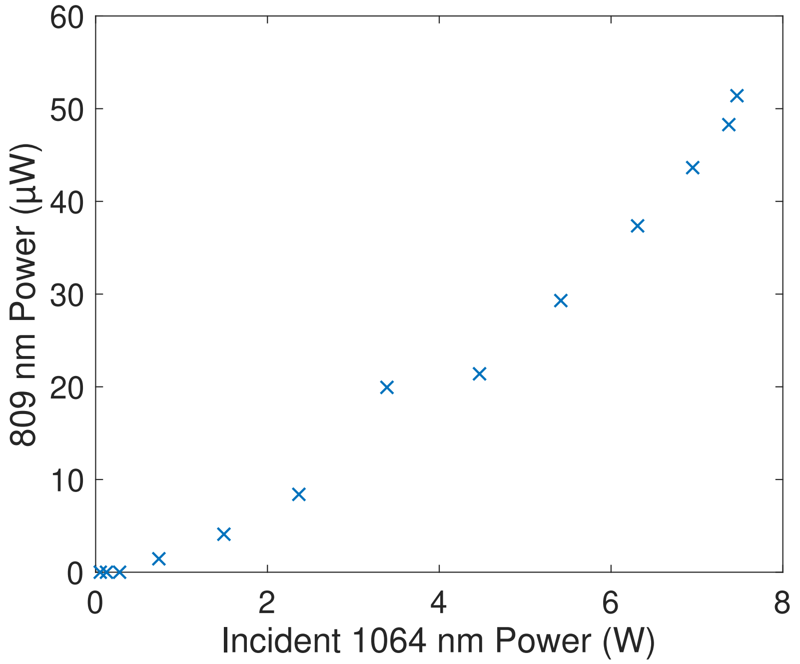

FIGURE 6.12: SFG generation power relationship to the incident 1064 nm power which ha been calibrated to account for loss in prior optical components. Standard deviation of each measurement is within the size of the markers.

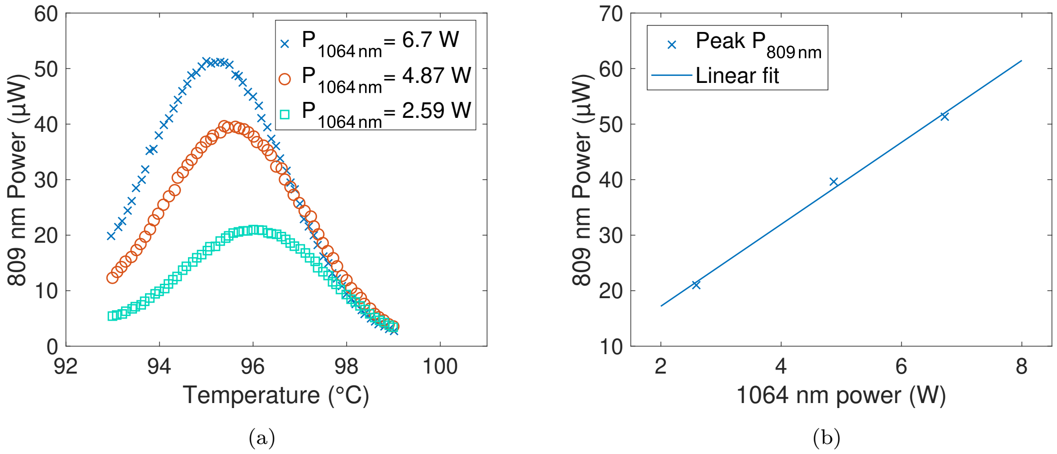

FIGURE 6.13: (a) Temperature tuning across the phasematching condition for the SFG process in the second stage of this system for a subset optical powers more commonly used in this work. Note, changing value of the phasematching temperature through optical power adjustments. (b) The peak power of each temperature tuning as a function of the incident power. The data has an approximately linear relation, as expected by theory.

power is linear, as given by [54]

$$P_{809\,\mathrm{nm}} \propto \frac{P_{1064\,\mathrm{nm}} P_{3.4\,\mathrm{\mu m}}}{\lambda_{1064\,\mathrm{nm}} \lambda_{3.4\,\mathrm{\mu m}} \lambda_{809\,\mathrm{nm}}} L d_{\mathrm{eff}}^2 \mathrm{sinc}^2\left(\frac{\Delta k_{\mathrm{SFG}} L}{2}\right) \tag{6.14}$$

for the small conversion regime of a SFG interaction. However, the data follows a 3/2-power relationship, not quadratic as it may appear to the eye. The reasoning for this is due to the offset in phasematching temperature as the incident power of the 1064 nm is increased; which will feature in the momentum parameter Δk_{SFG}. It is likely the heating of this crystal is occurring due to the thinner PPLN crystal, 0.5 mm, being used for the SFG process. This increases the chance of the incoming laser clipping the edge of the crystal and heating either the mount or cover slip which is clamped above the sample for PPLN crystals supplied by Covesion Ltd.

A smaller subset of data points throughout this data set were temperature tuned to confirm this and to rule out any other effects. These temperature-tuned phasematching spectra are shown in figure 6.13(a). The inverse relationship of phasematching temperature to incident 1064 nm power can be clearly seen. This is consistent with a hypothesis that the input beam is heating the crystal and hence requires the thermo-electric heater to be set at a lower temperature to compensate for this. As can be seen in figure 6.13(b), the trend of incident power to generated power follows an approximately linear relationship, which was the theoretical expectation for this nonlinear process. This simply verifies there is no unaccounted for nonlinear process occurring which would need to be addressed.

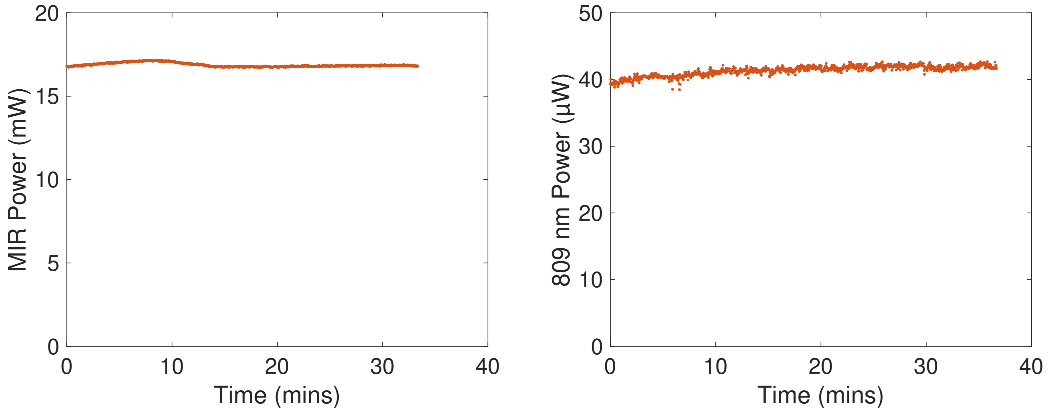

(a) (b)

FIGURE 6.14: Investigation of the stability of the generated beams over the course of a ~40 min period. Due to some thermal equilibrating, the presented standard deviation values are for the data after 12 min in figure (a) and 10 min in figure (b)

As shown to be achievable in figure 6.10, ~50 µW provides enough power for detection using a silicon avalanche photodiode for optical data transfer. Using these high-quality commercial sources, the transmission scheme demonstrated intensity stability with standard deviations of 37 µW and 0.67 µW, over a 30-minute duration, for the generated MIR and 809 nm signal, presented in figures 6.14(a) and 6.14(b), respectively. Thus, establishing the potential for stable optical communications; quality of data transferred is discussed and presented in the following section. Additionally, after passing through two nonlinear conversion processes, a signal-to-noise ratio (SNR) of at least 45 dB is confirmed for the generated 809 nm signal, figure 6.15(c), without any additional spectral filters whilst using commercial sources. The 1555 nm and 1064 nm commercial sources' spectra are presented in figures 6.15(a) and 6.15(b), respectively. This SNR is comparable to that which Su *et al.* [159] achieved for their scheme in which the regenerate a C-band signal although the authors do not explicitly state this value in their work.

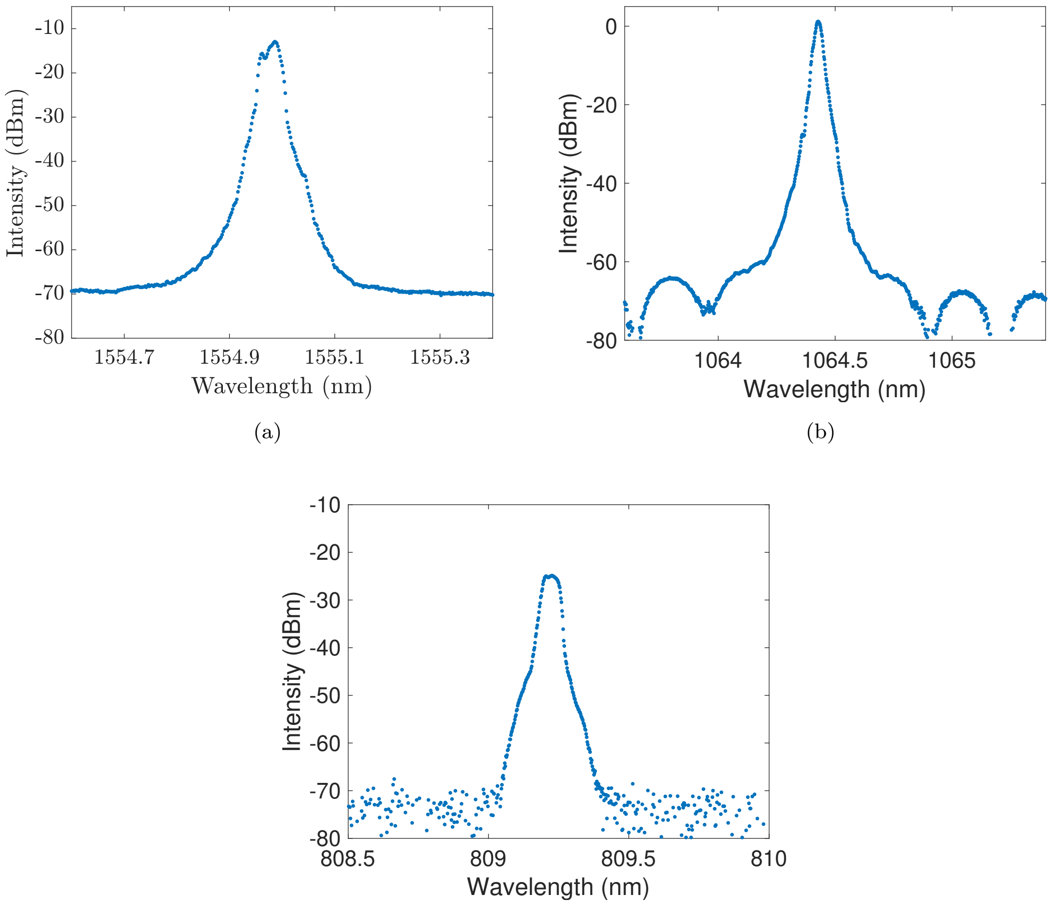

(a)

(b)

(c)

FIGURE 6.15: Spectra of the respective signals used and generated in this optical telecommunication setup: (a) Modulated and CW 1560 nm source, (b)the 1064 nm laser which forms the pump wavelength of the nonlinear interactions and (c) the final generated beam at 809 nm suitable for detection on a silicon detector.

6.6 Characterisation of data transfer and BER

As previously discussed, the EOM in figure 6.5 is the optical component which enables the modulation of the 1550 nm beam to carry the pseudo-random bit stream (PRBS). A PRBS is configured such that the numbers of 0's and 1's are approximately equal for neutral, balanced data. It is accepted that they allow for a shorter time requirement to estimate the quality of a transmitted signal. Although time is not a key concern here, this configuration is standard for a commercial bit error rate tester (BERT) and is straightforward to implement. Additionally, the supply voltage for the EOM is chosen to optimise the BER of a low power 1550 nm signal after EDFA amplification. It is marginally adjusted prior to each use to account for any thermal variation or absolute drift in the power supplies of which is typically negligible. Standard parameters for the EOM are a DC offset voltage of 1.8 V and a modulation voltage amplitude of 560 mV. The RF voltage is then passed through an RF amplifier prior to phase shifting the channel waveguide within the EOM. The BERT used does have the ability to generate a DC offset voltage but it was found to be limited to lower than required to drive this particular EOM.

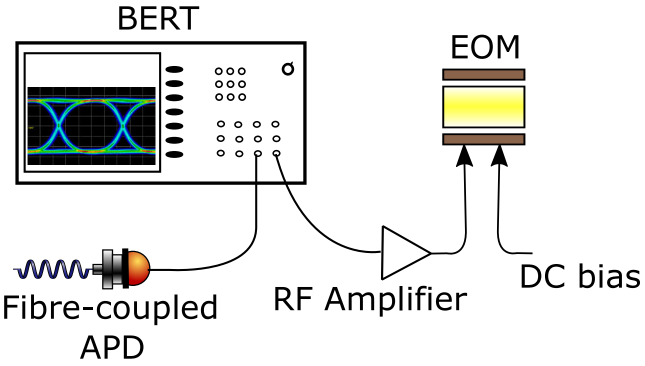

FIGURE 6.16: RF signal output and input connections to the bit error rate tester.

Before proceeding with the nonlinear optical investigations of this telecommunications system, the data rate should be chosen. Using the final upconverted wavelength, the BER is displayed in figure 6.17 as a function of the BERT's data frequency. While one might expect the response to be flat, the shape of the data is essentially decided by the hardware specifications. The APD used is specified up to 1 GHz but the BERT signal is particularly poor at lower frequencies as it is designed for up to 12.5 GHz testing. Hence, I proceed with optical testing with the BERT set at 1.25 GHz.

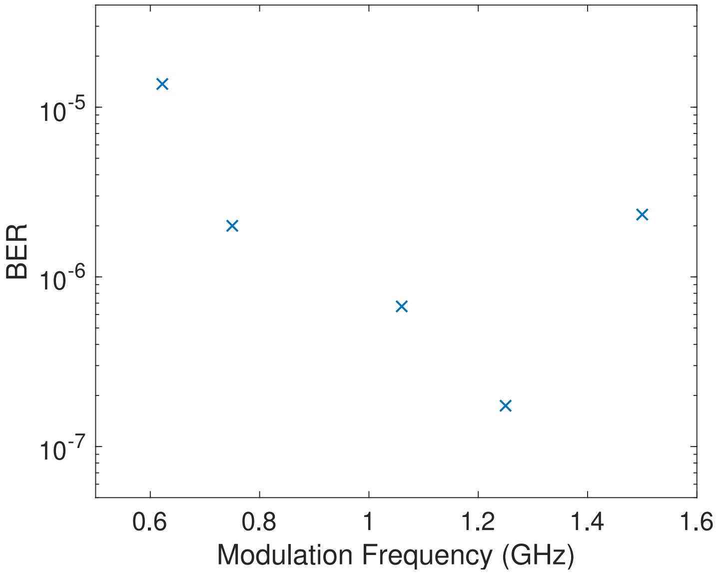

FIGURE 6.17: The BER corresponding to the modulation frequency of its output for the entire upconversion detection system. The given frequency which provides the smallest BER value is chosen to proceed with for the remaining investigations; in this case, the value chosen was 1.25 GHz.

Figures 6.18(a) and 6.18(b) demonstrate the impact introducing the HWP and PBS optics had on the receiver system. The presented data corresponds to a fixed angle

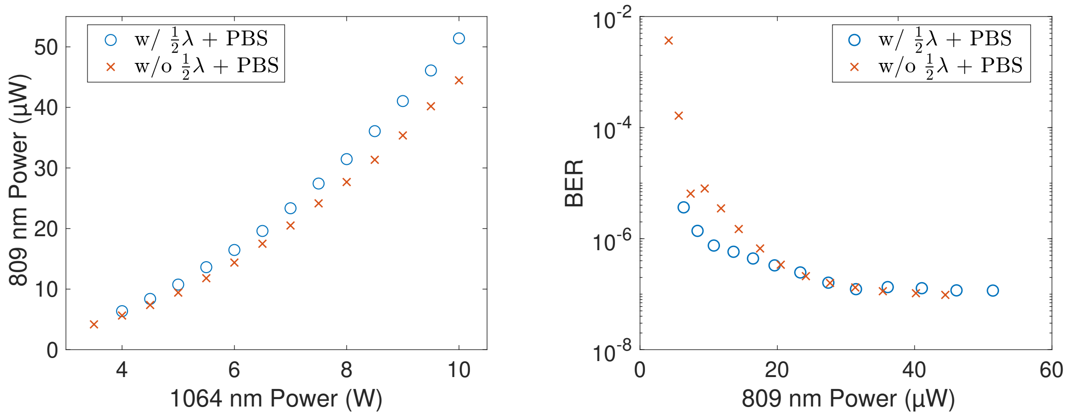

(a) (b)

FIGURE 6.18: Investigating the effect introducing the half-wave plate and PBS had on system characterisation.(a) Total generated 809 nm as a function of the initial 1064 nm laser setpoint. (b) The resulting BER as a function of 809 nm for both system configurations.

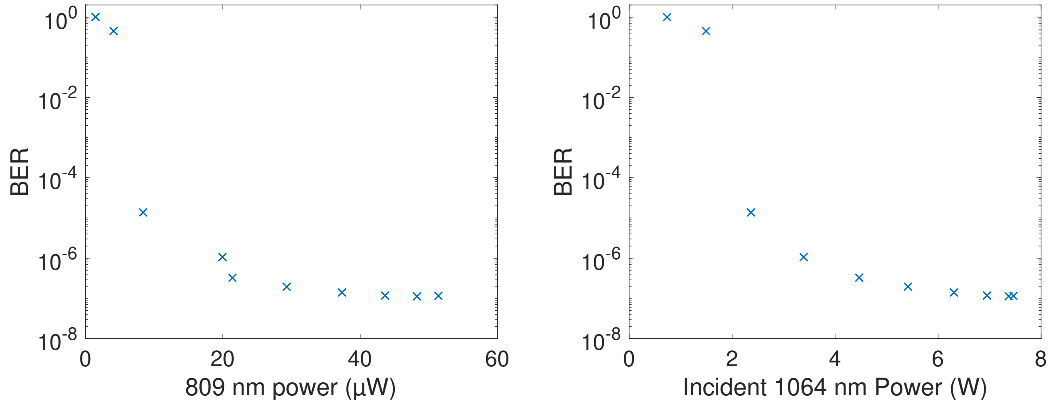

(a) (b)

FIGURE 6.19: (a) 809 nm power detected on the APD and the corresponding BER value. (b) BER as a function of the 1064 nm power used in the SFG interaction. Both figures correspond to the attenuation of the 1064 nm power reaching $\mathrm{PPLN}_{\mathrm{SFG}}$ via the HWP/PBS optics in figure 6.9.

for the HWP at which there is maximum power throughput. It is apparent that the conversion efficiency is marginally increased. This will be due to the length of higher refractive index material the beam passed through in the PBS; altering the focussing conditions of the 1064 nm beam which is converging as it passes through this optic and creates a moderately more efficient interaction. However, this has not resulted in a lower BER value for the increased 809 nm power, figure 6.18(b). The potential reasons which may be limiting the BER is discussed in section 6.6.1.

The characterisation of the BERs resulting from attenuation of 1064 nm power reaching $\mathrm{PPLN}_{\mathrm{SFG}}$ is presented in figures 6.19(a) and 6.19(b), as a function of the 809 nm and

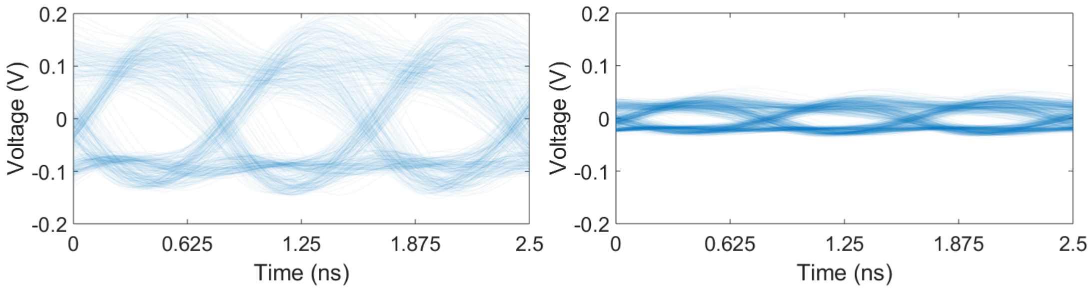

(a) (b)

FIGURE 6.20: Eye diagrams associated to the 809 nm light following a DFG process for creation of MIr radiation and then upconversion detection to this frequency for high-speed detection. (a) Eye diagram corresponding to the lowest BER achieved and (b) a BER of approx. 10^{-5}.

1064 nm power, respectively. This system achieves a minimum BER of 1.1×10^{-7}. Eye diagrams associated to this minimum BER and another associated to a BER of ~10^{-5} can be seen in figures 6.20(a) and 6.20(b), respectively.

6.6.1 Discussion

The BER measurements of this system, while indicative of a true application, are limited by the superposition of the data stream on the 1064 nm beam. This is intuitively expected due to the DFG process in which the 1064 nm photon splits into a ~1550 nm and 3.4 µm photon, in this specific parametric process. Theoretically, the 1550 nm beam can be amplified, typically called optical parametric amplification (OPA); in fact, this is one method to create a high-power, pulsed 1550 nm source using a low-power 1550 nm seed and a pulsed 1064 nm source. Although this is a quantum mechanical description, this conservation of energy process is also described through the semi-classical Manley-Rowe equations for a three-photon process. Both view-points must be considered for a complete description. However, this is not useful here as the 1550 nm beam is not re-used for any purpose. What is relevant is the partial depletion of the 1064 nm beam in phase with the 1550 nm bit stream. With no engineering solution in place to align the phases of the data, there is inherently destructive interference in the generated 809 nm beam. I do not attempt to align the data of the beams as this task would be very challenging due to the nature of the PRBS; in which you would need to essentially perform the function of a BERT in phase-aligning the PRBS spatially. The un-aligned partial depletion of the 1064 nm would cause a fluctuation in the power available for SFG to the 809 nm signal. This is one likely reason for the increased variation in measured power present in the lower and upper (0 and 1 bits, respectively) sections of the eye diagram, figure 6.20(a). This is commonly termed signal distortion.

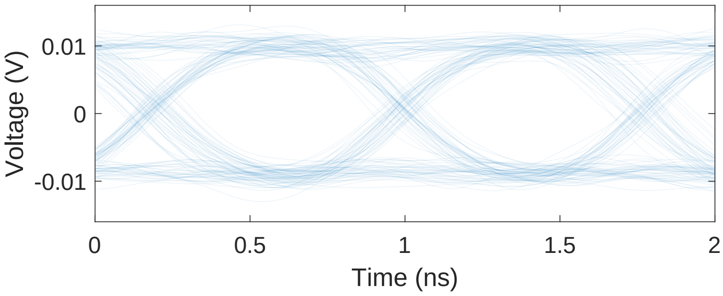

FIGURE 6.21: Eye diagram resulting from the partial depletion of the 1064 nm pump beam after mixing with the modulated 1550 nm signal at a rate of 1.25 GHz.

6.6.1.1 Limitations in design engineering and application

The presented system has many potential applications and advantages but there are further considerations prior to proceeding with the development of such a system for commercial applications. Firstly, some theoretical considerations. When choosing the final detection wavelength, the DFG process for detection in the telecommunication C-band, used in other works [159], is theoretically more efficient when you reach the efficiency levels where pump depletion is more clearly observed. This is only likely to occur with the high peak powers available when using pulsed laser sources.

The inability to do a standardised back-to-back as the receiver is not capable of detecting the modulated laser wavelength in the transmitter in another potential drawback. This provides an engineering challenge of system characterisation when designing bespoke components which may be in the optical path. For cases such as this, it may be desirable to implement a DFG phasematching PPLN crystal in place for the receiver system during initial design. Subsequently, the PPLN crystal and the detector can be substituted for the potential benefits of using a Si-detector configuration.

The chosen data rate of 1.25 Gbps to perform this system characterisation at is undeniably a compromise of current electronic components. This is primarily due to the BERT having a non-ideal output of the signal introduced into the experiment; a qualitative investigation to verify this point was hence carried out. To confirm the source of error for improvements in future work, eye diagrams corresponding to various electrical arrangements and early optical modulation was acquired, presented in figure 6.22. The initial source of error limiting the transfer of data is seen in the dissimilarity between figures 6.22(a) and 6.22(b). These represent the signal, modulated at 1.25 Gbps, directly out of the BERT and subsequent RF amplifier, respectively. The amplifier refers to that shown in the RF system, figure 6.16. The increase in signal-to-noise ratio and the timing jitter of the electrical signal is clearly apparent. Figures 6.22(c) and 6.22(d) are the 2.48 and 3.125 Gbps electrical signals directly out of the BERT, respectively. The post amplifier data is not presented as this frequency is above its operating range. Finally, figures 6.22(e) and 6.22(f) are the 1.25 Gbps data from the 1550 nm and post EDFA amplification, respectively, with approximately 1 mW of optical power detected in both cases. While it appears the signal is smoother and continuous from the BERT at higher modulation frequencies, this is potentially due to the limited timing resolution of the oscilloscope. The additional timing jitter resulting from the RF amplifier is observed in the optical, 1550 nm data is likely to be one of the larger sources of error in this upconversion communications system. This provides an area for further development of this system once a RF amplifier meeting the specifications required can be sourced.

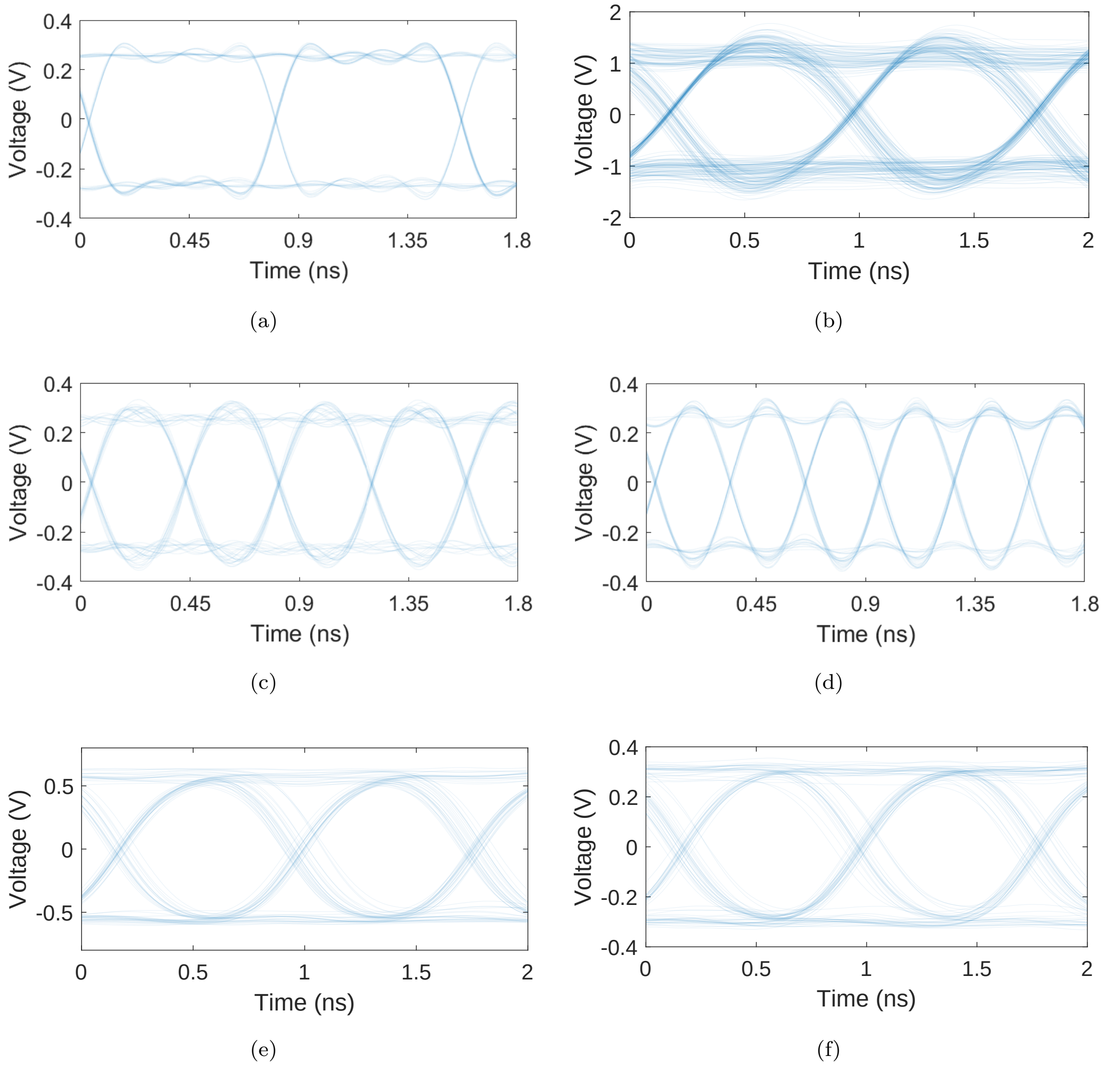

(a) (b)

(c) (d)

(e) (f)

FIGURE 6.22: Eye diagrams corresponding to (a) 1.25 Gpbs signal directly out of the BERT, (b) 1.25 Gpbs signal following the RF amplifier which precedes the connection to the EOM, (c) 2.48 Gpbs signal directly out of the BERT, (d) 3.125 Gpbs signal directly out of the BERT, (e) 1.25 Gpbs signal optically detected directly after the 1550 nm seed laser, (f) 1.25 Gpbs signal optically detected after EDFA amplification of the seed laser.

6.7 Relative intensity noise measurements

RIN is typically used for the characterisation of new lasers to quantify their limitations and specifications for a future end-user. Whereas here in this investigation, we simply aim to answer the question of whether an end-user for the application of upconversion telecommunications should invest in a high quality, low noise 1064 nm laser (the pump) or the 1550 nm seed laser plus EDFA which will be the data-containing beam.

Unlike previous works [182], the work here will provide a qualitative discussion of noise level. To analyse the contribution of intensity noise in our system, we firstly exchange the EDFA used previously to a higher power version with a maximum output of 5 W to increase the average 809 nm optical power to 129 µW. This 5 W EDFA still has a fibre-coupled output and is linearly polarised along the same axis from the fibre so no alterations to the optical design were required. Considering the additional noise above the shot noise limit, I propose a new parameter, σ_i, defined as

$$\sigma_i = S_{p,i}(f)R - N_{shot,i}, \tag{6.15}$$

where $S_{p,i}(f)$ was defined in equation 6.11, R is the responsivity of the detector as a function of frequency [186] and $N_{shot,i}$ was defined in equation 6.9. The responsivity of the detectors used in this work is provided in dB by the manufacturers so a unit conversion to the linear scale is not required for this step. This calculation allows for a partially quantitative examination of the contributions to intensity noise where the shot noise is the fundamental limit set by the optical power received. The dense population of peaks in the noise signals under 300 MHz are typically a result of electrical noise and the power supplies used to power the laser sources. This calculation for each optical source is performed at a frequency sufficiently far away from these noise peaks; 800 MHz was the noise frequency chosen for this. The 809 nm generated signal's noise, $\sigma_{809\mathrm{nm}}$, is approximately 22.5 dB above its shot noise limit.

It can now be hypothesised/proposed that this level of noise is a result of the contributing source lasers to the final SFG process,

$$\sigma_{809\mathrm{nm}} = 2 * \sigma_{1064\mathrm{nm}} + \sigma_{1550\mathrm{nm}}, \tag{6.16}$$

which equals ~22 dB in this investigation. Each of these noise power spectral densities are shown in figure 6.23. As laser RIN is a relevant factor for spectroscopy applications, considering the contributing noise sources is vital prior to system development if applications were to employ a scheme in which the pump is re-used rather than split before the nonlinear processes. This work indicates an equal contribution of excess spectral noise relative to the shot noise floor per each pass through a nonlinear process. This

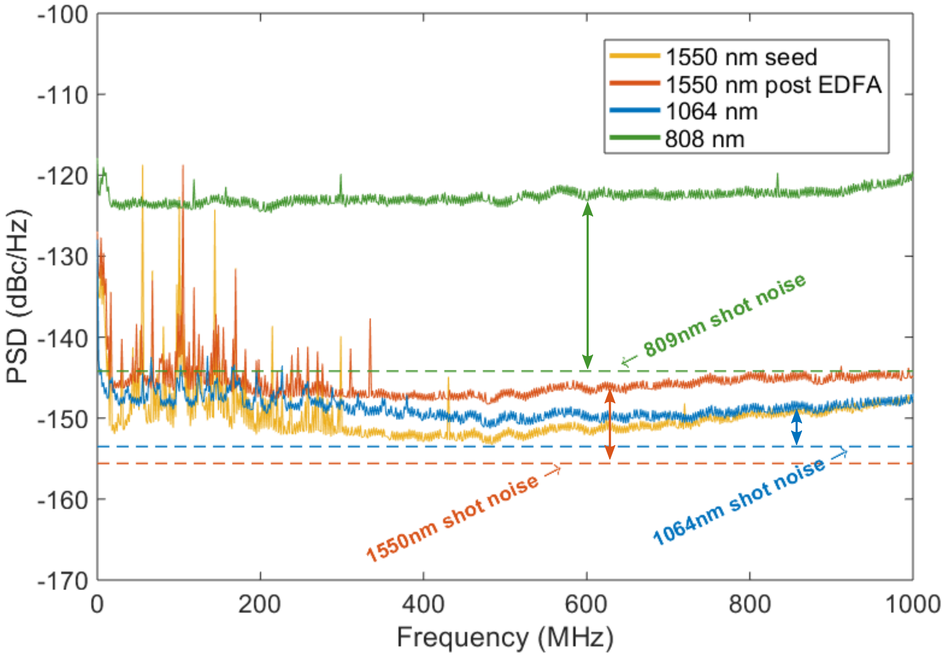

FIGURE 6.23: Power spectral density of laser sources and generated signal following normalisation to the responsivity of the corresponding detectors. This allows for comparison of the noise level to the the shot level for the corresponding noise trace. The vertical arrows are indicative of the proposed parameter to study the noise contributions in a parametric process, but not at the precise frequency value of which the calculation was performed.

implies the 1064 nm source is worth additional consideration prior to purchasing a commercial source if one wants to design a system equivalent to that which was presented in figures 6.5 and 6.9. However, for communication systems that will be separated in a real-world application, size and weight are expected to be among the dominant design factors.

6.8 Conclusions

An upconversion detection system has been investigated and characterised to determine the applicability of detection in the silicon absorption band. This was carried out using commercially available laser sources, PPLN crystals and silicon APD. A minimum BER of 10^{-7} was achieved for transmission of 1.25 Gbps data in an on-off keying modulation format where no further optical amplification has been implemented to boost the signal prior to detection. The noise contribution from each of the relevant lasers was also investigated. This has been achieved using single pass nonlinear conversion in bulk crystals and component limitations have been identified. This demonstrates potential for future work in this area.

The data speed used in this work, 1.25 Gbps, is very much limited by the silicon APD used. Low noise, faster RF amplifiers are easily available once the design of a system has no financial limitations. While the silicon APD had high sensitivity and was easily capable of detecting the µW-levels of optical power used here, the author could not source a higher speed version commercially available. This work proved the capability of employing commercial lasers, nonlinear crystals, optical components and detectors but the true power in this technological route will lie in the development of PPLN waveguides designed for DFG and SFG operation for the wavelengths used here; enhancing the conversion efficiency and system miniaturisation. Bringing the detected power into the mW range after down- and up-conversion will allow for standard PIN detectors to be applied to this problem, which can have detection bandwidths up to 10 GHz for silicon based devices.

Chapter 7

Integrated optical fibre refractometer

7.1 Introduction

This chapter presents work on the development of the integrated optical fibre platform, primarily the development of a refractometer operating as a leaky mode waveguide with variable propagation loss. This work led to an early publication and was targeted at applications in the aerospace industry. However, the integrated optical platform is a viable route for an integrated waveguide for routing photons due to its inherent low propagation losses [187] when then optical fibre isn't intentionally etched for access to the propagating mode.

In comparison to free-space optics, integrated optics offers the advantages of thermal stability and to perform operations such as phase-shifting in a single, small-footprint device. Utilising the well-established industry of optical fibre fabrication, binding these low-loss waveguides to a substrate can combine the inherent advantages of both platforms. The engineering challenges presented by the fabrication of such a platform is presented in this chapter along with initial characterisation. In the development of the integrated optical fibre (IOF) platform, a simple IOF refractometer was fabricated by characterising the response of an etched optical fibre to different surrounding refractive indices. Chemically etching the fibres to thinner diameters was considered as a potential route to evanescent field exposure for detectors such as transition edge sensors [188], however it is shown to introduce a high propagation loss into the waveguide.

Integrated optical fibre (IOF) is a novel optical platform exclusive to the University of Southampton. To date, the IOF platform has enabled the fabrication of an anenometer [189], a highly stable external cavity diode [19], a fibre-tip cantilever [122] and evanescent field sensing refractometry [190]. The platform involves binding an optical fibre to a planar substrate via the flame hydrolysis deposition process described in section 7.2. The resulting IOF chip, is as robust as a planar waveguide with the added advantage of having the low propagation loss associated with current optical fibre technology. An example image is shown in figure 7.1. Hence, the platform has potential for applications in harsh environment sensing and quantum optical circuitry.

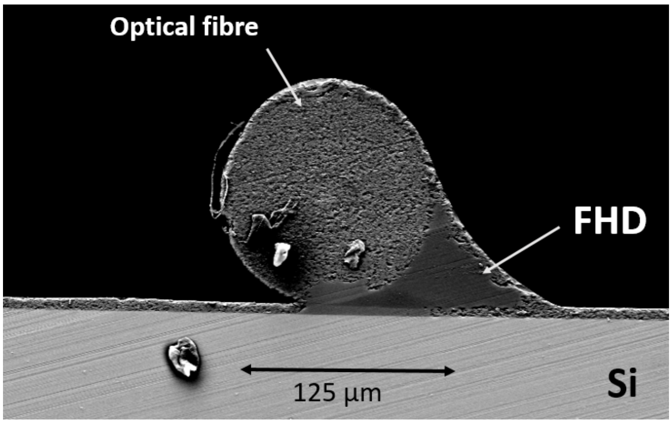

FIGURE 7.1: Example backscatter scanning electron micrograph of the IOF platform. The image shows an SMF-28 optical fibre fused to a silicon substrate.

7.2 Flame Hydrolysis Deposition

Flame hydrolysis deposition (FHD) utilizes the techniques developed in optical fibre fabrication to create planar optical devices. An FHD system was initially developed by Watts [191] in the University of Southampton but the current system was provided by the Centre for Integrated Optics (CIP), seen in figure 7.2. This technique is feasible due the widely available, high quality silicon wafers to act as substrates due to the microelectronics industry. Development of silica integrated optics opens a path to the eventual integration of optical and semiconductor circuitry. Precursors used include silicon tetrachloride ($SiCl_4$) boron trichloride (BCl_3) phosphorus trichloride (PCl_3) and germanium tetrachloride ($GeCl_4$). Boron and phosphorous allow for control over the refractive index and consolidation temperatures. Germanium is primarily used to develop the photosensitive core layer of planar waveguides. The halides present in the flame, play a vital role in the chemical reaction forming the silicate layer. If the temperature of the inner cone of this oxygen-hydrogen flame is above 1200 °C, direct oxidation is assumed to occur per equation 7.1. At temperatures below this, direct oxidation does not occur and hydrolysis is the dominant reaction, as per equation 7.2.

$$SiCl_4 + O_2 \rightarrow SiO_2 + 2Cl_2 \tag{7.1}$$

$$SiCl_4 + 2H_2O \rightarrow SiO_2 + HCl \tag{7.2}$$

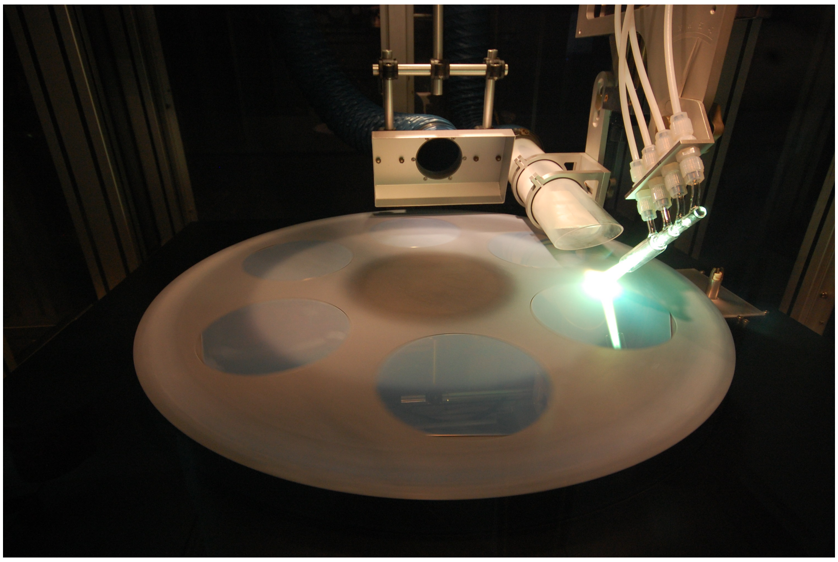

FIGURE 7.2: Photo of the FHD deposition tool half way through a pass. This is evident by the difference in soot thickness on the turntable.(Photo courtesy of Dr. James Gates)

The FHD system that is used throughout this work uses nitrogen as a carrier gas for the precursors and is bubbled through chloride precursors. Argon is used to shape and direct the flame away from the torch. Precursors are heated in their respective pipework to ensure they reach the torch in a gaseous state. The exception to this is BCl_3 which is a gas at room temperature. Following the deposition of the silica soot, the layer is consolidated in a furnace above temperatures of 1100 °C. This forms the silica glass layer required. The same FHD system which is used in the fabricating planar waveguides for various application [21, 22, 192] has also been demonstrated in fusing optical fibre to a silica-on-silicon substrate.

7.3 Optical Simulation Theory

To aid in fabrication and to explain experimental results, a number of numerical and semi-analytical techniques have been used in this work. The refractometer presented in section 7.4 exhibits the characteristics of leaky mode waveguide. Hence, a route to explain experimental results was required. The corresponding method used for this will be explained in this section.

7.3.1 Transfer Matrix Method for Leaky Waveguides

The technique used here is a modified TMM developed by Ramadas *et al.*[193] and was recently used in a similar leaky waveguide analysis [194]. This technique is explicitly applicable to planar waveguide structures in which the outer layers are semi-infinite. The method is relatively straightforward and allows the complex propagation constant,

β_i, to be evaluated by real matrices, derived by considering electric field continuity at the interfaces. This technique will be applied to the IOF refractometer developed and will be discussed in section 7.4. This technique allows for the an approximation of the device presented in this report to be theoretically understood and to propose routes for improvement.

An initial assumption is made that the electric field in the ith layer has the form

$$E_i = A_i \cos((x - d_i)k_i) + B_i \xi_i \sin((x - d_i)k_i), \tag{7.3}$$

where A_i and B_i are arbitrary constants, $k_i = (k_0^2 n_i^2 - \beta^2)^{1/2}$ and $\xi_i = 1/k_i$ for the TE polarisation case. x_i and d_i are the position within the layer and the location of the layer's boundary, respectively. The transfer matrix, g, representing the waveguide is evaluated by

$$g := \prod_{n=i}^{1} S_i \tag{7.4}$$

where the transfer matrix for each individual layer, S_i is defined as

$$S_i := \begin{cases} \begin{bmatrix} \cos(\Delta_i) & \xi_i \sin(\Delta_i) \\ -\frac{1}{\xi_i} \sin(\Delta_i) & \cos(\Delta_i) \end{bmatrix} & \text{for } k_i \in \mathbb{R} \\ \begin{bmatrix} \cosh(-\mathrm{i}\Delta_i) & \gamma_i \sinh(-\mathrm{i}\Delta_i) \\ \frac{1}{\gamma_i} \sinh(-\mathrm{i}\Delta_i) & \cosh(-\mathrm{i}\Delta_i) \end{bmatrix} & \text{for } k_i \in i\mathbb{R} \end{cases} \tag{7.5}$$

where $\Delta_i = k_i(d_{i+1} - d_i)$ and $\gamma_i = \mathrm{i}\xi_i$. The TE polarisation is the only case which shall be investigated in the progress of this work, as per the experimental data. The waveguide, in its entirety, is defined as

$$\begin{bmatrix} A_C \\ B_C \end{bmatrix} = g \begin{bmatrix} A_1 \\ B_1 \end{bmatrix} \tag{7.6}$$

where A_1 and B_1 represent the electric field constants in the substrate and A_C and B_C correspond to the covering material. In this work, the cover is the analyte. Considering exponential decay of the electric fields in the outermost layers, Ramadas *et al.* assign the conditions $A_1 = \gamma_1 B_1$ and $A_C = -\gamma_C B_C$ to derive the eigenvalue equation

$$F(\beta) = \gamma_1 g_{11} + g_{12} + \gamma_C \gamma_1 g_{21} + \gamma_C g_{22} = 0. \tag{7.7}$$

As per Ramadas *et al.*'s technique, plotting $|1/F(\beta)|^2$ as a function of effective index, the half width at half maximum (HWHM) of the Lorentzian shaped resonance peak equates to the complex propagation constant, β_i. Hence, propagation loss as a function of the refractive index of the analyte can be extracted. This is essential in numerically simulating the leaky IOF refractometer presented in this report in which the simplified model is presented in figure 7.3.

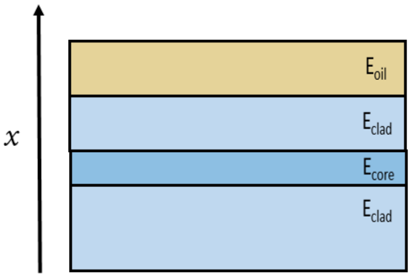

FIGURE 7.3: Model used in the application of the leaky mode transfer matrix method proposed by Ramadas *et. al* [193] to simulate the behaviour of a leaky mode waveguide as a refractometer

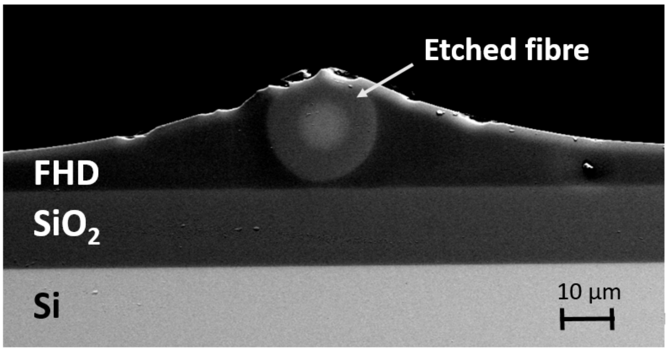

FIGURE 7.4: Backscatter SEM micrograph of the etched SMF-28 fibre embedded in a layer of FHD glass used as a refractometer in this work.

7.4 Leaky mode refractometry

In the field of refractometry, a number of techniques have been proposed: optical fibre-based multi-mode interference [195], bend loss[196], fibre Bragg gratings [197, 198] and tilted Bragg gratings [199, 200]. The additional advantage of using silica based devices is their chemical inertness. In the duration of this work and the development of the IOF platform, a refractometer was fabricated and characterized. The device utilized FBGs to determine propagation loss to quantify its response to a surrounding refractive index. Methodology for characterization and theoretical analysis of the device will be presented in this report.

The refractometer presented in this section was fabricated by HF etching an SMF-28 optical fibre to a diameter of approximately 22 µm, figure 7.4. It was subsequently bound to a silicon wafer with a 15 µm thermal oxide via FHD deposition. The thick oxide layer provided optical isolation from the silicon substrate for the etched optical fibre. Five Gaussian Bragg gratings were imprinted into the fibre via the dual-beam method described in [22]. The device was interrogated with a superluminescent diode (Amonics ASLD-CWDM-5B-FA), and the reflection spectrum characterised using an optical spectrum analyzer (OSA) (ANDO AQ6317B). The reflected signal was obtained using a 3 dB coupler, example data set shown in figure 7.5(a). To alter the refractive index external to the device, calibrated refractive index oils were used (Cargille-Sacher Laboratories Inc., series A and AA). To determine a reference FBG amplitude for each respective grating, the device was covered in an oil of n=1.42. This index is below the effective index of the fibre and is assumed to maximise the containment of modal power. It should be noted that all refractive indices recorded in this paper are scaled using the Cauchy equation considering wavelengths of 1550 nm from the calibrated value at 633 nm. Further measurements to calibrate this refractometer were normalised to the reference FBG amplitude to the measured spectrum. For each of the five FBGs, a data point is gathered per external refractive index value. An example of this data is displayed in figure 7.5(a). Loss at each grating position was normalised by the difference of the FBG's reflected power and the reference FBG amplitudes in air.

The propagation loss is the gradient of a linear fit to each data set using the least-squares method; a sample set is seen in figure 7.5(b). This method is a development and application of the propagation loss measurement technique proposed by Rogers *et. al*[201]. Spectral data was collected for each refractive index oil which were applied in a pseudorandom order to reduce the impact of remnant oil. Between data collection for different surrounding oils the device was cleaned using acetone and isopropyl alcohol, and dried with compressed air. The resulting data is shown in figure 7.6. Error bars displayed are representative of the standard error associated to each least square fit.

In addition to this calibration data, it was also attempted to use the presented refractometer to determine the concentration of water contamination in diesel. The water concentration ranged from 0 ppm to 220 ppm; provided by the Department of Chemistry here in Southampton. The resulting interrogation data from this experiment is also presented figure 7.6. The calculated propagation loss for each of these mixtures could

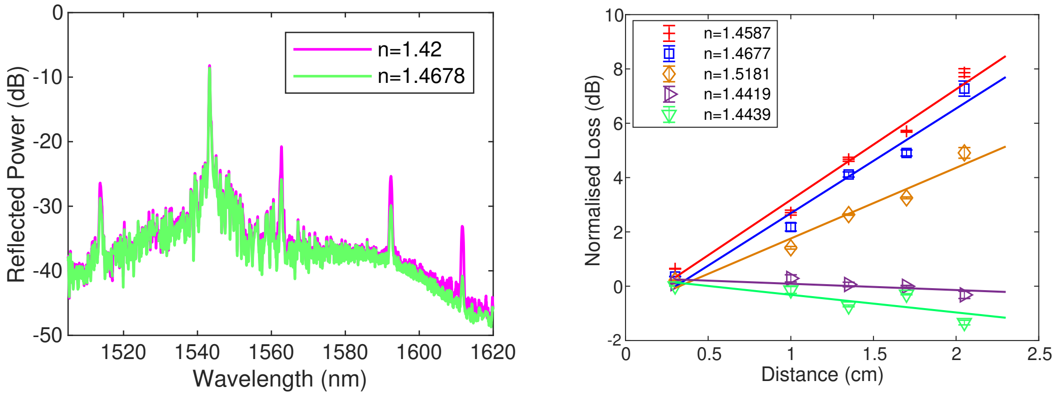

(a)

(b)

Figure 7.5: (a) Example back reflection spectra for two different external refractive indices. A reduction in FBG reflected power is observed for a higher propagation loss device. (b) A sample set of data showing the FBG back-reflected power ratio as a function of length into the waveguide. The slope is observed to be dependent on the analyte's refractive index.

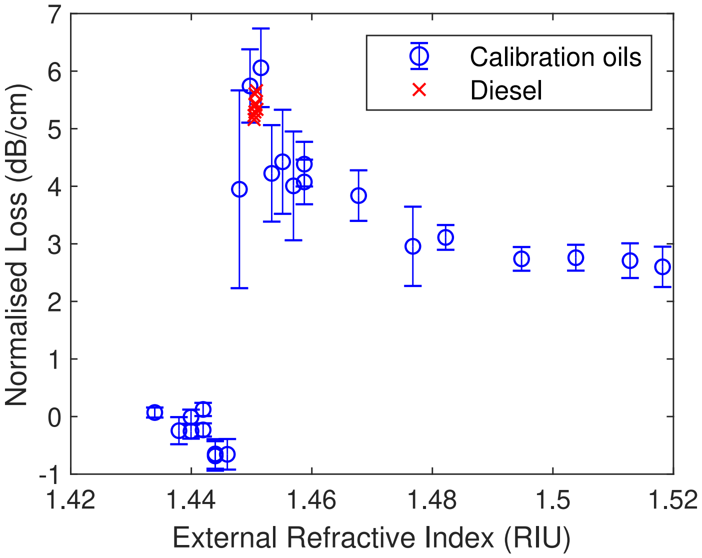

FIGURE 7.6: Calibration data of the presented refractometer. The device can be seen to not operate as a leaky mode waveguide when surrounded with index matching oils below that of waveguide clad. Interrogation of water contaminated diesel samples (0-200 ppm) is shown to fall within the error of this refractometer.

not be discriminated between, indicating a limitation in the applicability of this device as a sensor. Nevertheless, this does not rule out the potential for leaky mode waveguides to be utilised as refractometers as their sensitivity can be increased.

The Ramadas *et. al* method presented in section 7.3.1 enables a route to understand the trend observed in figure 7.6. The waveguide used in this work work is 22 µm in diameter. An analogy to this as a planar model allows for an upper clad thickness to be calculated and an investigation into the relation between propagation loss and a

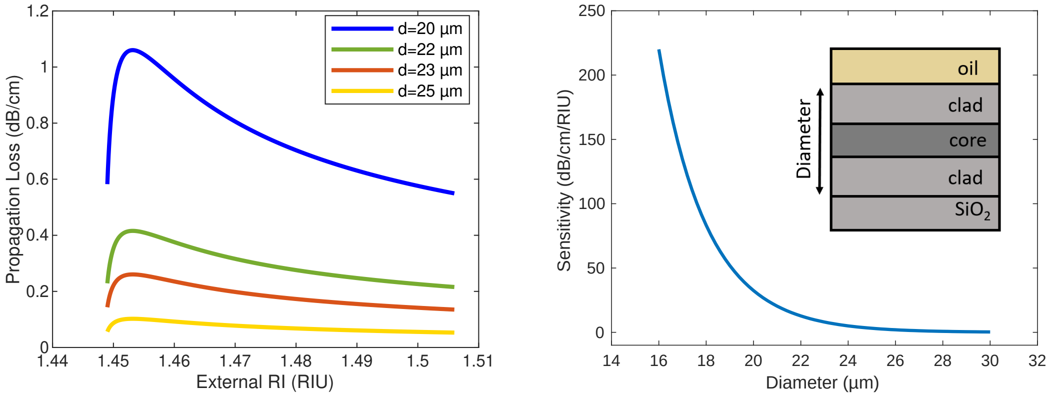

(a) (b)

FIGURE 7.7: (a) Numerical simulation results of propagation loss for different fibre diameters. (b) Theoretical sensitivity of a planar model of the device at a refractive index of 1.456. An exponential increase in sensitivity is shown with respect to a decreasing diameter.

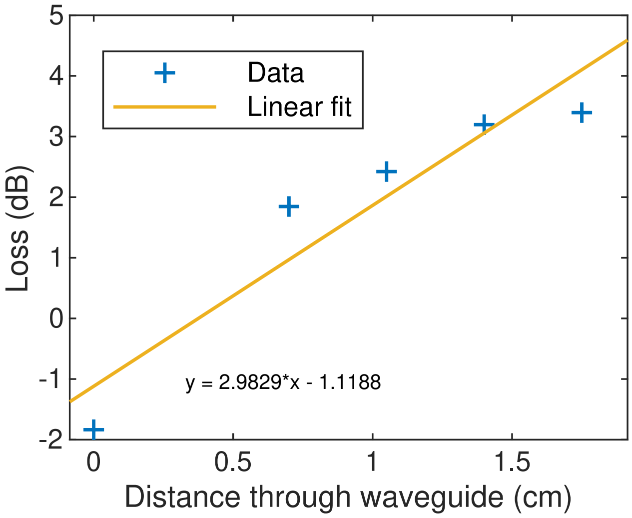

FIGURE 7.8: Bi-directional propagation loss data for IOF refractometer chip for use in the Rogers *et. al* method. A propagation loss of 2.98 dB/cm is calculated for this device.

waveguide diameter, for a given core width, as shown in the inset of figure 7.7(b). The result of this work is shown for a variety of thicknesses. At a refractive index of 1.456, the sensitivity of a leaky mode refractometer is displayed in figure 7.7(b). This provides a route to enhance the sensitivity of such a device.

The absolute propagation loss of this device could be quantified via the Rogers *et. al* [201] technique, in addition to the work presented in Ref. [123]. This is calculated via the ratio of the reflected power from either end of the waveguide for each grating. The relative power is the associated amplitude of a Gaussian fit to each grating. These values can be represented as a function of their location in the waveguide, figure 7.8. The propagation loss in dB/cm is the slope of a least-squares linear fit. A 2.98 dB/cm propagation loss is calculated for the waveguide used in the refractometry experiments. As this value is likely due to surface roughness or micro-bends in the etched fibre, it leads to the conclusion that HF etched optical fibre will not be a suitable method of creating low loss waveguides in this platform.

7.5 Conclusion

A method for refractometry for refractive indices above that of the waveguide's core has been presented. An etched IOF refractometer was fabricated with multiple FBGs as the method of quantifying propagation loss in the leaky mode waveguide. This enabled calibration of the device's response to a liquid analyte's refractive index. The device has shown a potential refractive index resolution in the order of 10^{-5}. Results from an approximated TMM simulation have presented a number of routes for development of the device. This form of etched IOF presents itself as a candidate for harsh environment sensing due to its inherent chemical stability as a purely Si/SiO_2 sensor. Future work will include an investigation into optical fibre extruding from the substrate for optimal device coupling without the need for glues. This will further develop the device's application in harsh environments and as a method for reduced coupling losses.

Chapter 8

Conclusions, Summary and Future Prospects

The preceding 7 chapters have discussed the motivation behind this work (Chapter 1), underlying theory and previous literature in this area (Chapters 2 and 3), and a collection of novel experimental research undertaken from 2017 to 2020; directly resulting in four journal publications. This research included: furthering the development of the Zn-indiffused PPLN ridge waveguides being developed here in the University of Southampton (Chapters 4 and 5); exploring the limitations of upconversion telecommunication systems using bulk crystal PPLN (Chapter 6); and a refractometer which was fabricated and characterised in a novel integrated optical fibre platform (Chapter 7). To conclude, a brief summary of this work and potential directions for future research will be discussed in the final sections of this thesis.

8.1 Short wavelength generation and characterisation of zinc-indiffused PPLN waveguides

The work presented in Chapter 4 is currently the shortest wavelength device demonstrated from the recently developed Zn-indiffused ridge waveguide technology at the University of Southampton. It was established that the 14 mm-long waveguide investigated displayed an effective nonlinear coefficient equal to the level of a third-order QPM grating. Without further advancements in the poling routine for LN domain reversal, third order devices will permit longer waveguides with consistent, uniform QPM gratings to establish their conversion efficiency. It is anticipated scattering effects along the side-walls of the ridge waveguide may start to play a limiting factor in UV generation, alongside the material absorption which would have been a dominant factor if pure LN was used. The individual benefits of doping LN with zinc or magnesium is known to shorten the cut-off wavelength for transmission but the combined effect has never been investigated.

Collaborative research to include a novel VECSEL structure as the pump source to seed the nonlinear process for blue/UV generation was successful. We reached optical powers up to 1 mW of 390 nm light. On-going research includes the development of an equivalent 739 nm, narrow-linewidth VECSEL source. Following development of the Zn-indiffused PPLN ridge waveguide with a QPM grating for this phasematching condition, there is potential for progress on current state-of-the-art 369 nm sources. In addition to this work, the Zn-indiffused PPLN ridge technology is mature enough to investigate its applicability as a 532 nm source, which will be implemented using 1^{st}-order gratings. Given the demonstration of high-damage thresholds in this optical platform [4], it is likely to demonstrate potential as a miniaturised competitor to the cavity-enhanced 532 nm sources which are usually used to pump laser gain materials, such as Ti:Sapphire or NIR VECSELs. Gaining an understanding of the impact of green induced IR absorption (GRIIRA), a well-known effect in $LiNbO_3$, on the conversion process in a zinc-doped, ridge waveguide will be vital in the applicability of this technology.

A data analysis route was presented in Chapter 5 for the application of studying the uniformity of ridge waveguides. This method capitalised on the finer details of white light interferometry, essentially permitting width data of the waveguide to be calculated from the lack of obtained data when the reflected data from the samples surface was outside of the numerical aperture of the collection lens. This method was successfully demonstrated but its true test in future work will be application to another large-mode nonlinear optical waveguides, such as KTP that has been fabricated by other research groups; perhaps of which has displayed an excessive challenge in troubleshooting the process flow.

8.2 Mid-infrared applications of PPLN

A PPLN-based upconversion system was designed, constructed and characterised for the application of MIR communication to test the performance of such an optical configuration where the receiver performs SFG and detects using a silicon APD. Bit error ratios (BER) of 10^{-7} were achieved but there is extensive room for improvement as current communication systems, which only utilise linear optics, routinely demonstrate BERs lower than 10^{-10}, even at untraditional spectral regions for communication [202]. It was noted in Chapter 6 that the electronic components available presented a certain limitation but the current error rates may be tolerable for industrial applications if the system had the added benefit of being miniaturised with a higher power efficiency, of which our research group is in a unique position to provide advancements towards this feat.

8.2.1 MIR PPLN waveguides

Future work in this research group will rely heavily upon the fabrication of novel MIR PPLN waveguides. This work will be carried out in collaboration with Covesion Ltd. While there have been previous demonstrations of MIR PPLN waveguides [53, 203], there is still no viable commercial product operating in this region. The are many technical reasons for this, primarily the sufficient overlap of the guided modes required for vastly different wavelengths. This a result of the DFG or SFG processes used, depending on whether it is required to act as the transmitter or receiver. However, while this task is certainly non-trivial, it would enable miniaturisation of these MIR communication systems.

Given the comparatively large mode sizes of this type of waveguide developed in this thesis and related work at Southampton to the competitor nano-LN waveguides a cohort of options may be available in the near future. This may include the development of fibre coupled MIR sources once safe optical filtering of the pump and signal wavelengths is achieved. The high damage threshold of the Zn-indiffused structures may also provide a commercially viable, integrated solution for optical parametric amplification which is still capable of high peak powers.

8.3 Integrated optical fibre

An integrated optical fibre platform has been successfully demonstrated as a refractometer for harsh environment applications. However, there are many potential routes to advance this optical platform, some of which have already been preliminarily demonstrated. To couple light into the device presented in Chapter 7, a UV-curable glue was used to join a v-groove assembly to the photonic chip. This glue is a point of weakness in a harsh environment, such as high temperature or chemically corrosive. Holmes *et al.* [204] presented the first example of the fibre coming off-chip. Developing a process which avoids glass degradation due to the high-temperatures used in the consolidation of

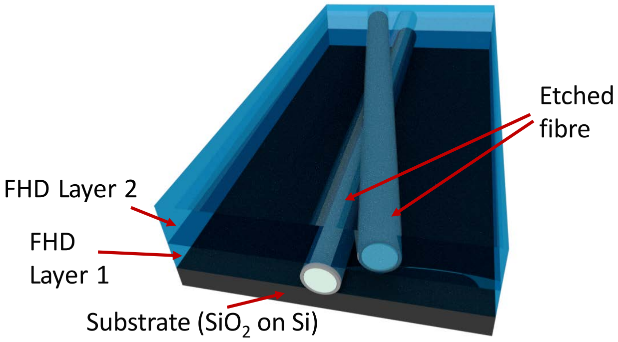

FIGURE 8.1: Conceptual image of a integrated coupler in the integrated fibre platform.

the planar glass layer, may allow for sufficient lengths of optical fibre to extrude off-chip to permit standard splicing techniques to be applied. This will allow for the seamless coupling of light into the device with many exciting research routes currently being investigated to enable this in the near future [205]. Other work to develop this platform will be the furthering of optical components such as integrated couplers. One route for this may be the use of cross-couplers, which are typically employed in integrated channel waveguide devices designed for quantum optical operations [192, 206, 207]. A conceptual image of how this may be fabricated is shown in figure 8.1 where chemically etched fibre embedded in deposited glass will permit evanescent field coupling between the fibre cores. Nevertheless, this is only one aspect of future work for this technology and there exists many other potential applications; even as far reaching as monitoring vibration in critical components [208].

Appendix A

Conference and journal publications

Gray, Alan Ciaran, Berry, Sam, Carpenter, Lewis Glynn, Gates, James, Gawith, Corin and Smith, Peter G R, Upconversion detection of 1.25 Gb/s mid-infrared telecommunications using a silicon avalanche photodiode. Optics Express, 2020 (Accepted)

A. C. Gray, S. A. Berry, L. G. Carpenter, J. C. Gates, C. B. E. Gawith and P. G. R. Smith, "Upconversion detection of 1.25 Gb/s Mid-IR telecommunications using a silicon avalanche photodiode," 2020 Conference on Lasers and Electro-Optics Pacific Rim (CLEO-PR), Sydney, Australia, 2020.

Carpenter, Lewis Glynn, Berry, Sam A, **Gray, Alan Ciaran**, Gates, James, Smith, Peter G R and Gawith, Corin, CW demonstration of SHG spectral narrowing in a PPLN waveguide generating 2.5 W at 780 nm. Optics Express, 28.15: 21382-21390, 2020.

Gray, Alan Ciaran, Carpenter, Lewis Glynn, Berry, Sam, Gates, James, Smith, Peter G R and Gawith, Corin. Investigation of PPLN waveguide uniformity via second harmonic generation spectra. IEEE Photonics Technology Letters, 32 (1), 63-66, 2020.

Gawith, Corin, Carpenter, Lewis Glynn, **Gray, Alan C.**, Smith, Peter G.R. and Berry, Sam, Watt-level 780 nm SHG in Zn indiffused MgO:PPLN ridge waveguides with 70% conversion efficiency. In SPIE Photonics West 2020.

Gray, Alan, Ciaran, Woods, Jonathan, Kahle, Hermann, Carpenter, Lewis Glynn, Berry, Sam, Tropper, Anne, Guina, Mircea, Apostolopoulos, Vasileios, Smith, Peter G.R. and Gawith, Corin, Zinc-indiffused MgO:PPLN waveguides for blue / UV generation via VECSEL pumping. Applied Optics, 59(16):4921-4926, 2020.

Gray, Alan Ciaran, Carpenter, Lewis Glynn, Berry, Sam A., Gates, James, Holmes, Christopher, Smith, Peter G.R. and Gawith, Corin (2019) Development of periodically poled lithium niobate zinc-indiffused ridge waveguides at blue wavelengths. Conference on Lasers and Electro-Optics Europe and European Quantum Electronics Conference, CLEO/Europe-EQEC 2019, ICM – International Congress Centre, Germany. 23 - 27 Jun 2019.

Jantzen, Senta Lisa, Bannerman, Rex, Jantzen, Alexander, Berry, Sam, **Gray, Alan Ciaran**, Gates, James, Boyd, Lewis, Smith, Peter G.R. and Holmes, Christopher, Integrated optical fibre – Investigating the vibrational response using optical frequency domain reflectometry. Conference on Lasers and Electro-Optics Europe; European Quantum Electronics Conference (CLEO/Europe-EQEC) 2019.

Carpenter, Lewis Glynn, Berry, Sam, Legg, Thomas H., Farries, M.C., Watson, Chloe, Bannerman, Rex, **Gray, Alan, Ciaran**, Holmes, Christopher, Gates, James, Smith, Peter G R and Gawith, Corin, Zn MgO PPLN waveguides for Rb cold atom trap based quantum gravitometry in a CubeSat. Conference on Lasers and Electro-Optics Europe and European Quantum Electronics Conference, OSA, 2019.

Berry, Sam, Carpenter, Lewis Glynn, **Gray, Alan, Ciaran**, Smith, Peter G.R. and Gawith, Corin, Zn-indiffused diced ridge waveguides in MgO:PPLN generating 1 watt 780 nm SHG at 70% efficiency. OSA Continuum, 2 (12), 3456-3464, 2019.

Carpenter, Lewis Glynn, Berry, Sam, Bannerman, Rex, **Gray, Alan, Ciaran** and Gawith, Corin, ZnO indiffused MgO:PPLN ridge waveguides. Optics Express, 27 (17), 24538-24544, 2019.

Gray, Alan, Ciaran, Jantzen, Alexander, Yoshikawa, Naruo, Gow, Paul C., Gawith, Corin, Smith, Peter and Holmes, Christopher (2018) An integrated optical fibre device for harsh environment refractometry at indices above silica for monitoring hydrocarbon fuels. SPIE Photonics West United States January 2018, San Francisco, United States. 26 Jan - 02 Feb, 2018.

Gow, Paul C., Jantzen, Alexander, Boyd, Keiron, Simakov, Nikita, Daniel, Jae, M.O., **Gray, Alan C.**, Gates, James C., Shardlow, Peter, Smith, Peter G.R. and Holmes, Christopher, Consolidation of flame hydrolysis deposited silica with a 9.3 µm wavelength CO2 laser. Electronics Letters, 54 (15), 945-947, 2018.

Carpenter, Lewis Glynn, Berry, Sam, Bannerman, Rex, **Gray, Alan Ciaran**, Field, James, Holmes, Christopher, Gates, James, Smith, Peter and Gawith, Corin (2018) Developing PPLN waveguides for quantum rubidium atom traps in space. Nonlinear Photonics (OSA, Advanced Photonics Congress), Zürich, Switzerland. 02 - 05 Jul 2018.

Holmes, C., Gow, P.C., Jantzen, A., **Gray, A.C.**, Scholl, S.L., Gates, J.C. and Smith, P.G.R., High temperature operation of integrated optical fiber. In Conference on Lasers and Electro-Optics/Pacific Rim, CLEO PR vol. Part F113-CLEOP, OSA, 2018.

Holmes, Christopher, Jantzen, Alexander, **Gray, Alan C.**, Lynch, Stephen G., Carpenter, Lewis G., Gow, Paul C., Gates, James C. and Smith, Peter G.R., Integrated optical fiber: A fresh approach to planar photonics. IEEE 7th International Conference on Photonics, ICP. Institute of Electrical and Electronics Engineers Inc, 2018.

Gray, Alan Ciaran, Jantzen, Alexander, Gow, P.C., Smith, Devin H., Gawith, Corin B.E., Smith, Peter G.R. and Holmes, Christopher, Leaky mode integrated optical fibre refractometer. Optics Express, 26 (7), 9155-9164, 2018.

Jantzen, Alexander, Gow, Paul C., **Gray, Alan**, Scholl, Senta, Gates, James, Smith, Peter, Boyd, Lewis and Holmes, Christopher (2018) Pressure sensing based on ratiometric Bragg grating loss in a planar silica diaphragm platform. OSA Advanced Photonics Congress, Zurich, Switzerland. 02-05 Jul, 2018.

Holmes, Christopher, Jantzen, Alexander, **Gray, Alan, Ciaran**, Gow, Paul C., Carpenter, Lewis Glynn, Bannerman, Rex, Gates, James and Smith, Peter, Evanescent field refractometry in planar optical fiber. Optics Letters, 43 (4), 791-794, [309889], 2017.

Holmes, Christopher, Jantzen, Alexander, **Gray, Alan C.**, Carpenter, Lewis, Gow, Paul C., Lynch, Stephen G., Gates, James and Smith, Peter, Integrated optical fiber-tip cantilevers. IEEE Sensors Journal, 17 (21), 6960-6965, 2017.

Appendix B

ZnO ALD fabrication

A simple process flow is presented in figure B.1 to fabricate planar waveguides via Zn-indiffusion in LN. In the development of waveguides for use in the SHG from 780 nm light, the mode field diameter (MFD) of these Zn-indiffused planar layers was investigated. This is similar to the research presented by Carpenter *et. al* [209]. The aim was to determine which deposition and annealing parameter set provided the greatest likelihood of a single-mode 780 nm waveguide with the smallest MFD in the y-axis.

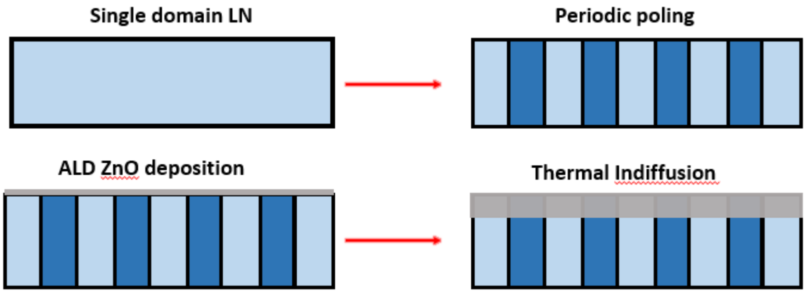

Figure B.1: Schematic diagram of the fabrication process flow to create LN waveguides.

A broadband source was utilised to characterize the planar Zn-indiffused LN waveguides. These had been fabricated by depositing a range of ZnO layer thicknesses via atomic layer deposition (ALD) and annealing for 1 hour in a range of temperatures. The final fabrication step to create ridge waveguides will be to utilise an ultra-precision dicing saw (Disco, DAD3430). MFD data was calculated via a Gaussian fit with the outer limit taken as $1/e^2$ of either side. Light was coupled into the planar layer via butt-coupling of SMF-28 optical fibre and imaged on a high resolution InGaAs camera. The system utilised to carry out this analysis is courtesy of Rex Bannerman. An example output from this data is shown in figure B.2.

All results associated with this investigation are presented in figure B.3. As expected, the increasing temperature increased the diffusivity of the ZnO layer and formed a larger

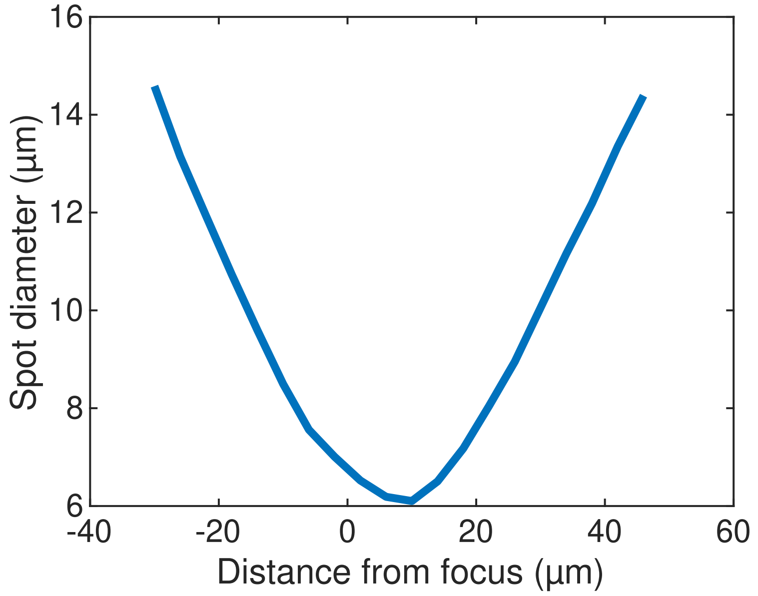

FIGURE B.2: Example data set from the MFD characterization of ZnO diffused LN waveguides. Data set represents the PPLN chip with a 120 nm layer ZnO layer, diffused at 800 °C for 1 hour.

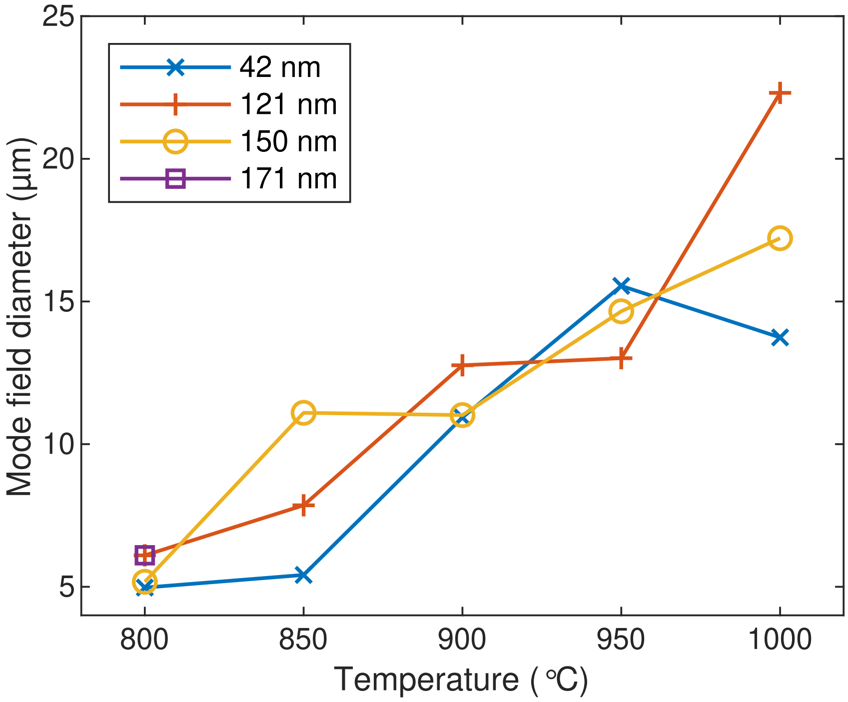

FIGURE B.3: Decreasing trend in the planar waveguide MFD observed as a function of furnace temperature utilised to diffuse the ZnO layer.

waveguide. This work suggests there is an optimal waveguiding layer in the region of 800-850 °C for ZnO layers of approximately 50-100 nm in thickness. These waveguides were single-mode and had an approximate MFD to that of commercial 780 nm optical fibre. The apparent independence of the MFD on ZnO thickness suggests that all layers were undepleted for this temperature and dwell time, i.e., a small amount of ZnO remained on top of the MgO:LN crystal.

However, after this work was carried out, numerous challenges have presented themselves with regards to the ALD layer of ZnO, preventing further development and testing of PPLN for SHG of 780 nm, in addition to the conclusion of the parallel research undertaken for 1560-780 nm SHG in this group using similar fabrication parameters, as presented by Carpenter *et al.*[103].

Bibliography

[1] Theodore H Maiman. Stimulated optical radiation in ruby. *Nature*, 187(4736):493–494, 1960.

[2] Richard P Feynman. Simulating physics with computers. *International Journal of Theoretical Physics*, 21(6/7), 1982.

[3] JA Armstrong, N Bloembergen, J Ducuing, and PS Pershan. Interactions between light waves in a nonlinear dielectric. *Physical review*, 127(6):1918, 1962.

[4] Lewis G Carpenter, Sam A Berry, Alan C Gray, James C Gates, Peter GR Smith, and Corin BE Gawith. CW demonstration of SHG spectral narrowing in a PPLN waveguide generating 2.5 W at 780 nm. *Optics Express*, 28(15):21382–21390, 2020.

[5] J. I. Cirac and P. Zoller. Quantum computations with cold trapped ions. *Phys. Rev. Lett.*, 74:4091–4094, May 1995.

[6] Ye Wang, Mark Um, Junhua Zhang, Shuoming An, Ming Lyu, Jing-Ning Zhang, L-M Duan, Dahyun Yum, and Kihwan Kim. Single-qubit quantum memory exceeding ten-minute coherence time. *Nature Photonics*, 11(10):646, 2017.

[7] Wayne M Itano, James C Bergquist, John J Bollinger, and David J Wineland. Laser cooling of trapped ions. *Proceedings of thes international school of physics" Enrico Fermi": Laser Manipulation of Atoms and Ions, Edité par North Holland*, page 519, 1992.

[8] David Kielpinski, Marko Cetina, JA Cox, and Franz X Kaertner. Laser cooling of trapped ytterbium ions with an ultraviolet diode laser. *Optics Letters*, 31(6):757–759, 2006.

[9] William Paul Risk, TR Gosnell, and AV Nurmikko. *Compact blue-green lasers.* Cambridge University Press, 2003.

[10] Sam A Berry, Lewis G Carpenter, Alan C Gray, Peter GR Smith, and Corin BE Gawith. Zn-indiffused diced ridge waveguides in MgO:PPLN generating 1 watt 780 nm SHG at 70% efficiency. *OSA Continuum*, 2(12):3456–3464, 2019.

[11] Cheng Wang, Carsten Langrock, Alireza Marandi, Marc Jankowski, Mian Zhang, Boris Desiatov, Martin M Fejer, and Marko Loncar. Ultrahigh-efficiency second-harmonic generation in nanophotonic PPLN waveguides. *arXiv preprint arXiv:1810.09235*, 2018.

[12] Lin Chang, Yifei Li, Nicolas Volet, Leiran Wang, Jon Peters, and John E Bowers. Thin film wavelength converters for photonic integrated circuits. *Optica*, 3(5):531–535, 2016.

[13] Luke Maidment, Peter G Schunemann, and Derryck T Reid. Molecular fingerprint-region spectroscopy from 5 to 12 µm using an orientation-patterned gallium phosphide optical parametric oscillator. *Optics Letters*, 41(18):4261–4264, 2016.

[14] Sebastian Wolf, Tobias Trendle, Jens Kiessling, Johannes Herbst, Karsten Buse, and Frank Kühnemann. Self-gated mid-infrared short pulse upconversion detection for gas sensing. *Optics Express*, 25(20):24459–24468, 2017.

[15] CK Hong, Zhe-Yu Ou, and Leonard Mandel. Measurement of subpicosecond time intervals between two photons by interference. *Physical Review Letters*, 59(18):2044, 1987.

[16] Jonathan CF Matthews, Alberto Politi, André Stefanov, and Jeremy L O'brien. Manipulation of multiphoton entanglement in waveguide quantum circuits. *Nature Photonics*, 3(6):346–350, 2009.

[17] Alberto Politi, Martin J. Cryan, John G. Rarity, Siyuan Yu, and Jeremy L. O'Brien. Silica-on-silicon waveguide quantum circuits. *Science*, 320(5876):646–649, 2008.

[18] Partha Pratim Sahu. Compact component for integrated quantum optic processing. *Scientific Reports*, 5:16276, 2015.

[19] Stephen G. Lynch, Christopher Holmes, Sam A. Berry, James C. Gates, Alexander Jantzen, Teresa I. Ferreiro, and Peter G. R. Smith. External cavity diode laser based upon an FBG in an integrated optical fiber platform. *Optics Express*, 24(8):8391–8398, Apr 2016.

[20] Stephen G Lynch. *Integrated planar cavities for external cavity diode lasers.* PhD thesis, University of Southampton, 2017.

[21] Christopher Holmes, James C Gates, Lewis G Carpenter, Helen L Rogers, Richard M Parker, Peter A Cooper, Sima Chaotan, Faisal R Mahamd Adikan, Corin B E Gawith, and Peter G R Smith. Direct UV-written planar Bragg grating sensors. *Measurement Science and Technology*, 26(11):112001, 2015.

[22] C Sima, JC Gates, HL Rogers, PL Mennea, C Holmes, MN Zervas, and Peter G R Smith. Ultra-wide detuning planar Bragg grating fabrication technique based on

direct UV grating writing with electro-optic phase modulation. *Optics Express*, 21(13):15747–15754, 2013.

[23] Robert W Boyd. *Nonlinear Optics*. Elsevier, 2003.

[24] DA Kleinman. Nonlinear dielectric polarization in optical media. *Physical Review*, 126(6):1977, 1962.

[25] Arlee V Smith. *Crystal nonlinear optics: with SNLO examples*. AS-Photonics, 2018.

[26] Yōichi Shiozaki and Toshio Mitsui. Powder neutron diffraction study of $LiNbO_3$. *Journal of Physics and Chemistry of Solids*, 24(8):1057–1061, 1963.

[27] Ichiro Shoji, Takashi Kondo, Ayako Kitamoto, Masayuki Shirane, and Ryoichi Ito. Absolute scale of second-order nonlinear-optical coefficients. *JOSA B*, 14(9):2268–2294, 1997.

[28] Robert C Miller. Optical second harmonic generation in piezoelectric crystals. *Applied Physics Letters*, 5(1):17–19, 1964.

[29] William J Alford and Arlee V Smith. Wavelength variation of the second-order nonlinear coefficients of $KNbO_3$, $KTiOPO_4$, $KTiOAsO_4$, $LiNbO_3$, $LiIO_3$, β-BaB_2O_4, KH_2PO_4, and LiB_3O_5 crystals: a test of Miller wavelength scaling. *JOSA B*, 18(4):524–533, 2001.

[30] RT Murray, TH Runcorn, S Guha, and JR Taylor. High average power parametric wavelength conversion at 3.31–3.48 µm in MgO:PPLN. *Optics Express*, 25(6):6421–6430, 2017.

[31] Toshiaki Suhara and Masatoshi Fujimura. *Waveguide nonlinear-optic devices*, volume 11. Springer Science & Business Media, 2003.

[32] Matthias Jäger, George I Stegeman, Marinus C Flipse, Mart Diemeer, and Guus Möhlmann. Modal dispersion phase matching over 7 mm length in overdamped polymeric channel waveguides. *Applied Physics Letters*, 69(27):4139–4141, 1996.

[33] W Wirges, S Yilmaz, W Brinker, S Bauer-Gogonea, S Bauer, M Jäger, GI Stegeman, M Ahlheim, M Stähelin, B Zysset, F. Lehr, M. Diemeer, and M. C. Flipse. Polymer waveguides with optimized overlap integral for modal dispersion phase-matching. *Applied Physics Letters*, 70(25):3347–3349, 1997.

[34] M Houe and PD Townsend. An introduction to methods of periodic poling for second-harmonic generation. *Journal of Physics D: Applied Physics*, 28(9):1747, 1995.

[35] Inrad Optics, BBO. https://www.inradoptics.com/bbo, last accessed on 22/06/20.

[36] LBO crystals. https://www.advatech-uk.co.uk/nlo_lbo.html, last accessed on 23/06/20.

[37] Konstantin L Vodopyanov, O Levi, PS Kuo, TJ Pinguet, JS Harris, MM Fejer, B Gerard, L Becouarn, and E Lallier. Optical parametric oscillation in quasi-phase-matched GaAs. *Optics Letters*, 29(16):1912–1914, 2004.

[38] L Gordon, GL Woods, RC Eckardt, RR Route, RS Feigelson, MM Fejer, and R Byer. Diffusion-bonded stacked GaAs for quasiphase-matched second-harmonic generation of a carbon dioxide laser. *Electronics Letters*, 29(22):1942–1944, 1993.

[39] MS Piltch, CD Cantrell, and RC Sze. Infrared second-harmonic generation in nonbirefringent cadmium telluride. *Journal of Applied Physics*, 47(8):3514–3517, 1976.

[40] Duan Feng, Nai-Ben Ming, Jing-Fen Hong, Yong-Shun Yang, Jin-Song Zhu, Zhen Yang, and Ye-Ning Wang. Enhancement of second-harmonic generation in $LiNbO_3$ crystals with periodic laminar ferroelectric domains. *Applied Physics Letters*, 37(7):607–609, 1980.

[41] A Feisst and P Koidl. Current induced periodic ferroelectric domain structures in $LiNbO_3$ applied for efficient nonlinear optical frequency mixing. *Applied Physics Letters*, 47(11):1125–1127, 1985.

[42] EJ Lim, MM Fejer, and RL Byer. Second-harmonic generation of green light in periodically poled planar lithium niobate waveguide. *Electronics Letters*, 25(3):174–175, 1989.

[43] G Rosenman, A Skliar, D Eger, M Oron, and M Katz. Low temperature periodic electrical poling of flux-grown $KTiOPO_4$ and isomorphic crystals. *Applied Physics Letters*, 73(25):3650–3652, 1998.

[44] A Arie, G Rosenman, V Mahal, A Skliar, M Oron, M Katz, and D Eger. Green and ultraviolet quasi-phase-matched second harmonic generation in bulk periodically-poled $KTiOPO_4$. *Optics Communications*, 142(4-6):265–268, 1997.

[45] Valdas Pasiskevicius, Shunhua Wang, Jens A Tellefsen, Fredrik Laurell, and Håkan Karlsson. Efficient Nd:YAG laser frequency doubling with periodically poled KTP. *Applied Optics*, 37(30):7116–7119, 1998.

[46] O Gayer, Z Sacks, E Galun, and A Arie. Temperature and wavelength dependent refractive index equations for MgO-doped congruent and stoichiometric $LiNbO_3$. *Applied Physics B*, 91(2):343–348, 2008.

[47] Katsunari Okamoto. *Fundamentals of optical waveguides*. Academic press, 2006.

[48] Ajoy Ghatak and K Thyagarajan. *An introduction to fiber optics*. Cambridge University Press, 1998.

[49] Christopher Holmes. *Direct UV written planar devices for sensing and telecommunication applications.* PhD thesis, University of Southampton, 2009.

[50] Benjamin D Snow. *Liquid crystal adaptive planar optical devices.* PhD thesis, University of Southampton, 2010.

[51] Huw E Major. *QPM grating design for novel PPLN structures.* PhD thesis, University of Southampton, 2009.

[52] J. M. Manley and H. E. Rowe. Some General Properties of Nonlinear Elements-Part I. General Energy Relations. *Proceedings of the IRE*, 44(7):904–913, 1956.

[53] Kai-Daniel F Büchter, Harald Herrmann, Carsten Langrock, Martin M Fejer, and Wolfgang Sohler. All-optical Ti:PPLN wavelength conversion modules for free-space optical transmission links in the mid-infrared. *Optics Letters*, 34(4):470–472, 2009.

[54] GD Boyd and DA Kleinman. Parametric interaction of focused Gaussian light beams. *Journal of Applied Physics*, 39(8):3597–3639, 1968.

[55] Shekhar Guha and Joel Falk. The effects of focusing in the three-frequency parametric upconverter. *Journal of Applied Physics*, 51(1):50–60, 1980.

[56] Teunis W Tukker, Cees Otto, and Jan Greve. Elliptical-focusing effect on parametric oscillation and downconversion. *JOSA B*, 15(9):2455–2461, 1998.

[57] Herwig Kogelnik and Tingye Li. Laser beams and resonators. *Applied Optics*, 5(10):1550–1567, 1966.

[58] Anthony E Siegman. Lasers university science books. *Mill Valley, CA*, 37(208):169, 1986.

[59] William T Silfvast. *Laser fundamentals.* Cambridge University Press, 2004.

[60] Rüdiger Paschotta. ABCD Matrix, Oct 2019.

[61] Robert C Miller. Optical Harmonic Generation in Single Crystal BaTiO$_3$. *Physical Review*, 134(5A):A1313, 1964.

[62] David S Hum and Martin M Fejer. Quasi-phasematching. *Comptes Rendus Physique*, 8(2):180–198, 2007.

[63] Georg Harder, Vahid Ansari, Benjamin Brecht, Thomas Dirmeier, Christoph Marquardt, and Christine Silberhorn. An optimized photon pair source for quantum circuits. *Optics Express*, 21(12):13975–13985, 2013.

[64] JL Tambasco, A Boes, LG Helt, MJ Steel, and A Mitchell. Domain engineering algorithm for practical and effective photon sources. *Optics Express*, 24(17):19616–19626, 2016.

[65] Georg Harder, Tim J Bartley, Adriana E Lita, Sae Woo Nam, Thomas Gerrits, and Christine Silberhorn. Single-mode parametric-down-conversion states with 50 photons as a source for mesoscopic quantum optics. *Physical Review Letters*, 116(14):143601, 2016.

[66] Sunil Mittal, Venkata Vikram Orre, Alessandro Restelli, Reza Salem, Elizabeth A Goldschmidt, and Mohammad Hafezi. Temporal and spectral manipulations of correlated photons using a time lens. *Physical Review A*, 96(4):043807, 2017.

[67] J.-P. Meyn and M. M. Fejer. Tunable ultraviolet radiation by second-harmonic generation in periodically poled lithium tantalate. *Optics Letters*, 22(16):1214–1216, Aug 1997.

[68] Kiminori Mizuuchi, Tomoya Sugita, Kazuhisa Yamamoto, Tatsuo Kawaguchi, Takeshi Yoshino, and Minoru Imaeda. Efficient 340-nm light generation by a ridge-type waveguide in a first-order periodically poled MgO:LiNbO$_3$. *Optics Letters*, 28(15):1344–1346, Aug 2003.

[69] Toshiharu Oka and Toshiaki Suhara. Annealed proton-exchanged waveguide quasi-phase-matched second-harmonic generation devices in 8 mol% mgo-doped congruent LiTaO$_3$ crystal. *Japanese Journal of Applied Physics*, 54(10):100304, 2015.

[70] Qiang Fu, Lin Xu, Sijing Liang, PC Shardlow, DP Shepherd, S-U Alam, and DJ Richardson. High-beam-quality, watt-level, widely tunable, mid-infrared op-gaas optical parametric oscillator. *Optics Letters*, 44(11):2744–2747, 2019.

[71] BC Grabmaier and F Otto. Growth and investigation of MgO-doped LiNbO$_3$. *Journal of Crystal Growth*, 79(1-3):682–688, 1986.

[72] Majid Ebrahim-Zadeh, Suddapalli Chaitanya Kumar, and Kavita Devi. Yb-fiber-laser-pumped continuous-wave frequency conversion sources from the mid-infrared to the ultraviolet. *IEEE Journal of Selected Topics in Quantum Electronics*, 20(5):350–372, 2014.

[73] Olivier Alibart, Virginia D'Auria, Marc De Micheli, Florent Doutre, Florian Kaiser, Laurent Labonté, Tommaso Lunghi, Éric Picholle, and Sébastien Tanzilli. Quantum photonics at telecom wavelengths based on lithium niobate waveguides. *Journal of Optics*, 18(10):104001, 2016.

[74] Jonas Webjorn, V Pruneri, P St J Russell, JRM Barr, and DC Hanna. Quasi-phase-matched blue light generation in bulk lithium niobate, electrically poled via periodic liquid electrodes. *Electronics Letters*, 30(11):894–895, 1994.

[75] Corin Barry Edmund Gawith, Peter George Robin Smith, and Huw Edward Major. Process for poling a ferroelectric material doped with a metal, November 22 2011. US Patent 8,064,129.

[76] NANOLN. https://www.nanoln.com/PRODUCTS_128978.htmlcomp-maeh1ti8, last accessed on 22/06/20.

[77] Mohammadreza Younesi, Pawan Kumar, Badrudin Jakob Stanicki, Reinhard Geiss, Wei-Kun Chang, Yen-Hung Chen, Frank Setzpfandt, and Thomas Pertsch. Periodic poling with short period for thin film lithium niobate waveguides. In *2019 Conference on Lasers and Electro-Optics Europe & European Quantum Electronics Conference (CLEO/Europe-EQEC)*, pages 1–1. IEEE, 2019.

[78] Thomas A Wright, Robert JA Francis-Jones, Corin BE Gawith, Jonas N Becker, Patrick M Ledingham, Peter GR Smith, Joshua Nunn, Peter J Mosley, Benjamin Brecht, and Ian A Walmsley. Two-way photonic interface for linking the Sr^+ transition at 422 nm to the telecommunication C band. *Physical Review Applied*, 10(4):044012, 2018.

[79] Covesion Ltd. - MgO:PPLN for second harmonic generation. https://www.covesion.com/products/magnesium-doped-ppln-mgoppln-crystals/mgo-ppln-for-second-harmonic-generation/, last accessed on 04/06/20.

[80] HC Photonics corp. - PPLN. https://www.hcphotonics.com/portfolio/items/443978, last accessed on 01/06/20.

[81] Corin BE Gawith. *Novel active waveguide devices in direct-bonded structures.* PhD thesis, University of Southampton, 2002.

[82] R. Regener and W. Sohler. Efficient second-harmonic generation in Ti:$LiNbO_3$ channel waveguide resonators. *J. Opt. Soc. Am. B*, 5(2):267–277, Feb 1988.

[83] JL Jackel and CE Rice. Topotactic $LiNbO_3$ to cubic perovskite structural transformation in $LiNbO_3$ and $LiTaO_3$. *Ferroelectrics*, 38(1):801–804, 1981.

[84] Janet L Jackel, CE Rice, and JJ Veselka. Proton exchange for high-index waveguides in $LiNbO_3$. *Applied Physics Letters*, 41(7):607–608, 1982.

[85] Fredrik Laurell, MG Roelofs, and H Hsiung. Loss of optical nonlinearity in proton-exchanged $LiNbO_3$ waveguides. *Applied Physics Letters*, 60(3):301–303, 1992.

[86] DF Clark, ACG Nutt, KK Wong, PJR Laybourn, and RM De La Rue. Characterization of proton-exchange slab optical waveguides in z-cut LiNbO3. *Journal of Applied Physics*, 54(11):6218–6220, 1983.

[87] Mauro Varasi, Antonello Vanucci, and Mario Signorazzi. Lithium niobate proton-exchange technology for phase-amplitude modulators. In *Integrated Optical Circuits*, volume 1583, pages 165–169. International Society for Optics and Photonics, 1991.

[88] KK Wong, RM De La Rue, and S Wright. Electro-optic-waveguide frequency translator in $LiNbO_3$ fabricated by proton exchange. *Optics Letters*, 7(11):546–548, 1982.

[89] PG Suchoski, Talal K Findakly, and FJ Leonberger. Stable low-loss proton-exchanged $LiNbO_3$ waveguide devices with no electro-optic degradation. *Optics Letters*, 13(11):1050–1052, 1988.

[90] Krishnan R Parameswaran, Roger K Route, Jonathan R Kurz, Rostislav V Roussev, Martin M Fejer, and Masatoshi Fujimura. Highly efficient second-harmonic generation in buried waveguides formed by annealed and reverse proton exchange in periodically poled lithium niobate. *Optics Letters*, 27(3):179–181, 2002.

[91] M. L. Bortz, L. A. Eyres, and M. M. Fejer. Depth profiling of the d33 nonlinear coefficient in annealed proton exchanged $LiNbO_3$ waveguides. *Applied Physics Letters*, 62(17):2012–2014, 1993.

[92] Shantanu Pal, Bijoy Krishna Das, and Wolfgang Sohler. Photorefractive damage resistance in Ti:PPLN waveguides with ridge geometry. *Applied Physics B*, 120(4):737–749, 2015.

[93] Edvard P Kokanyan, Luca Razzari, Ilaria Cristiani, Vittorio Degiorgio, and John B Gruber. Reduced photorefraction in hafnium-doped single-domain and periodically poled lithium niobate crystals. *Applied Physics Letters*, 84(11):1880–1882, 2004.

[94] TR Volk and NM Rubinina. A new optical damage resistant impurity in lithium niobate crystals: indium. *Ferroelectrics Letters Section*, 14(1-2):37–43, 1992.

[95] T Volk, M Wöhlecke, N Rubinina, NV Razumovski, F Jermann, C Fischer, and R Böwer. $LiNbO_3$ with the damage-resistant impurity indium. *Applied Physics A*, 60(2):217–225, 1995.

[96] Joyce K Yamamoto, Kenji Kitamura, Nobuo Iyi, Shigeyuki Kimura, Yasunori Furukawa, and Masayoshi Sato. Increased optical damage resistance in Sc_2O_3-doped $LiNbO_3$. *Applied Physics Letters*, 61(18):2156–2158, 1992.

[97] Yongfa Kong, Shiguo Liu, Yanjun Zhao, Hongde Liu, Shaolin Chen, and Jingjun Xu. Highly optical damage resistant crystal: Zirconium-oxide-doped lithium niobate. *Applied Physics Letters*, 91(8):081908, 2007.

[98] WM Young, Martin M Fejer, Michel JF Digonnet, AF Marshall, and RS Feigelson. Fabrication, characterization and index profile modeling of high-damage resistance Zn-diffused waveguides in congruent and MgO:lithium niobate. *Journal of Lightwave Technology*, 10(9):1238–1246, 1992.

[99] Lu Ming, Corin BE Gawith, Katia Gallo, Martin V O'Connor, Gregory D Emmerson, and Peter GR Smith. High conversion efficiency single-pass second harmonic

generation in a zinc-diffused periodically poled lithium niobate waveguide. *Optics Express*, 13(13):4862–4868, 2005.

[100] R Nevado, C Sada, F Segato, F Caccavale, A Kling, JC Soares, E Cantelar, F Cusso, and G Lifante. Compositional characterisation of Zn-diffused lithium niobate waveguides. *Applied Physics B*, 73(5-6):555–558, 2001.

[101] L Aghli-Moghadam, A Baghizadeh, G Nabiyouni, A Farashiani, and A Zendehnam. Zn-diffused $LiNbO_3$ waveguides fabricated by DC magnetron sputtering. *Applied Physics A*, 97(4):805, 2009.

[102] R Nevado and G Lifante. Low-loss, damage-resistant optical waveguides in zn-diffused LiNbO3 by a two-step procedure. *Applied Physics A*, 72(6):725–728, 2001.

[103] Lewis Glynn Carpenter, Sam A Berry, Rex H S Bannerman, Alan C Gray, and Corin B E Gawith. ZnO indiffused MgO:PPLN ridge waveguides. *Optics Express*, 27(17):24538–24544, 2019.

[104] Ye Zhang, YH Xu, MH Li, and YQ Zhao. Growth and properties of Zn doped lithium niobate crystal. *Journal of crystal growth*, 233(3):537–540, 2001.

[105] TR Volk, MA Ivanov, VI Pryalkin, and NM Rubinina. Photorefractive and nonlinear-optical properties of optical damage resistant $LiNbO_3$: Zn crystals. *Ferroelectrics*, 126(1):57–62, 1992.

[106] Robin C Sterling, Hwanjit Rattanasonti, Sebastian Weidt, Kim Lake, Prasanna Srinivasan, SC Webster, Michaël Kraft, and Winfried K Hensinger. Fabrication and operation of a two-dimensional ion-trap lattice on a high-voltage microchip. *Nature communications*, 5(1):1–6, 2014.

[107] Steve Olmschenk, Kelly C Younge, David L Moehring, Dzmitry N Matsukevich, Peter Maunz, and Christopher Monroe. Manipulation and detection of a trapped Yb^+ hyperfine qubit. *Physical Review A*, 76(5):052314, 2007.

[108] S Mulholland, HA Klein, GP Barwood, S Donnellan, PBR Nisbet-Jones, G Huang, G Walsh, PEG Baird, and P Gill. Compact laser system for a laser-cooled ytterbium ion microwave frequency standard. *Review of Scientific Instruments*, 90(3):033105, 2019.

[109] Sachin Kasture, Francesco Lenzini, Ben Haylock, Andreas Boes, Arnan Mitchell, Erik W Streed, and Mirko Lobino. Frequency conversion between UV and telecom wavelengths in a lithium niobate waveguide for quantum communication with Yb^+ trapped ions. *Journal of Optics*, 18(10):104007, 2016.

[110] K. Mizuuchi, A. Morikawa, T. Sugita, K. Yamamoto, N. Pavel, and T. Taira. Continuous-wave ultraviolet generation at 354nm in a periodically poled

MgO:$LiNbO_3$ by frequency tripling of a diode end-pumped nd:gdvo4 microlaser. *Applied Physics Letters*, 85(18):3959–3961, 2004.

[111] Christopher D Wallace, Timothy P Dinneen, Kit-Yan N Tan, Timothy T Grove, and Phillip L Gould. Isotopic difference in trap loss collisions of laser cooled rubidium atoms. *Physical Review Letters*, 69(6):897, 1992.

[112] R Guckert, X Zhao, SG Crane, A Hime, WA Taylor, D Tupa, DJ Vieira, and H Wollnik. Magneto-optical trapping of radioactive 82 rb atoms. *Physical Review A*, 58(3):R1637, 1998.

[113] Leonardo Ricci, Matthias Weidemüller, Tilman Esslinger, Andreas Hemmerich, Claus Zimmermann, Vladan Vuletic, Wolfgang König, and Theodor W Hänsch. A compact grating-stabilized diode laser system for atomic physics. *Optics Communications*, 117(5-6):541–549, 1995.

[114] Alan C Gray, Jonathan RC Woods, Lewis G Carpenter, Hermann Kahle, Sam A Berry, Anne C Tropper, Mircea Guina, Vasilis Apostolopoulos, Peter G R Smith, and Corin B E Gawith. Zinc-indiffused MgO:PPLN waveguides for blue/UV generation via VECSEL pumping. *Applied Optics*, 59(16):4921–4926, 2020.

[115] Lewis Carpenter. *Precision dicing and micromilling of silica for photonics.* PhD thesis, University of Southampton, 2013.

[116] H Eda. Ductile grinding of ceramics: Machine tool and process. In *Handbook of advanced ceramics machining*, pages 15–42. CRC Press, 2006.

[117] T. G. Bifano, T. A. Dow, and R. O. Scattergood. Ductile-Regime Grinding: A New Technology for Machining Brittle Materials. *Journal of Engineering for Industry*, 113(2):184–189, 05 1991.

[118] Lewis G Carpenter, Helen L Rogers, Peter A Cooper, Christopher Holmes, James C Gates, and Peter GR Smith. Low optical-loss facet preparation for silica-on-silicon photonics using the ductile dicing regime. *Journal of Physics D: Applied Physics*, 46(47):475103, 2013.

[119] LG Carpenter, SA Berry, and CBE Gawith. Ductile dicing of $LiNbO_3$ ridge waveguide facets to achieve 0.29 nm surface roughness in single process step. *Electronics Letters*, 53(25):1672–1674, 2017.

[120] Rongbo Wu, Min Wang, Jian Xu, Jia Qi, Wei Chu, Zhiwei Fang, Jianhao Zhang, Junxia Zhou, Lingling Qiao, Zhifang Chai, Jintian Lin, and Ya Cheng. Long low-loss-litium niobate on insulator waveguides with sub-nanometer surface roughness. *Nanomaterials*, 8(11):910, 2018.

[121] Peter A Cooper, Lewis G Carpenter, Paolo L Mennea, Christopher Holmes, James C Gates, and Peter GR Smith. Integrated optical dual-cantilever arrays in silica on silicon. *Optics Express*, 22(26):31801–31813, 2014.

[122] C. Holmes, A. Jantzen, A. C. Gray, L. G. Carpenter, P. C. Gow, S. G. Lynch, J. C. Gates, and P. G. R. Smith. Integrated optical fiber-tip cantilevers. *IEEE Sensors Journal*, 17(21):6960–6965, Nov 2017.

[123] Alan C Gray, Alexander Jantzen, Paul C Gow, Devin H Smith, Corin BE Gawith, Peter GR Smith, and Christopher Holmes. Leaky mode integrated optical fibre refractometer. *Optics Express*, 26(7):9155–9164, 2018.

[124] Matthew T Posner, Thomas Hiemstra, Paolo L Mennea, Rex HS Bannerman, Ulrich B Hoff, Andreas Eckstein, W Steven Kolthammer, Ian A Walmsley, Devin H Smith, James C Gates, and Peter G. R. Smith. High-birefringence direct UV-written waveguides for use as heralded single-photon sources at telecommunication wavelengths. *Optics Express*, 26(19):24678–24686, 2018.

[125] Rex H S Bannerman. *Microfabrication of Waveguide-Based Devices for Quantum Optics*. PhD thesis, University of Southampton, 2019.

[126] Lasers and laser-related equipment. Test methods for laser beam widths, divergence angles and beam propagation ratios. Stigmatic and simple astigmatic beams. Standard, British Standard, 2005.

[127] Basic knowledge for using the sem. https://www.jeol.co.jp/en/applications/detail/891.html, JEOL Ltd.

[128] Martin M Fejer, GA Magel, Dieter H Jundt, and Robert L Byer. Quasi-phase-matched second harmonic generation: tuning and tolerances. *IEEE J. Quantum Electron*, 28(11):2631–2654, 1992.

[129] Sidney A Self. Focusing of spherical Gaussian beams. *Applied Optics*, 22(5):658–661, 1983.

[130] AC Tropper and S Hoogland. Extended cavity surface-emitting semiconductor lasers. *Progress in Quantum Electronics*, 30(1):1–43, 2006.

[131] ZL Liau. Semiconductor wafer bonding via liquid capillarity. *Applied Physics Letters*, 77(5):651–653, 2000.

[132] Krishnan R Parameswaran, Jonathan R Kurz, Rostislav V Roussev, and Martin M Fejer. Observation of 99% pump depletion in single-pass second-harmonic generation in a periodically poled lithium niobate waveguide. *Optics Letters*, 27(1):43–45, 2002.

[133] Christof Eigner, Matteo Santandrea, Laura Padberg, Martin F Volk, Christian E Rüter, Harald Herrmann, Detlef Kip, and Christine Silberhorn. Periodically poled ridge waveguides in KTP for second harmonic generation in the UV regime. *Optics Express*, 26(22):28827–28833, 2018.

[134] Takeshi Umeki, Osamu Tadanaga, and Masaki Asobe. Highly efficient wavelength converter using direct-bonded PPZnLN ridge waveguide. *IEEE J. Quantum Electron.*, 46(8):1206–1213, 2010.

[135] James D Franson. Bell inequality for position and time. *Physical Review Letters*, 62(19):2205, 1989.

[136] Andreas Eckstein, Guillaume Boucher, Aristide Lemaître, Pascal Filloux, Ivan Favero, Giuseppe Leo, John E Sipe, Marco Liscidini, and Sara Ducci. High-resolution spectral characterization of two photon states via classical measurements. *Laser & Photonics Reviews*, 8(5), 2014.

[137] Bin Fang, Offir Cohen, Marco Liscidini, John E Sipe, and Virginia O Lorenz. Fast and highly resolved capture of the joint spectral density of photon pairs. *Optica*, 1(5):281–284, 2014.

[138] Alfred B U'Ren, Christine Silberhorn, Reinhard Erdmann, Konrad Banaszek, Warren P Grice, Ian A Walmsley, and Michael G Raymer. Generation of pure-state single-photon wavepackets by conditional preparation based on spontaneous parametric downconversion. *arXiv preprint quant-ph/0611019*, 2006.

[139] Peter J Mosley, Jeff S Lundeen, Brian J Smith, Piotr Wasylczyk, Alfred B U'Ren, Christine Silberhorn, and Ian A Walmsley. Heralded generation of ultrafast single photons in pure quantum states. *Physical Review Letters*, 100(13):133601, 2008.

[140] Sam A Berry, Lewis G Carpenter, James C Gates, Peter GR Smith, and Corin BE Gawith. Zinc indiffused diced ridge ppln waveguides for photorefractive damage resistance and spectral engineering. In *The European Conference on Lasers and Electro-Optics*, page cj_6_5. Optical Society of America, 2019.

[141] Mathieu Chauvet, Fabien Henrot, Florent Bassignot, Fabrice Devaux, Ludovic Gauthier-Manuel, Vincent Pêcheur, Hervé Maillotte, and Brahim Dahmani. High efficiency frequency doubling in fully diced $\mathrm{LiNbO_3}$ ridge waveguides on silicon. *Journal of Optics*, 18(8):085503, 2016.

[142] Matteo Santandrea, Michael Stefszky, and Christine Silberhorn. General framework for the analysis of imperfections in nonlinear systems. *Optics Letters*, 44(22):5398–5401, 2019.

[143] Matteo Santandrea, Michael Stefszky, Vahid Ansari, and Christine Silberhorn. Fabrication limits of waveguides in nonlinear crystals and their impact on quantum optics applications. *New Journal of Physics*, 21(3):033038, 2019.

[144] Derek Chang, Carsten Langrock, Yu-Wei Lin, CR Phillips, CV Bennett, and Martin M Fejer. Complex-transfer-function analysis of optical-frequency converters. *Optics Letters*, 39(17):5106–5109, 2014.

[145] Pavel Pavlicek. Height profile measurement by means of white light interferometry. In *13th Polish-Czech-Slovak Conference on Wave and Quantum Aspects of Contemporary Optics*, volume 5259, pages 139–144. International Society for Optics and Photonics, 2003.

[146] Kieran G Larkin. Efficient nonlinear algorithm for envelope detection in white light interferometry. *JOSA A*, 13(4):832–843, 1996.

[147] Nathan Ida and Norbert Meyendorf. *Handbook of advanced nondestructive evaluation*. Springer International Publishing, 2019.

[148] John Canny. A computational approach to edge detection. In *Readings in computer vision*, pages 184–203. Elsevier, 1987.

[149] Judith MS Prewitt. Object enhancement and extraction. *Picture processing and Psychopictorics*, 10(1):15–19, 1970.

[150] Yuen-Ron Shen. The principles of nonlinear optics. *New York, Wiley-Interscience, 1984, 575 p.*, 1984.

[151] Georg Rademacher, Ruben S Luís, Benjamin J Puttnam, Tobias A Eriksson, Roland Ryf, Erik Agrell, Ryo Maruyama, Kazuhiko Aikawa, Yoshinari Awaji, Hideaki Furukawa, and Naoya Wada. High capacity transmission with few-mode fibers. *Journal of Lightwave Technology*, 37(2):425–432, 2018.

[152] Zhixin Liu, Boris Karanov, Lidia Galdino, John R Hayes, Domaniç Lavery, Kari Clark, Kai Shi, Daniel J Elson, Benn Charles Thomsen, Marco N Petrovich, D. J. Richardson, F. Poletti, R. Slavík, and P. Bayvel. Nonlinearity-free coherent transmission in hollow-core antiresonant fiber. *Journal of Lightwave Technology*, 37(3):909–916, 2018.

[153] Yong Chen, Zhixin Liu, Seyed R Sandoghchi, Gregory T Jasion, Tom D Bradley, Eric Numkam Fokoua, John R Hayes, Natalie V Wheeler, David R Gray, Brian J Mangan, Radan Slavík, Francesco Poletti, Marco N. Petrovich, and David J. Richardson. Multi-kilometer long, longitudinally uniform hollow core photonic bandgap fibers for broadband low latency data transmission. *Journal of Lightwave Technology*, 34(1):104–113, 2016.

[154] Jian Wang, Jeng-Yuan Yang, Irfan M Fazal, Nisar Ahmed, Yan Yan, Hao Huang, Yongxiong Ren, Yang Yue, Samuel Dolinar, Moshe Tur, and Alan Willner. Terabit free-space data transmission employing orbital angular momentum multiplexing. *Nature Photonics*, 6(7):488, 2012.

[155] Giovanni Milione, Martin PJ Lavery, Hao Huang, Yongxiong Ren, Guodong Xie, Thien An Nguyen, Ebrahim Karimi, Lorenzo Marrucci, Daniel A Nolan, Robert R Alfano, et al. 4×20 Gbit/s mode division multiplexing over free space using vector modes and a q-plate mode (de) multiplexer. *Optics Letters*, 40(9):1980–1983, 2015.

[156] Hao Huang, Guodong Xie, Yan Yan, Nisar Ahmed, Yongxiong Ren, Yang Yue, Dvora Rogawski, Moshe J Willner, Baris I Erkmen, Kevin M Birnbaum, Samuel J. Dolinar, Martin P. J. Lavery, Miles J. Padgett, Moshe Tur, and Alan E. Willner. 100 Tbit/s free-space data link enabled by three-dimensional multiplexing of orbital angular momentum, polarization, and wavelength. *Optics Letters*, 39(2):197–200, 2014.

[157] In Keun Son and Shiwen Mao. A survey of free space optical networks. *Digital communications and networks*, 3(2):67–77, 2017.

[158] Alan E Willner, Yongxiong Ren, Guodong Xie, Yan Yan, Long Li, Zhe Zhao, Jian Wang, Moshe Tur, Andreas F Molisch, and Solyman Ashrafi. Recent advances in high-capacity free-space optical and radio-frequency communications using orbital angular momentum multiplexing. *Philosophical Transactions of the Royal Society A: Mathematical, Physical and Engineering Sciences*, 375(2087):20150439, 2017.

[159] Yulong Su, Wei Wang, Xiaohong Hu, Hui Hu, Xinning Huang, Yishan Wang, Jinhai Si, Xiaoping Xie, Biao Han, Huan Feng, et al. 10 Gbps DPSK transmission over free-space link in the mid-infrared. *Optics express*, 26(26):34515–34528, 2018.

[160] Thermopile sensors, excelitas technologies corp. https://www.maximintegrated.com/ en/design/technical-documents/ app-notes/3/3470.html.

[161] Antonio Rogalski. *Infrared detectors.* CRC press, 2010.

[162] Qi Hu, Jeppe Seidelin Dam, Christian Pedersen, and Peter Tidemand-Lichtenberg. High-resolution mid-ir spectrometer based on frequency upconversion. *Optics Letters*, 37(24):5232–5234, 2012.

[163] Nicholas M Davis, SG Lynch, JC Gates, Jane Hodgkinson, PGR Smith, and Ralph P Tatam. Spectroscopic gas detection using a Bragg grating-stabilized external cavity laser, custom written in planar integrated silica-on-silicon. *Optics Express*, 27(20):29034–29044, 2019.

[164] Max Widarsson, Markus Henriksson, Patrick Mutter, Carlota Canalias, Valdas Pasiskevicius, and Fredrik Laurell. High resolution and sensitivity up-conversion mid-infrared photon-counting LIDAR. *Applied Optics*, 59(8):2365–2369, 2020.

[165] Jeppe Seidelin Dam, Peter Tidemand-Lichtenberg, and Christian Pedersen. Room-temperature mid-infrared single-photon spectral imaging. *Nature photonics*, 6(11):788–793, 2012.

[166] Huafang Dong, Haifeng Pan, Yao Li, E Wu, and Heping Zeng. Efficient single-photon frequency upconversion at 1.06 µm with ultralow background counts. *Applied Physics Letters*, 93(7):071101, 2008.

[167] Ajanta Barh, Peter Tidemand-Lichtenberg, and Christian Pedersen. Thermal noise in mid-infrared broadband upconversion detectors. *Optics Express*, 26(3):3249–3259, 2018.

[168] Laurent Huot, Peter Morten Moselund, Peter Tidemand-Lichtenberg, Lasse Leick, and Christian Pedersen. Upconversion imaging using an all-fiber supercontinuum source. *Optics Letters*, 41(11):2466–2469, 2016.

[169] Lasse Høgstedt, Andreas Fix, Martin Wirth, Christian Pedersen, and Peter Tidemand-Lichtenberg. Upconversion-based lidar measurements of atmospheric CO_2. *Optics Express*, 24(5):5152–5161, 2016.

[170] Pavel Polynkin, Rostislav Roussev, MM Fejer, N Peyghambarian, and Jerome Moloney. Laser transmitter for undersea communications using third-harmonic generation of fiber-laser system at 1.5 µm. *IEEE Photonics Technology Letters*, 19(17):1328–1330, 2007.

[171] Vincent J Urick, Preetpaul S Devgan, Jason D McKinney, and James L Dexter. Laser noise and its impact on the performance of intensity-modulation with direct-detection analog photonic links. Technical report, NAVAL RESEARCH LAB WASHINGTON DC OPTICAL SCIENCES DIV, 2007.

[172] Joseph M Singley, John Diehl, and Vincent J Urick. Characterization of lasers for use in analog photonic links. Technical report, NAVAL RESEARCH LAB WASHINGTON DC, 2011.

[173] Eagleyard Photonics. Relative intensity noise of distributed feedback lasers. *Application note. URL http://www. eagleyard. com/fileadmin/downloads/app_notes/app_note_rin_1-5. pdf.*

[174] Harry Nyquist. Thermal agitation of electric charge in conductors. *Physical Review*, 32(1):110, 1928.

[175] John Bertrand Johnson. Thermal agitation of electricity in conductors. *Physical review*, 32(1):97, 1928.

[176] Peter J Winzer. Shot-noise formula for time-varying photon rates: a general derivation. *JOSA B*, 14(10):2424–2429, 1997.

[177] P Horowitz. The art of electronics–3rd edition. *Horowitz W. Hill–NY.: Cambrige University Press, 2015.–1192 p*, 2015.

[178] HFAN-09.1.0: Impact of Transmitter RIN on Optical Link performance. https://pdfserv.maximintegrated.com/en/an/AN3470.pdf.

[179] David Large and James Farmer. Broadband cable access networks. *The HFC Plant*, 2009.

[180] S Bartalini, S Borri, I Galli, G Giusfredi, D Mazzotti, T Edamura, N Akikusa, M Yamanishi, and P De Natale. Measuring frequency noise and intrinsic linewidth of a room-temperature DFB quantum cascade laser. *Optics Express*, 19(19):17996–18003, 2011.

[181] Ghaya Baili, Loïc Morvan, Grégoire Pillet, Sophie Bouchoule, Zhuang Zhao, Jean-Louis Oudar, Loïc Ménager, Stéphane Formont, Frédéric Van Dijk, Mickaël Faugeron, Mehdi Alouini, Fabien Bretenaker, and Daniel Dolfi. Ultralow noise and high-power vecsel for high dynamic range and broadband rf/optical links. *Journal of Lightwave Technology*, 32(20):3489–3494, 2014.

[182] Mahmoud Tawfieq, Anders Kragh Hansen, Ole Bjarlin Jensen, Dominik Marti, Bernd Sumpf, and Peter E Andersen. Intensity noise transfer through a diode-pumped titanium sapphire laser system. *IEEE Journal of Quantum Electronics*, 54(1):1–9, 2017.

[183] Advantest Corporation. https://www.advantest.com/, last accessed on 22/07/20.

[184] Anders Kragh Hansen, Mahmoud Tawfieq, Ole Bjarlin Jensen, Peter E Andersen, Bernd Sumpf, G Erbert, and Paul Michael Petersen. Concept for power scaling second harmonic generation using a cascade of nonlinear crystals. *Optics Express*, 23(12):15921–15934, 2015.

[185] A Smith. SNLO software package. *www. as-photonics. com*, 2008.

[186] Optical Receiver, Newport corporation, 320-1000 nm Silicon detector, 30 khz to 1 GHz bandwidth.

[187] C. Holmes, A. Jantzen, A. C. Gray, S. G. Lynch, L. G. Carpenter, P. C. Gow, J. C. Gates, and P. G. R. Smith. Integrated Optical Fiber: A Fresh Approach to Planar Photonics. In *2018 IEEE 7th International Conference on Photonics (ICP)*, pages 1–3, 2018.

[188] Brice Calkins, Paolo L Mennea, Adriana E Lita, Benjamin J Metcalf, W Steven Kolthammer, Antia Lamas-Linares, Justin B Spring, Peter C Humphreys, Richard P Mirin, James C Gates, Peter G. R. Smith, Ian A. Walmsley, Thomas Gerrits, and Sae Woo Nam. High quantum-efficiency photon-number-resolving detector for photonic on-chip information processing. *Optics Express*, 21(19):22657–22670, 2013.

[189] Christopher Holmes, James C. Gates, and Peter G. R. Smith. Planarised optical fiber composite using flame hydrolysis deposition demonstrating an integrated FBG anemometer. *Optics Express*, 22(26):32150–32157, Dec 2014.

[190] Christopher Holmes, Alexander Jantzen, Stephen G Lynch, Paul C Gow, Teresa I Ferreiro, and Peter G R Smith. Extreme environment refractometers designed

in integrated optical fibre. In *Conference on Lasers and Electro-Optics, CLEO: Science and Innovations 2017*, Proceedings Conference on Lasers and Electro-Optics. OSA Publishing, 6 2017.

[191] Sam Watts. *Flame Hydrolysis Deposition of Photosensitive Silicate Layers Suitable for the Definition of Wave guiding Structures through Direct Ultraviolet Writing.* PhD thesis, Optoelectronics Research Centre, University of Southampton, 2002.

[192] Benjamin J Metcalf, Nicholas Thomas-Peter, Justin B Spring, Dmytro Kundys, Matthew A Broome, Peter Humphreys, Xian-Min Jin, Marco Barbieri, W Steven Kolthammer, James C Gates, et al. Multi-photon quantum interference in a multiport integrated photonic device. *arXiv preprint arXiv:1208.4575*, 2012.

[193] M. R. Ramadas, A. K. Ghatak, K. Thyagarajan, E. Garmire, and M. R. Shenoy. Analysis of absorbing and leaky planar waveguides: a novel method. *Optics Letters*, 14(7):376–378, Apr 1989.

[194] Babita Hooda and Vipul Rastogi. Low cost highly sensitive miniaturized refractive index sensor based on planar waveguide. *Optik - International Journal for Light and Electron Optics*, 143(Supplement C):158 – 166, 2017.

[195] Qian Wang and Gerald Farrell. All-fiber multimode-interference-based refractometer sensor: proposal and design. *Optics letters*, 31(3):317–319, 2006.

[196] G. J. Veldhuis, L. E. W. van der Veen, and P. V. Lambeck. Integrated optical refractometer based on waveguide bend loss. *Journal of Lightwave Technology*, 17(5):857–864, May 1999.

[197] Wei Liang, Yanyi Huang, Yong Xu, Reginald K Lee, and Amnon Yariv. Highly sensitive fiber Bragg grating refractive index sensors. *Applied Physics Letters*, 86(15):151122, 2005.

[198] C. Gouveia, P. A. S. Jorge, J. M. Baptista, and O. Frazao. Fabry-perot cavity based on a high-birefringent fiber Bragg grating for refractive index and temperature measurement. *IEEE Sensors Journal*, 12(1):17–21, Jan 2012.

[199] K. R. Daly, C. Holmes, J. C. Gates, P. G. R. Smith, and G. D'Alessandro. Complete mode structure analysis of tilted Bragg grating refractometers in planar waveguides toward absolute index measurement. *IEEE Photonics Journal*, 3(5):861–8871, Oct 2011.

[200] Jacques Albert, Li-Yang Shao, and Christophe Caucheteur. Tilted fiber Bragg grating sensors. *Laser & Photonics Reviews*, 7(1):83–108, 2013.

[201] Helen L. Rogers, Sumiaty Ambran, Christopher Holmes, Peter G. R. Smith, and James C. Gates. In situ loss measurement of direct UV-written waveguides using integrated Bragg gratings. *Optics Letters*, 35(17):2849–2851, Sep 2010.

[202] John R Hayes, Seyed Reza Sandoghchi, Thomas D Bradley, Zhixin Liu, Radan Slavík, Marcelo Alonso Gouveia, Natalie V Wheeler, Gregory Jasion, Yong Chen, Eric Numkam Fokoua, et al. Antiresonant hollow core fiber with an octave spanning bandwidth for short haul data communications. *Journal of Lightwave Technology*, 35(3):437–442, 2017.

[203] M Asobe, O Tadanaga, T Yanagawa, T Umeki, Y Nishida, and H Suzuki. High-power mid-infrared wavelength generation using difference frequency generation in damage-resistant Zn:$LiNbO_3$ waveguide. *Electronics Letters*, 44(4):288–290, 2008.

[204] Christopher Holmes, Alexander Jantzen, Alan C. Gray, Paul C. Gow, Lewis G. Carpenter, Rex H. S. Bannerman, James C. Gates, and Peter G. R. Smith. Evanescent field refractometry in planar optical fiber. *Optics Letters*, 43(4):791–794, Feb 2018.

[205] Paul C Gow, Christopher Holmes, Qazi Salman Ahmed, James Gates, and Peter GR Smith. Microwave consolidation of photosensitive planar glass layers. *Integrated Photonics Research, Silicon and Nanophotonics*, pages IW2A–3, 2020.

[206] Justin B Spring, Benjamin J Metcalf, Peter C Humphreys, W Steven Kolthammer, Xian-Min Jin, Marco Barbieri, Animesh Datta, Nicholas Thomas-Peter, Nathan K Langford, Dmytro Kundys, James C. Gates, Brian J. Smith, Peter G. R. Smith, and Ian A. Walmsley. Boson sampling on a photonic chip. *Science*, 339(6121):798–801, 2013.

[207] Paolo L Mennea, William R Clements, Devin H Smith, James C Gates, Benjamin J Metcalf, Rex HS Bannerman, Roel Burgwal, Jelmer J Renema, W Steven Kolthammer, Ian A Walmsley, and Peter G.R. Smith. Modular linear optical circuits. *Optica*, 5(9):1087–1090, 2018.

[208] Senta L Scholl, Rex HS Bannerman, Alexander Jantzen, Sam A Berry, Alan C Gray, James C Gates, Lewis J Boyd, Peter GR Smith, and Christopher Holmes. Integrated optical fibre–investigating the vibrational response using optical frequency domain reflectometry. In *The European Conference on Lasers and Electro-Optics*, page ce_7_4. Optical Society of America, 2019.

[209] Lewis Glynn Carpenter, Sam Berry, Rex Bannerman, Alan Ciaran Gray, James Field, Christopher Holmes, James Gates, Peter Smith, and Corin Gawith. Developing PPLN waveguides for quantum rubidium atom traps in space. In *Nonlinear Photonics*, July 2018.